

SAFEGUARDS APPROACH FOR SPENT NUCLEAR FUEL IN DRY CASK  
STORAGE USING REMOTE MONITORING SYSTEMS

A Dissertation

by

ATHENA ASHWENE SAGADEVAN

Submitted to the Office of Graduate and Professional Studies of  
Texas A&M University  
in partial fulfillment of the requirements for the degree of

DOCTOR OF PHILOSOPHY

Chair of Committee,	Sunil S. Chirayath
Committee Members,	Craig M. Marianno
	John R. Ford
	Andrew L. Ross
Head of Department,	Michael Nastasi

August 2020

Major Subject: Nuclear Engineering

Copyright 2020 Athena Sagadevan

## ABSTRACT

Spent fuel pools at nuclear power reactors are reaching their capacity. Since there is no long-term spent nuclear fuel (SNF) storage solution currently, dry cask storage is practiced in the interim. A single dry cask that stores 32 pressurized water reactor SNF assemblies contains about 20 significant quantities (SQ) of special nuclear material (SQ = 8 kg of plutonium). Once the cask is sealed, it is difficult to verify its contents, hence posing a nuclear safeguards concern because of the potential for misuse of plutonium inside the dry cask. In this work, two new remote monitoring systems (RMSs) to detect the diversion of SNF assemblies from dry casks are studied and results are presented. RMS can perform continuous monitoring so that the International Atomic Energy Agency can maintain continuity of knowledge (CoK) and verify the contents of dry casks without opening them.

Simulations of the RMS response to SNF assembly diversions are characterized for various loading patterns with different fuel burnup and cooling times. Multiple SNF assembly diversion scenarios are studied where a diversion includes the removal and substitution of SNF assemblies with dummy fresh fuel assemblies. The Monte Carlo N-Particle (MCNP) transport code is used to model and simulate the RMS design and the dry cask containing SNF assemblies.

The RMS neutron signal estimated from the simulations are analyzed to determine whether CoK of the SNF assemblies in the dry casks can be maintained. The RMS response is calculated for each assembly diversion scenario by setting a false alarm

probability ( $\alpha$ ) and calculating the corresponding non-detection probability ( $\beta$ ). For both RMSs, the  $\beta$  probabilities are proved to be less than 20% including a single SNF assembly diversion with a measurement time of less than four minutes. Proof-of-concept experiments are conducted using  $^{252}\text{Cf}$  neutron sources and the  $\beta$  probabilities are calculated for neutron source diversions. Analysis of experimental results concluded that neutron source diversions mimicking the diversion of SNF assemblies are detectable in a short measurement time. Hence, RMS designs developed are accurate and viable as an alternative to in-person inspections to detect SNF assembly diversions.

## DEDICATION

To my mother, Grace.

For all the sleepless nights, multiple daily phone calls and countless 30+ hour flights, thank you Amma. None of this would be possible without your constant encouragement, love, laughter, and support.

And to my grandmother, who loved me more than life and knew before I did, that one day, I will be called, Doctor. May your soul rest peacefully in heaven.

## ACKNOWLEDGEMENTS

All glory and honor to God.

There are many people I owe a debt of gratitude and thanks to for my entire academic journey. Firstly, I would like to thank my advisor, Dr. Sunil S. Chirayath for his wisdom, guidance, and ever-willingness to educate me. He has provided me with many opportunities and this work would not have been possible without his expertise. Dr. Chirayath has challenged and pushed me to become a better researcher while providing endless support and feedback. Working with him has been a true blessing.

I would also like to thank the rest of my committee members for their time, effort and support throughout my journey at Texas A&M. In particular, Dr. Craig Marianno for the conversations we have had about neutron detection experiments (despite his own beliefs, that neutrons do not exist), for letting me conduct experiments in his lab and providing me with resources.

It is also important that I mention my gratitude to Professor Sara Pozzi and Dr. Marc Ruch for paving my way into the field of nuclear safeguards while I was an undergraduate student at the University of Michigan. My hunger for success developed early on as I was inspired by both of them.

Dr. Ram Venkataraman and Logan Scott at Oak Ridge National Laboratory, for the tremendous support with planning the logistics of my experiments. Although it did not happen due to the pandemic, I am grateful for all the time and effort. Dr. Shaheen Dewji, for assisting immensely in my professional development and leading me to many

opportunities. Mario Mendoza for his contributions to my dissertation and Kelly Ragusa for all the help.

Words cannot depict the love I have for my family. I am forever in debt to them for being there for me every step of the way, to pick me up when I fall and celebrate even the smallest of successes. Amma, it would be a crime against nature if I started listing all the reasons I am thankful for you – know that you are my greatest strength. Addelynn, you truly are a joy to the world. More than a sister, you are my best friend, confidant, and critique – thank you for believing in me. Appa, you have supported me tremendously through the years – thank you. Allan, Aunty Prema and Uncle Michael, thank you for your constant prayers, love and pride in every success I have achieved.

My friends, because of you, this journey has been wonderful. These friendships will last well past graduation and I look forward to the future. Nuraslinda Anuar and Shu Ying Wee for being my home away from home and the ‘first responders’ to any scene in my life. Rob Zedric for patiently teaching me how to fold origami cranes, the many office dance parties, and pick-me-ups. Tarek Ghaddar for some of my best memories of College Station. Jordan Douglas and Lauren Overbay for sharing your home with me and constant support in my most uncertain times. Adam Howell for the many laughs and help with my job hunt. Matthew Boyd, Mohammad Hawila, Paul Mendoza and everyone in NSSPI who have answered many questions, worked through solutions and spent countless nights at the office – thank you.

Finally, I extend my gratitude to all who directly or indirectly have lent a helping hand in this venture.

## CONTRIBUTORS AND FUNDING SOURCES

### **Contributors**

This work was supervised by a dissertation committee consisting of Prof. Sunil Chirayath [Chair], Prof. Craig Marianno and Prof. John R. Ford of the Department of Nuclear Engineering and Prof. Andrew Ross of the Bush School of Government and Public Service.

All work conducted for the dissertation was completed by the student independently based on the project conceptualization and advice provided by Prof. Sunil S. Chirayath [dissertation advisor].

### **Funding Sources**

Three semesters of the 4-year graduate study were supported through Nuclear Engineering Department's Graduate Teaching Assistantship, two semesters by Texas A&M Nuclear Solutions Institute's Graduate Merit Fellowship and five semesters by Prof. Sunil S. Chirayath from his discretionary research fund.

## TABLE OF CONTENTS

	Page
ABSTRACT .....	ii
DEDICATION .....	iv
ACKNOWLEDGEMENTS .....	v
CONTRIBUTORS AND FUNDING SOURCES.....	vii
TABLE OF CONTENTS .....	viii
LIST OF FIGURES.....	xi
LIST OF TABLES .....	xv
1. INTRODUCTION.....	1
1.1. Motivations.....	1
1.2. Objectives.....	3
1.3. Dissertation Outline.....	4
2. PRESENT EFFORT OF SPENT FUEL VERIFICATION METHODS BACKGROUND AND LITERATURE REVIEW .....	6
2.1. Theory and Background Information.....	6
2.2. IAEA Requirements for Verification .....	7
2.3. Previous Work.....	11
2.3.1. Fingerprint Method.....	11
2.3.2. Compton Dry Cask Imaging System.....	12
2.3.3. Cosmic Ray Muon Radiography .....	13
2.3.4. Bonner Sphere Spectrometry.....	14
2.3.5. Dual Slab Verification Detector .....	14
2.3.6. Neutron Fingerprinting of Dry Casks – Computational Approach .....	15
3. SIMULATION METHODOLOGY FOR DRY CASK REMOTE MONITORING SYSTEM DEVELOPMENT.....	17
3.1. MCNP Simulation Method.....	17
3.1.1. MCNP Modelling of a PWR SNF Assembly .....	21
3.1.2. Neutron Source Term .....	23
3.2. ORIGEN2 Fuel Burnup Simulations .....	25

4. CONCEPTUALIZATION OF SNF ASSEMBLY DIVERSION SCENARIOS AND THE USE OF MCNP .....	27
4.1. SNF Assembly Diversion Scenarios .....	27
4.2. Overview of MCNP Simulations for SNF Diversion Scenarios .....	30
4.3. Overview of MCNP Simulations for both RMS Design Analyses .....	30
4.3.1. Variance Reduction Techniques.....	33
4.3.2. Effect of Variance Reduction Techniques on the External RMS Results.....	36
4.4. Statistical Analysis of MCNP Results of Diversion Scenarios .....	40
5. DEVELOPMENT OF THE REMOTE MONITORING SYSTEM CONFIGURATIONS .....	45
5.1. Procedure.....	45
5.2. Monitoring Limitations of SNF Dry Casks.....	46
5.3. Proposed RMS Approaches .....	47
5.4. Neutron Flux Inside a Dry Cask.....	48
5.5. Neutron Flux Outside Dry Cask.....	54
5.6. Internal RMS .....	57
5.6.1. Function of Each Component in the Internal RMS.....	59
5.7. External RMS.....	75
5.7.1. Polyethylene Optimization .....	78
5.7.2. Number of Detectors/Array Size.....	81
6. ANALYSIS OF DIVERSION SCENARIOS USING BOTH RMS DESIGNS.....	88
6.1. Internal RMS Homogenous Assembly Contributions.....	90
6.2. Internal RMS and Diversion Scenarios.....	91
6.3. External RMS Homogenous Assembly Contributions.....	94
6.4. External RMS and Diversion Scenarios.....	94
6.4.1. Minimum Measurement Time.....	98
7. CHARACTERIZATION OF RMS DESIGNS FOR HETEROGENEOUS SNF LOADING PATTERNS .....	105
7.1. Internal RMS Results for Various Heterogeneous Loading Patterns.....	108
7.2. External RMS Results for Various Heterogenous Loading Patterns .....	111
7.3. Conclusions .....	113
8. CHARACTERIZATION OF RMS FOR MULTIPLE CASK SCENARIO.....	114
9. EXPERIMENTS TO VERIFY INTERNAL RMS CAPABILITIES .....	118
9.1. MCNP Simulations using <sup>252</sup> Cf as a Surrogate for SNF .....	119
9.1.1. Isotropic Point Source to Surface Source Approximation .....	121

9.1.2. Approximating Concrete Body Shielding of Dry Cask.....	126
9.1.3. Approximating Lid of Dry Cask .....	126
9.2. Experiments at Texas A&M using <sup>252</sup> Cf as a Surrogate for SNF .....	133
9.3. Results of Experiments .....	139
9.4. MCNP Simulations of Final Experimental Setup .....	143
10. EXTERNAL RMS MATERIAL STUDY .....	153
10.1. Effect of LiF Material in the External RMS for Homogenous Assemblies .....	155
10.2. Effect of LiF Material in External RMS on Heterogenous Loading Patterns...	157
11. CONCLUSIONS .....	160
11.1. Future work .....	161
REFEFENCES .....	163
APPENDIX A .....	172
APPENDIX B .....	185
APPENDIX C .....	187
APPENDIX D .....	188
APPENDIX E.....	189
APPENDIX F .....	191
APPENDIX G .....	193

## LIST OF FIGURES

	Page
Figure 3-1 VISED rendering of a dry cask (a) axial view (b) radial view .....	20
Figure 3-2 17x17 PWR assembly inside the dry cask MPC basket from a (a) cross section view and (b) axial view .....	23
Figure 4-1 Diversion scenario (DS) configurations where the yellow cell indicates the position of the substituted assembly where the diversion has occurred.....	29
Figure 4-2 Diversion scenarios 1, 2, 3, 4, and 5 in a dry cask that can be used for symmetrical purposes .....	29
Figure 4-3 Pictorial representation of importance sampling variance reduction method in the MCNP dry cask model cells.....	34
Figure 4-4 FOM of external RMS box configurations.....	39
Figure 4-5 Graphical display of false alarm probability, $\alpha$ and non- detection probabiliy, $\beta$ for 5% alarm threshold.....	43
Figure 5-1 Internal RMS location denoted by yellow box and mesh tally positions by red lines. Blue box denotes MPC lid .....	49
Figure 5-2 Thermal flux mesh tallies at the (a) top and (b) bottom positions .....	51
Figure 5-3 Location for external RMS shown in blue on (a) the lid of the dry cask and (b) around the body .....	54
Figure 5-4 Thermal neutron flux on the dry cask lid .....	56
Figure 5-5 Internal RMS with fission chambers (denoted by uranium lining and air), polyethylene and cadmium shown in (a) front view and (b) top view .....	58
Figure 5-6 Position of internal RMS within dry cask .....	58
Figure 5-7 Internal RMS with one fission chamber in the center .....	64
Figure 5-8 $\beta$ probabilities (%) for each fission chamber where $D_C$ is the center detector in blue, $D_L$ and $D_R$ are the left and right detectors in red. $\beta_C$ , $\beta_L$ and $\beta_R$ are the corresponding $\beta$	

probabilities. The yellow square designates position of diverted assembly. All results are for 3 s measurement time and 5% $\alpha$ .....	65
Figure 5-9 Internal RMS configuration from Khudoleeva et al.....	70
Figure 5-10 Mesh tally indicating the thermal neutron flux above cadmium and in the corner.....	71
Figure 5-11 Flux ratio versus cadmium size .....	72
Figure 5-12 External RMS with MSND detectors shown in (a) front view and (b) top view.....	77
Figure 5-13 Thermal neutron flux as a function of polyethylene thicknesses above the detector cells and the lines represent the variation of polyethylene thicknesses below the detector cells.....	80
Figure 5-14 MSND array configurations on the lid of the dry cask where the blue cells represent the position of the detector in different configurations on the lid (circle) .....	81
Figure 6-1 Assembly numbers in a dry cask containing 32 SNF assemblies.....	89
Figure 6-2 Thermal neutron flux contributions (%) from each assembly to the (a) left and (b) right detectors within the internal RMS .....	90
Figure 6-3 $\beta$ probabilities (%) for each detector and all diversion scenarios at 5% $\alpha$ threshold using a 2-second measurement time and 1% $\alpha$ threshold using a 4-second measurement time.....	93
Figure 6-4 Thermal neutron flux contributions (%) from each assembly to the external RMS.....	94
Figure 6-5 $\beta$ probabilities (%) for all diversion scenarios at 5% $\alpha$ threshold using 5- second measurement time and 1% $\alpha$ threshold using a 9- second measurement time.....	97
Figure 6-6 $\beta$ probabilities (%) versus measurement time in the left, $D_L$ and right, $D_R$ detectors for DS1 and DS4 after 45 years of initial loading in the dry cask. ....	99
Figure 6-7 $\beta$ probabilities (%) versus measurement time in the external RMS for DS1 and DS4 after 45 years of initial loading in dry cask.....	101

Figure 6-8 $\beta$ probabilities for both detectors for DS1 and DS4 with the internal RMS as a function of time since initial cask loading.....	102
Figure 6-9 $\beta$ probabilities (%) for DS1 and DS4 with external RMS as a function of time since initial cask loading.....	103
Figure 7-1 Three different loading patterns where the numbers in each box are the assembly number, and average neutron emission rate ( $n.s^{-1}$ ) .....	107
Figure 7-2 Three loading patterns where the top to bottom numbers are the assembly number, assembly contributions (%) to the left and right detectors respectively and the $\beta$ probability (%) for the particular assembly diversion.....	109
Figure 7-3 Three loading patterns where the top to bottom numbers are the assembly number, assembly contributions (%) to the detectors in the external RMS and the $\beta$ probability (%) for the particular assembly diversion .....	112
Figure 8-1 Nine fully loaded dry casks .....	114
Figure 9-1 Dots represent 32 $^{252}\text{Cf}$ point neutron sources in a dry cask. ....	119
Figure 9-2 Eight assemblies represent $\frac{1}{4}$ of a dry cask.....	120
Figure 9-3 The blue blocks represent SNF assemblies. The RMS (red block) is placed on top of the assemblies which appears as a surface source (yellow squares) to the detectors .....	121
Figure 9-4 Setup of $^{252}\text{Cf}$ source and surrounding material for all simulations .....	123
Figure 9-5 Results of reflector study using a single $^{252}\text{Cf}$ source surrounded by different reflector materials.....	125
Figure 9-6 VISED rendering of top part of dry cask containing SNF .....	127
Figure 9-7 VISED rendering of eight $^{252}\text{Cf}$ point sources representing $\frac{1}{4}$ the contents of a dry cask. The pink box surrounding each point source is the reflector material. A single black box in the bottom left corner indicates the position for the mesh tally. Blue boxes are concrete.....	128

Figure 9-8 VISED rendering of the thickness of concrete being varied. The blue boxes are concrete. ....	128
Figure 9-9 Combined thermal neutron counts for 1-second measurement time as a function of concrete thickness.....	130
Figure 9-10 Combined thermal neutron counts for 1-second measurement time as a function of concrete width for varied thicknesses.....	132
Figure 9-11 (a) 32 assemblies divided into 8 sections such that each section is made up of (b) 3 full assemblies and 2 half assemblies represent one section which is 1/8 of a dry cask.....	134
Figure 9-12 Approximation of internal RMS with two fission chambers enveloped in polyethylene and cadmium with a concrete lid .....	134
Figure 9-13 Setup of experiments using polyethylene reflectors from the (a) side view and (b) top view where numbers present indicate the position of the <sup>252</sup> Cf source .....	135
Figure 9-14 Setup of experiments using graphite reflectors .....	136
Figure 9-15 Basic electronic configuration for experiments.....	137
Figure 9-16 VISED 3D rendering of experimental setup for the graphite reflected system.....	144
Figure 9-17 Neutron counts with 2σ uncertainties obtained in the left and right detectors using polyethylene reflectors for a measurement time of 90 seconds.....	146
Figure 9-18 Neutron counts with 2σ uncertainties obtained in the left and right detectors using graphite reflectors for a measurement time of 220 seconds.....	147
Figure 10-1 Neutron flux observed by external cask detector for void and LiF detector materials.....	154
Figure 10-2 β probabilities (%) for the external RMS using LiF and void detector materials .....	156
Figure 10-3 Three loading patterns where the top to bottom numbers are the assembly number, assembly contributions (%) to the detectors in the external RMS and the β probability (%) for the particular assembly diversion.....	158

## LIST OF TABLES

	Page
Table 2-1 IAEA significant quantities for nuclear material .....	8
Table 2-2 Number of PWR spent fuel assemblies that must be diverted to obtain 1 SQ of Pu (8-kg) and <sup>235</sup> U (75-kg) .....	10
Table 3-1 Dimensions of the dry cask modeled in MCNP.....	19
Table 3-2 Dimensions of a Westinghouse 17 x 17 fuel assembly.....	22
Table 3-3 Energy dependent neutron emission rate for a single three-year cooled PWR SNF assembly with a burnup of 45 GWD/MTU.....	24
Table 3-4 Neutron source emissions per assembly for various burnup steps using 3-year and five-year cooling periods .....	25
Table 4-1 Neutron energy group structure used for calculation of external and internal RMS response .....	32
Table 5-1 Energy dependent flux tallied below and above the stainless steel MPC lid and corresponding transmission factor .....	52
Table 5-2 Energy dependent neutron flux on the lid of a dry cask .....	55
Table 5-3 Thermal neutron flux in D <sub>C</sub> , D <sub>L</sub> , and D <sub>R</sub> which are the center, left and right fission chamber detectors for all diversion scenarios (DS) and the percentage difference in thermal flux between D <sub>C</sub> /D <sub>L</sub> , D <sub>C</sub> /D <sub>R</sub> and D <sub>L</sub> /D <sub>R</sub> .....	67
Table 5-4 β probabilities (%) for all diversion scenarios for different cadmium sizes using a 2-second measurement time and 5% α .....	74
Table 5-5 Configurations, dimensions and number of detectors used for each MCNP simulation performed where R is radius, L is length, W is width, x is the horizontal plane and y is the vertical plane .....	82
Table 5-6 β probabilities (%) for all configurations and all SNF diversion scenarios (DS) studied using a 5% false alarm probability (α) and 5-second counting time. Red numbers represent β probabilities over 20% .....	85

Table 6-1 Total source strength of SNF for all diversion scenarios.....	89
Table 8-1 $\beta$ probabilities recorded for each DS for $\alpha$ of 5% (t=82 s) and 1% (t=133s) for the multiple dry casks case with external RMS .....	116
Table 9-1 Characteristics of potential moderator/reflector materials.....	124
Table 9-2 Percentage increase in counts as a function of concrete thicknesses and varied widths and corresponding mass of concrete slab .....	131
Table 9-3 $^{252}\text{Cf}$ sources and neutron emission rates.....	133
Table 9-4 Approximations made between experiment performed and MCNP simulations of internal RMS in dry cask storage. ....	138
Table 9-5 Neutron counts recorded by $D_1$ and $D_2$ for 90 seconds measurement time and corresponding $\beta$ probabilities $\beta_R$ and $\beta_L$ using polyethylene reflected sources .....	140
Table 9-6 Neutron counts recorded by $D_R$ and $D_L$ for 220 seconds measurement time and corresponding $\beta$ probabilities $\beta_R$ and $\beta_L$ using graphite reflected sources.....	141
Table 9-7 $\beta$ probabilities (%) in the left and right detectors, comparing measurement neutron counts to MCNP simulation counts. These show values for the polyethylene reflected sources using a measurement time of 90 s and 5% $\alpha$ .....	149
Table 9-8 $\beta$ probabilities (%) in the left and right detectors, comparing measurement neutron counts to MCNP simulation counts. These show values for the graphite reflected sources using a measurement time of 220 s and 5% $\alpha$ .....	150

## 1. INTRODUCTION

The goal of this research is to develop a neutron detection system for remote and continuous monitoring of spent nuclear fuel (SNF) stored in dry casks to support the Continuity of Knowledge (CoK) element of nuclear safeguards. Current safeguards techniques employed rely on containment and surveillance (C&S) measures, however, with the increasing number of dry cask storage facilities, there is an increased likelihood of a C&S failure and loss of CoK. Hence, the proposed detection systems offer a method to independently verify the contents of the dry cask.

### 1.1. Motivations

Countries around the world take different approaches to handling SNF, including reprocessing or storage either in an underground repository or in multiple interim dry casks. Presently, only Sweden and Finland are expected to see underground repositories for radioactive waste completed in the 2020s, while plans for permanent storage facilities nearly everywhere else are stalled [1]. Meanwhile, as other nations, especially in Asia, ramp up their nuclear capacity, the need for storing spent fuel continues to increase; hence, building spent fuel pools and dry cask storage facilities are the only viable tested and practical options for the near future [1].

As a pioneer in the nuclear power industry, the United States has operated commercial nuclear power reactors since the 1960s with the goal of generating electricity [2]. Almost five decades later, there is yet to be a long-term solution for

disposing of the nation's SNF. According to the Nuclear Energy Institute, as of September 2016, there are 78,590 metric tons of commercial spent fuel accumulated in the United States, and approximately one fifth of this SNF is stored in dry casks [3]. The total increases by 2000 to 2400 tons annually [4]. Dry cask storage allows for the interim storage of SNF assemblies that have been cooled in a pool for at least one year. These casks are designed and constructed with steel and thick concrete in order to confine the SNF assemblies and keep the radiation dose rate levels in accordance with the required regulations. In addition to storage, certain cask designs are used for transportation, therefore serving a dual purpose. Also, the modular nature of these casks allow for future storage in repositories [5]. However, a disadvantage of using dry casks from a nuclear safeguards perspective is that there is no effective way of verifying a cask's contents after it has been sealed. Current safeguards measures rely on C&S techniques, primarily by using seals and optical surveillance systems [6]. Nevertheless, if a seal is broken, there is no method to verify the contents of a cask without opening it. Opening the cask would expose operating personnel to high levels of radiation in addition to being expensive and undesirable. In order to overcome these issues, a remote monitoring system (RMS) is proposed. RMSs combine non-destructive assay (NDA) and C&S to collect and transmit data continuously to the authorities. RMSs fall under Information Driven Safeguards (IDS), which is a vital portion of the International Atomic Energy Agency's (IAEA) analytical capability to ensure the non-diversion of declared nuclear material and the absence of undeclared nuclear material and activities in a State [7]. IDS employ physical verification with cutting edge technology in order to verify that States

fully comply with their nonproliferation commitment. Hence, with continual monitoring of events, the IAEA fulfils its requirement of maintaining CoK and thus verifying the contents of the dry casks without ever having to open them. Other advantages of employing RMSs for dry cask storage include reducing the number of visits an inspector has to perform to ensure a facility is safeguarded; therefore, it is more efficient and cost-effective.

## **1.2. Objectives**

The main objective of this dissertation is to investigate the neutron radiation signature emitted by SNF stored inside a dry cask and to utilize this signature to detect possible diversions of SNF assemblies. Even with significant shielding, there are still neutrons that escape the dry cask, which allows for the possibility of taking neutron measurements outside of a dry cask to verify its contents inside [8]. The work in this dissertation is focused on the development and analysis of two neutron-based RMS designs using both computational and experimental methods. The first design is an internal RMS that is deployed inside the dry cask before it is sealed, supporting the concept of safeguards-by-design. The second design is an external RMS that can be placed outside a dry cask after it has been sealed. Both methods allow for maintenance of CoK on the contents of the dry cask and should be sensitive to potential diversions of SNF assemblies. An additional objective of this research was to conduct proof-of-concept experiments to verify the effectiveness of the RMS design.

### **1.3. Dissertation Outline**

Chapter 2 outlines the background information required to better understand the challenges of safeguarding SNF in dry cask storage. The properties of SNF and IAEA safeguards verification requirements are presented. Following that, the present methods of safeguarding SNF in dry casks are reviewed.

In Chapter 3, the radiation transport method used to simulate the dry cask and the SNF are discussed. Following that, the details used to model the dry cask with SNF assemblies and the details of the neutron source term are described.

Chapter 4 describes the concept of SNF assembly diversions from the dry cask and the methodology used for quantification of the neutron signal using the RMS.

The limitations of a dry cask from a radiation detection perspective, the design requirements of the internal and external RMS designs, and the final RMS design details are discussed in Chapter 5. The details of the proposed RMS design studies, viable locations for its placement, choice of detectors, number of detectors and the working principle of the detectors are also described in this chapter.

Chapter 6 presents the results of SNF assembly diversion scenarios analyzed using the final RMS designs proposed in Chapter 5. Also, the minimum detectable neutron signal and minimum measurement time for the RMSs are shown as a function of time since initial loading of SNF in the dry cask.

Chapter 7 employs the RMSs in dry casks with various SNF loading patterns and gives the details of the results of SNF assembly diversion scenarios.

Chapter 8 shows a multi-cask scenario where the signal of the external RMS on the central cask is studied while it is surrounded by eight other SNF filled dry casks. This is done to investigate the effect of surrounding neutron radiation from other casks on the neutron signal on the individual cask being monitored.

Chapter 9 shows the experiments done at Texas A&M University using  $^{252}\text{Cf}$  sources and fission chamber detectors to mimic the output of the internal RMS in the event of a diversion. This small-scale experiment serves as a proof-of-concept for the internal RMS.

Chapter 10 is a preliminary study of the external RMS using  $^6\text{LiF}$  material in the detector volume to better understand radiation interactions within. This is done for homogenous and heterogenous loading patterns. The results are compared with the previous cases that are void of material (in place of  $^6\text{LiF}$ ) and conclusions are drawn regarding the capabilities of the external RMS.

Finally, chapter 11 concludes this dissertation and proposes future work.

## 2. PRESENT EFFORT OF SPENT FUEL VERIFICATION METHODS

### BACKGROUND AND LITERATURE REVIEW

#### **2.1. Theory and Background Information**

A typical pressurized water reactor (PWR) contains 150-200 fuel assemblies in its core depending on the design [9]. Most commercial PWRs are refueled on an 18 to 24 month cycle, where approximately one third of the core is replaced [10]. The SNF assemblies that are removed from the reactor core are transferred to a spent fuel pool located at the reactor site. At this point, the back end of the nuclear fuel cycle begins.

The back end of the nuclear fuel cycle is comprised of the spent fuel in the pool, the interim dry cask storage and finally the reprocessing/recycling or long term waste disposal depending on whether the country in question employs a closed or open fuel cycle [11]. The highly radioactive SNF assemblies will remain in the spent fuel pool for a few years to allow a majority of the short-lived fission products to decay away. Following that, when water is no longer required to remove the decay heat, the SNF assemblies are transferred into dry cask storage.

As of 2019, the United States has over 90,000 tons of nuclear waste that requires disposal. The U.S. commercial power industry generated 80,000 tons of that waste [12]. In the absence of a permanent geological repository in the U.S., commercial nuclear power plants have been storing their SNF on site in pools and using dry cask storage methods under the Atomic Energy Acts. The U.S. Nuclear Waste Technical Review Board predicts that the quantity of SNF stored as of 2012 at commercial nuclear power

plants will approximately double by 2048 [13]. Other countries practice different methods. For instance, China, France, India, Pakistan, Russia and the U.K. reprocess their SNF [14]. In addition, Belgium, Finland, France, Japan, Korea, Sweden and Switzerland are pursuing deep geological repositories for the long-term disposal of SNF [15].

There are two main types of light water reactors (LWRs) - pressurized water reactors (PWRs) and boiling water reactors (BWRs). These reactors are referred to as LWRs because light water is used for both as the coolant to remove nuclear fission heat and to moderate the neutron energy in the core. Low enriched Uranium (LEU) is the main type of fuel used in LWRs. The most common of these is the PWR, representing 300 of the world's 448 reactors now operating [16].

In PWRs, the fuel is made from uranium dioxide ( $\text{UO}_2$ ) which is shaped into pellets with a diameter of 1 cm and a length of 2 cm. These pellets are stacked in Zircaloy metal cladding, which is sealed to form a fuel pin. Fuel pins that are stacked together in specific configurations are referred to as assemblies [17]. For the work performed in this dissertation, the 17 x 17 PWR fuel assembly is used, which contains 32 spent fuel assemblies and comprises the total contents of a dry cask.

## **2.2. IAEA Requirements for Verification**

Under Article 28 of INFCIRC153, the technical objective of international safeguards is “the timely detection of diversion of significant quantities of nuclear material from peaceful nuclear activities to the manufacture of nuclear weapons or of

other nuclear explosive devices or for purposes unknown, and deterrence of such diversion by the risk of early detection”[18]. One significant quantity (SQ) is the approximate amount of nuclear material for which the possibility of manufacturing a nuclear explosive device cannot be excluded [19]. Table 2-1 shows the SQ values of various nuclear materials.

**Table 2-1 IAEA significant quantities for nuclear material**

<b>Material</b>	<b>SQ</b>
Direct - Use Material	
Pu (containing < 80% <sup>238</sup> Pu)	8 kg of Pu (all isotopes)
<sup>233</sup> U	8 kg <sup>233</sup> U
Highly Enriched Uranium ( <sup>235</sup> U>20%)	25 kg <sup>235</sup> U
Indirect - Use Material	
Low Enriched Uranium ( <sup>235</sup> U < 20%)	75 kg <sup>235</sup> U
Th	20 t Th (all isotopes)

The timely detection of diversion refers to a set of timeliness goals that are based on the time required to convert diverted material into the components of a nuclear explosive device and the type of material in question [20]. For the verification of LWR SNF, the following SQs and timeliness detection goals apply [21]:

- Diversion of 8 kg of Pu (all isotopes) is to be detected within:
  - 1 month for fresh fuel
  - 3 months for spent (irradiated) fuel
- Diversion of 75kg of  $^{235}\text{U}$  contained in low enriched uranium ( $^{235}\text{U} < 20\%$ ), natural or depleted uranium is to be detected in 12 months

SNF is subjected to IAEA safeguards as it is “irradiated direct use material”.

During an inspection of a facility, the IAEA inspectors verify the spent fuel inventory declared by the operator via item accounting and measuring a sample of the assemblies (in spent fuel pools) to ensure the validity of the operator’s accountancy system. The operating records and surveillance system data are also reviewed to obtain a complete picture of the system. However, because they are limited by time and resources, not every single item in a facility is checked and accounted for with all the aforementioned methods, though they will all be identified at least by their serial numbers. Instead, several samples are measured to achieve the desired detection probability,  $P$ , of a diversion of one SQ of material. The number of samples,  $n$ , to be selected for measurement from each stratum is given by Equation 2-1.

$$n = N(1 - \beta^{1/D}) \quad \text{Eq. 2- 1}$$

where  $\beta$  is the non-detection probability,  $N$  is the total number items in the stratum, and  $D$  is  $M/x$  and is the number of defects in the stratum rounded up to the next integer.  $M$  is the goal amount. In this case  $M$  is the SQ value, and  $x$  is the average nuclear material

weight of an item in the stratum. To put these numbers in perspective, the number of SNF assemblies to be diverted to obtain 1 SQ of Pu and <sup>235</sup>U are listed in Table 2-2. Also, employing Equation 2-1, the fraction of dry casks that must be sampled in order to detect diversions with a 20% non-detection probability of  $\beta$  is shown as the n/N fraction. The ORIGEN 2 software was used to generate the following values.

**Table 2-2 Number of PWR spent fuel assemblies that must be diverted to obtain 1 SQ of Pu (8-kg) and <sup>235</sup>U (75-kg)**

<b>Burnup (GWd/MTU)</b>	<b>10</b>	<b>20</b>	<b>30</b>	<b>40</b>	<b>45</b>	<b>50</b>
Pu mass per FA (kg)	1.74	2.93	3.94	4.84	5.23	5.56
# FA to acquire 1 SQ	4.59	2.74	2.03	1.65	1.53	1.44
Fraction of the cask to be sampled (n/N)	30%	44%	55%	62%	65%	67%
<sup>235</sup> U mass per FA (kg)	14.54	10.21	6.76	4.14	3.16	2.37
# FA to acquire 1 SQ	5.16	7.35	11.10	18.13	23.75	31.61
Fraction of the cask to be sampled (n/N)	27%	20%	13%	8%	7%	5%

From Table 2-2, in order to achieve a  $\beta$  probability of 20%, (for 1 SQ of Pu diversion), approximately 30% - 67% of the contents of each cask will need to be sampled depending on the declared burnup. The same for 1 SQ of <sup>235</sup>U is 5-27%. Additionally, to obtain the SQs defined in Table 2-1, ~ 2 fuel assemblies (FAs) will need to be diverted to accrue 1 SQ of Pu, which is 8 kg, and 5 – 30 FAs will need to be diverted to accrue 1 SQ of <sup>235</sup>U, which is 75 kg. Hence, based on the results in Table 2-2, it is evident that

verifying the Pu content in PWR SNF is of importance to safeguard and that verifying  $^{235}\text{U}$  content is less significant due to the large number of FAs that need to be diverted.

### **2.3. Previous Work**

Once a dry cask has been sealed, verification of its contents is very challenging. This loss of CoK is risky and must be overcome. Hence, current spent fuel verification methods must be improved to ensure the timely detection of the diversion of a significant quantity of nuclear material. The following sections will describe some SNF verification methods found from literature.

#### **2.3.1. Fingerprint Method**

In this method, researchers at Lawrence Livermore National Laboratory examined radiation signals (gamma and neutron) from six different types of dry cask storage containing spent nuclear fuel [22]. A gamma ray imager, thermal neutron imager and germanium spectrometer were used to collect data. Each dry cask emitted an independent signature known as a ‘fingerprint,’ which can be used to distinguish one from another. From the studies, it was seen that in order to obtain significant results, measurements of a few hours was required for each cask. However, there were some limitations to this method: (1) The gamma radiation signal observed by the detectors was dominated by radiation that was scattered in the shielding rather than the original information carrying the gamma radiation signal. This caused the image to be unclear and led to the conclusion that a better gamma imager with a larger surface area and higher sensitivity to higher energy unscattered gammas should be developed to produce

images that are sharp and meaningful. (2) The neutron radiation signal also underwent a similar scattering, which created fuzzy images that did not provide any details of the dry cask being imaged. However, LLNL's work regarding the measurable fluence of higher-energy, unscattered radiation exiting the casks provided evidence. Images obtained with instruments sensitive to this high-energy and unscattered radiation may provide the requisite clarity to allow fingerprinting to succeed. Such devices are currently under development.

### **2.3.2. Compton Dry Cask Imaging System**

Another method that has been studied uses gamma ray imaging to distinguish the diversion of spent fuel [23]. It is possible to detect high-energy gamma radiation from  $^{60}\text{Co}$  (formed due to the neutron activation of  $^{59}\text{Co}$  impurity present in the structural components of the fuel assembly) and  $^{137}\text{Cs}$  (long lived fission product present in fuel assembly) penetrating through the dry cask shield.

In this study, a high purity germanium detector (HPGe) is placed on the outside of the dry cask lid above the known position of the SNF. When the detector is placed above a spot that is filled, the unscattered gamma radiation reaches the detector and registers counts in spectral peaks. However, when positioned over an empty slot, a majority of the gammas have been Compton scattered, and the energies are too low to register at the peak. The ratio of peak to Compton continuum counts is observed for every assembly position above the dry cask. The ratio of peak to Compton-continuum counts is high above full slots and, conversely, the ratio is low above empty slots.

This method proved viable for verifying the contents of dry casks using gamma ray spectroscopy; however, it may not work for diversion scenarios employing dummy assembly replacements.

### **2.3.3. Cosmic Ray Muon Radiography**

There have been multiple studies of cosmic ray muon radiography for spent nuclear fuel stored in dry casks [24–29]. The underlying principles of detection are as follows.

Cosmic ray muons are produced by interactions of protons and nuclei from space with atoms in the upper atmosphere. Collisions of these primary cosmic rays with atmospheric gas produce showers of pions, many of which decay to muons [30]. Muons that make it to the earth are usually high in energy and hence have a high penetrating nature. The incoming and outgoing muon trajectories are measured with two identical drift tube tracking detectors, which are placed on the opposite sides of a dry cask. Muons passing through the tubes ionize the gas, and the resulting electrons drift towards the wire where they are multiplied through an avalanche process in the high electric field near the surface of the wire, producing a measurable signal [29].

Using this method, diversions of SNF assemblies can be identified. However, measurement times of the order of weeks to several months is needed. Also, more complicated geometries including replacing diverted assemblies with dummies and partially filled assemblies are not yet tested.

#### **2.3.4. Bonner Sphere Spectrometry**

A method for SNF dry cask monitoring using bonner spheres is also found in literature [31]. These multi-sphere spectrometry detectors employ thermal neutron detectors like  $\text{BF}_3$  or  $^3\text{He}$  detectors within layers of moderating material, specifically polyethylene of varying thicknesses.

An estimate of the neutron spectrum can be obtained by correlating the count rate between layers of moderating material. For instance, the small spheres would allow for the detection of low energy neutrons, while fast energy neutrons pass through undetected. Larger spheres conversely will capture low energy neutrons and detect fast neutrons by moderating them. Since these are thermal neutron detectors, all initial energy information is lost. In addition, these detectors are commonly used as dosimeters rather than spectrometers.

#### **2.3.5. Dual Slab Verification Detector**

The dual slab verification detector (DSVD) was built by Los Alamos National Laboratory in collaboration with the IAEA as part of the dry cask storage safeguards system used to store spent fuel from the BN-350 fast reactor. The assemblies of the BN-350 reactor are hexagonal and contain uranium oxide rods. Each dry cask contains between four to eight assemblies [32].

The working principle of the DSVD is the use of ten  $^3\text{He}$  tubes in two rows encased in polyethylene slabs separated by a sheet of cadmium. The inner row of  $^3\text{He}$  detectors is sensitive to the contents of the dry cask while the outer row is used to obtain

background measurements from the neighboring casks. This arrangement allows for a method for suppressing background neutrons and determining the neutrons emitted by the cask of interest. Preliminary experiments show that the total uncertainty with verifying the neutron fingerprint of a dry storage cask is approximately  $\pm 3\%$  [32].

Past fingerprints are compared with current fingerprints to determine if a diversion has occurred. This method is viable option, however, is costly due to the usage of  $^3\text{He}$  detectors.

### **2.3.6. Neutron Fingerprinting of Dry Casks – Computational Approach**

In this study, researchers from the University of Florida devised a computational study to evaluate the feasibility of neutron spectroscopy for the safeguarding of SNF assemblies in a dry cask storage [33]. Their method involved a computational study by modelling dry casks and their contents using the Next Generation Safeguards Initiative (NGSI) Spent Fuel Library, the one-group fuel burnup code ORIGEN-S, and the Monte Carlo radiation transport code (MCNP).

100  $^4\text{He}$  detectors are placed in a ring outside the cask at a specified height. These detectors work by scattering fast neutrons with helium gas. As fast neutrons move through the gas, they undergo elastic scattering and transfer a fraction of their kinetic energy to the  $^4\text{He}$  nucleus dependent on the scattering angle. The  $^4\text{He}$  recoil nucleus obtains a large kinetic energy and leaves the electrons behind. The recoiled alpha particle interacts with other helium atoms through excitation or ionization. Scintillation light is then emitted during the de-excitation, which can be detected [8].

The count rates from 100 neutron detectors can be used to form a signature of the dry cask. Diversion scenarios of assemblies that are not shielded by other assemblies are easily detectable while central assembly diversions are challenging.

This method also relies on re-evaluating the contents of the dry cask as a function of time, as count rates will decrease with time.

This method is viable; however, detecting diverted assemblies replaced with dummies and partially filled assemblies is not currently feasible. Employing 100  $^3\text{He}$  detectors is also extremely cost intensive.

### 3. SIMULATION METHODOLOGY FOR DRY CASK REMOTE MONITORING SYSTEM DEVELOPMENT

The objective of this research is to analyze the neutron radiation signal emitted from SNF assemblies stored inside a dry cask to detect the potential diversion of SNF assemblies. Development of two neutron-based RMS designs is envisaged to meet the research objective. The first RMS design is for placement inside the dry cask before it is sealed. The second RMS design is for placement on top of the dry cask lid. Both designs should support the maintenance of CoK on the contents of the dry cask and should be sensitive to potential diversion of SNF assemblies.

To develop the RMS designs, modelling of the dry cask with SNF assemblies is essential. This is done using the Monte Carlo N- Particle (MCNP) radiation transport code. The Oak Ridge Isotope GENeration code (ORIGEN2) was used for the SNF source term estimation.

#### **3.1. MCNP Simulation Method**

MCNP is a radiation transport code developed by Los Alamos National Laboratory [34]. It can be used for neutron, photon, electron, or coupled neutron/photon/electron transport. MCNP employs a stochastic process where probability distributions of the radiation transport equation are randomly sampled to determine the path of a particle. By sampling appropriate probability distributions, the particle may undergo appropriate interactions including absorption, scattering, fission,

etc. MCNP is a versatile radiation transport code because it can handle complicated geometries and multiple source definitions along with the provision of scoring (tallies) fluence rates and other needed radiation responses. Verification and validation of the code is continuously done through experimental benchmarks. [35] .

A MCNP model of a dry cask filled with 32 PWR SNF assemblies, along with its neutron source term integrated with the RMS design, is needed to estimate the neutron radiation signal. Since there are many dry cask designs, the MCNP model made for this research was based on a Holtec design, the HI-STORM 100S Version B (218) [36]. Most features were explicitly modeled; however, some approximations were necessary both to limit the simulation time and due to the proprietary nature of information related to this product.

When full, this dry cask can accommodate up to 32 PWR SNF assemblies. The Holtec dry cask design consists of a multipurpose canister (MPC). The MPC is a stainless-steel grid structure that stores the SNF assemblies. Also, each cell in the MPC grid surrounding the fuel assembly position is lined with Boral for additional neutron shielding. Each MPC consists of a fuel basket, base plate, canister shell and a lid. The rectilinear stainless steel grid allows for the assemblies to be placed in specific locations that optimize uniform distribution of metal mass and radiation attenuation [36]. For the case being studied, MPC-32 can hold a maximum of 32 PWR fuel assemblies; however, there are different designs that can accommodate different numbers of assemblies and types of fuel. For instance, MPC-24 can contain up to 24 PWR assemblies, and MPC-68 can contain up to 68 boiling water reactor (BWR) assemblies [33].

**Table 3-1 Dimensions of the dry cask modeled in MCNP**

<b>Parameter for the multipurpose canister (MPC)</b>	<b>Dimension (cm)</b>
Outer steel radius	85.86
Inner steel radius	84.46
Steel lid thickness	24.14
<b>Parameters for the steel-lined concrete overpack</b>	<b>Dimension (cm)</b>
Outer radius	166.52
Inner radius	85.86
<b>Top layers:</b>	<b>Dimension (cm)</b>
Concrete thickness	20
Stainless steel top thickness	2.54
<b>Bottom layers:</b>	<b>Dimension (cm)</b>
Stainless steel thickness	6.35

An over-pack surrounds the MPC. The over-pack is a steel structure that is designed to be filled with concrete on-site [37]. Concrete serves a safety role as a shield from the high level of radiation from the SNF assemblies. The dimensions of the MPC and the over-pack used for the MCNP model of the dry cask are shown in Table 3-1 and graphically depicted in Figure 3-1 using Visual Editor (VISED). Also, an MCNP input file is attached in Appendix A. Some approximations were made to optimize the MCNP simulation time as well as to prevent full disclosure of the proprietary information of the

dry cask design. Simplifications primarily focused on the lid, which is very complex; however, shield thickness was not compromised. Extrusions, filets, chamfers, and minor penetrations were not modeled in order to simplify the MCNP model.

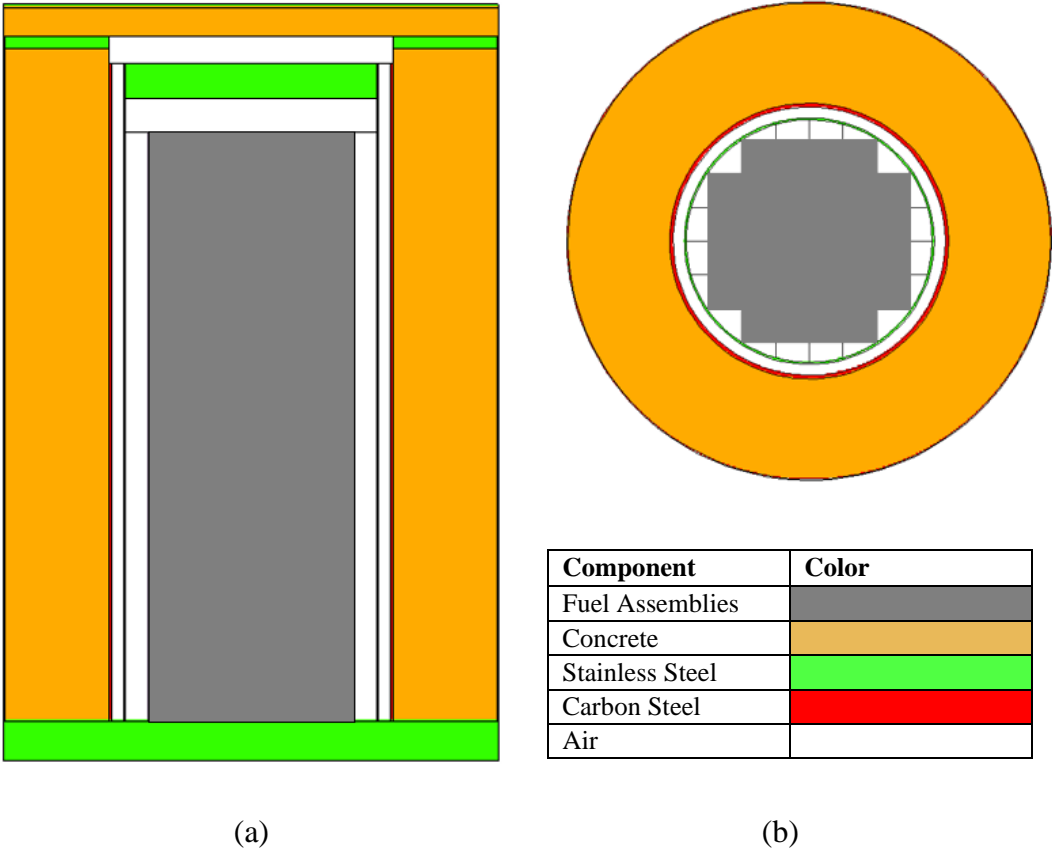


**Figure 3-1 VISED rendering of a dry cask (a) axial view (b) radial view**

### 3.1.1. MCNP Modelling of a PWR SNF Assembly

The next model prepared was the PWR fuel assembly. For this, a standard Westinghouse 17 x 17 PWR assembly was used. This assembly was chosen to be consistent with the source data provided by Comanche Peak Nuclear Power Plant (CPNPP) [38]. Also, Westinghouse 17 x 17 assemblies have been used in the commercial nuclear industry for the past 30 years, thereby making this a good choice for analysis [39]. The dimensions of the assembly were sourced from publicly available sources [39]. The fuel was uranium dioxide ( $\text{UO}_2$ ) pellets inside of Zircalloy-4 cladding. These rods were assembled in a 17 x 17 structure to form the assembly. In addition, there were 25 unfueled positions. Fuel assembly dimensions are provided in Table 3-2 and a cross section of the assembly obtained using VISED software is shown in Figure 3-2. In Figure 3-2(b), the axial profile of the fuel is shown where the top and bottom white spaces represent the plenum. The middle, which is blue, is the active volume containing the fuel.

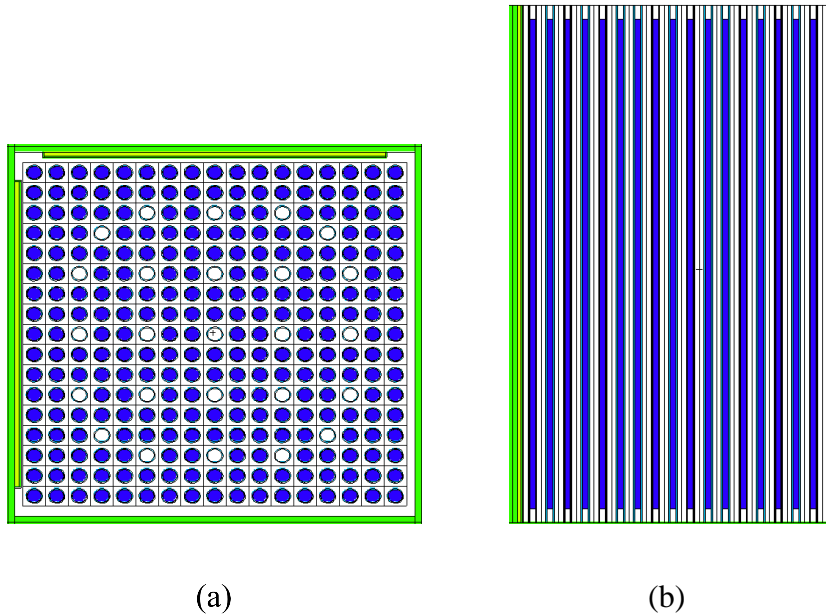
In this study, the helium gap between the fuel and the cladding was not modeled. Also, all the fuel assembly hardware and structural details like nozzles and grid spacers were neglected.

Initial cask loadings used rods and assemblies with identical parameters for ease of simulation. Following that, the loading patterns of the cask were varied based on data obtained from the Next Generation Safeguards Initiative spent fuel libraries [8]. Also, fuel burnup simulations to obtain the neutron source term were carried out using the

ORIGEN2 code for burnup values of 10, 20, 30 40, 45 and 50 GWD/MTU and cooling times of 3 and 5 years.

**Table 3-2 Dimensions of a Westinghouse 17 x 17 fuel assembly**

<b>Parameter</b>	<b>Dimensions (cm)</b>
Pellet outer radius	0.3922
Fuel rod outer radius	0.4572
Cladding thickness	0.0572
Fuel rod pitch	1.2598
Active fuel height	381.0000
Guide tube outer radius	0.4000
Guide/instrument tube thickness	0.0572
Fuel density (g/cm <sup>3</sup> )	10.4600
Number of fuel rods	264
Number of guide tubes	25



Component	Color
Fuel	Blue
Stainless Steel	Green
Boral	Yellow-Green
Air	

**Figure 3-2 17x17 PWR assembly inside the dry cask MPC basket from a (a) cross section view and (b) axial view**

### 3.1.2. Neutron Source Term

The neutron source term was developed based on information provided by Comanche Peak Nuclear Power Plant (CPNPP) [40]. Each assembly has a neutron source strength of  $4.74\text{E}+08 \text{ n.s}^{-1}$  therefore, the total source strength of the 32 PWR SNF assemblies is  $1.52\text{E}+10 \text{ n.s}^{-1}$ . Table 3-3 shows the energy dependent neutron source strength for each SNF assembly. Depending on the fuel assembly diversion scenario, the

neutron source strengths are altered in the MCNP model to accommodate for the difference in the number of SNF assemblies within the dry cask. The initial  $^{235}\text{U}$  enrichment of fuel was given to be 4% with a burnup of 45 GWd/MTU and had a cooling period of three years.

**Table 3-3 Energy dependent neutron emission rate for a single three-year cooled PWR SNF assembly with a burnup of 45 GWD/MTU**

Neutron Energy range (MeV)	Source Strength (n.s <sup>-1</sup> )
0.10 - 0.40	1.80E+07
0.40 - 0.90	9.21E+07
0.90 - 1.40	8.43E+07
1.40 - 1.85	6.21E+07
1.85 -3.00	1.09E+08
3.00 - 6.43	9.96E+07
6.43 - 20.0	8.84E+06
Single Assembly	4.74E+08
32 Assemblies	1.52E+10

### 3.2. ORIGEN2 Fuel Burnup Simulations

ORIGEN2 is a computer code system developed by Oak Ridge National Laboratory and used to perform one-energy group fuel burnup and depletion calculations [41]. This code was chosen as it can quickly determine the neutron emission data from spent nuclear fuel for varying fuel burnups since the data provided earlier was only for 45 GWd/MTU.

In this work, ORIGEN2 was used to estimate the total neutron emission rate of a PWR fuel assembly for burnups of 10, 20, 30, 40, 45, and 50 GWd/MTU. The values obtained are given in Table 3-4.

**Table 3-4 Neutron source emissions per assembly for various burnup steps using 3-year and five-year cooling periods**

Burnup (GWd/MTU)	$(\alpha, n)$ [n.s <sup>-1</sup> ]		Spontaneous Fission [n.s <sup>-1</sup> ]		Total [n.s <sup>-1</sup> ]	
	3 year	5 year	3 year	5 year	3 year	5 year
10	3.54E+05	3.86E+05	6.47E+05	6.11E+05	1.00E+06	9.98E+05
20	9.49E+06	8.87E+06	9.49E+06	8.87E+06	1.90E+07	1.77E+07
30	3.86E+06	3.32E+06	8.54E+07	7.60E+07	8.92E+07	7.94E+07
40	8.05E+06	7.63E+06	3.50E+08	3.22E+08	3.58E+08	3.30E+08
45	1.18E+07	1.11E+07	6.20E+08	5.72E+08	6.32E+08	5.83E+08
50	1.67E+07	1.56E+07	6.20E+08	5.72E+08	6.36E+08	5.88E+08

From Table 3-4, it is seen that as the burnup increases, the neutron emission rate also increases. Additionally, the dominant methods of production of neutrons in SNF are ( $\alpha$ , n) and spontaneous fission.

Using ORIGEN2 the total neutron source term obtained for a single PWR fuel assembly that has a 45GWd/MTU burnup with 3 years of cooling is  $6.32\text{E}+08 \text{ n.s}^{-1}$ . However, for all the calculations performed in this work using the same burnup and cooling time, the neutron source strength of  $4.74\text{E}+08 \text{ n.s}^{-1}$  is used to be consistent with the data provided by CPNPP.

## 4. CONCEPTUALIZATION OF SNF ASSEMBLY DIVERSION SCENARIOS AND THE USE OF MCNP

### 4.1. SNF Assembly Diversion Scenarios

This chapter is dedicated to describing the concept of SNF assembly diversions and the methodology used for quantification of neutron signal from the RMSs. First, the objective of IAEA safeguards is the timely detection of the diversion of significant quantities of nuclear material from peaceful nuclear activities to the manufacture of nuclear weapons or of other nuclear explosive devices or for purposes unknown, and the deterrence of such diversion by the risk of early detection [21]. Diversion of nuclear material is the undeclared removal of declared nuclear material from a safeguarded facility [6].

In this study, a full dry cask contains 32 PWR SNF assemblies. In order to verify the effectiveness of both the proposed RMSs, various SNF assembly diversion scenarios were analyzed. One significant quantity of plutonium is 8 kg. By diverting two PWR SNF assemblies from the dry cask, one can obtain one SQ of Pu. However, in order to make the RMSs more sensitive to SNF assembly diversions, they have been optimized to detect the diversion of even a single SNF assembly. In addition, once diverted, the SNF assemblies could be substituted with dummy metallic assemblies to eliminate the possibility of detecting the diversion using a simple weight measurement of the cask. The dummy would have the same mass and dimensions of the diverted assembly but not the radiation characteristics. For the following cases, abrupt diversion is considered.

Abrupt diversion is the removal of 1 SQ or more of nuclear material in a short time that is less than the material balance period between two IAEA inspections. On the other hand, protracted diversion refers to the removal of the nuclear material in very small quantities (less than 1 SQ) over one material balance periods. In order for a diversion of SNF to occur, the diversion pathway involves opening the dry cask lid, removing the SNF assembly and replacing it with a dummy assembly.

There are eight diversion scenarios (DS) considered, and these are shown in Figure 4-1. DS1 through DS5 refer to the diversion of a single SNF assembly, while DS6 through DS8 are diversions of two SNF assemblies. In addition to these, there is also a no diversion case (RS), where all 32 SNF assemblies are present, that serves as a reference simulation. Finally, DS0 refers to a case where the top concrete lid of the dry cask is removed but no SNF assembly diversion has taken place. Hence, for both DS0 and RS, 32 SNF assemblies are present, as shown in Figure 4-1. The MCNP6 code is used to perform the neutron transport simulations by creating an input file that represents a 3-D high fidelity model of the dry cask with SNF assemblies and the two RMS designs proposed. The positions of the detectors and the shielding dimensions surrounding them are optimized from previous work [42,43].

For initial sensitivity analyses, the SNF used was homogenized in every assembly. They had the same materials, neutron source strength, energies and loading pattern. This allowed for the assumption of symmetry to hold true such that diversions in any locations for DS1-DS5 can be equivalent to removing any of the 32 assemblies. This configuration is depicted in Figure 4-2. The numbers represent the diversion scenarios –

hence due to symmetry, the response of diversions from these positions can be used to predict the response in other diversion positions within the dry cask.

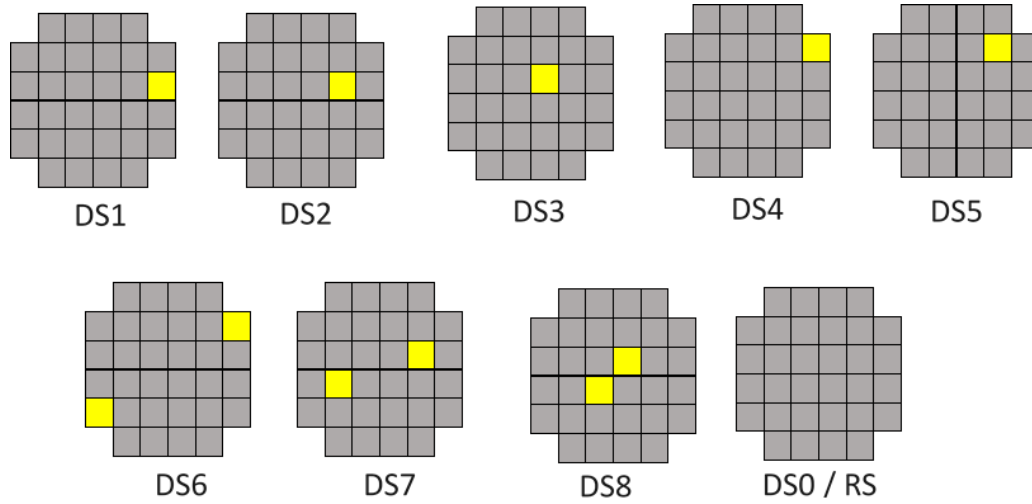


**Figure 4-1 Diversion scenario (DS) configurations where the yellow cell indicates the position of the substituted assembly where the diversion has occurred**

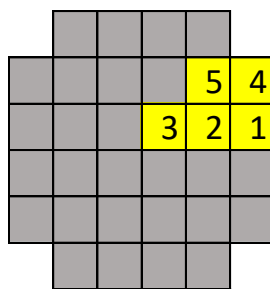


**Figure 4-2 Diversion scenarios 1, 2, 3, 4, and 5 in a dry cask that can be used for symmetrical purposes**

#### **4.2. Overview of MCNP Simulations for SNF Diversion Scenarios**

To obtain a total thermal neutron signal from a complete dry cask, all 32 SNF assemblies were modelled. However, to estimate the contribution from each assembly to the neutron signal recorded by the RMS, the neutron emissions were simulated only one assembly at a time. The remainder of the dry cask (31 assembly positions) were filled with dummy assemblies (fresh fuel assemblies with no neutron emissions). The sum of neutron signal from 32 individual simulations was considered as the reference scenario, RS. Corresponding SNF assembly diversion scenarios responses were calculated by summing the SNF assembly contributions from all locations except from those that were diverted. This follows the superposition principle in the Green's function such that the total neutron flux from multiple sources at the same time is equal to the sum of the flux from each source individually [44]. The uncertainties were propagated accordingly.

#### **4.3. Overview of MCNP Simulations for both RMS Design Analyses**

In order to simulate expected neutron count rates from the detectors in both RMSs, separate MCNP input decks were created for each RMS type, and each diversion scenario. The geometry of the dry cask remained the same for all MCNP simulations with the exception of dummy assembly substitutions for the diversion scenarios.

In order to obtain neutron flux in the detectors, averaged cell flux (F4 tally) is employed. Equation 4-1 describes how the tally is scored.  $\Phi(r, E, \Omega)$  represents the energy and angular distribution of the flux as a function of position. If a particle of

weight,  $W$  and energy,  $E$  make a track length (segment),  $T$  within a specified volume,  $V$ , then that segment contributes  $WT/V$  to the cell flux. The sum of these contributions is reported in the output.

$$F4 = \frac{1}{V} \int_V dV \int_E dE \int_{4\pi} d\Omega \Phi(r, E, \Omega) \quad \text{Eq. 4- 1}$$

The results of an F4 tally are in units of particles.cm<sup>-2</sup> (source particle)<sup>-1</sup>:

$$F4 = \frac{\frac{\text{neutron track length (cm)}}{\text{volume (cm}^3)}}{\text{source particle}} = \frac{\frac{\text{neutron}}{\text{cm}^2}}{\text{source particle}}$$

where the source particle is the source strength – which is number of neutrons per second emitted by the SNF assemblies. Once multiplied by the source strength, an absolute neutron flux is obtained, which can be divided into neutron energy groups as well.

In addition to average cell flux tallies, there is an option to couple this tally with mesh tallies. Mesh tally results can be used to graphically display the neutron flux, dose or other quantities on a rectangular, cylindrical, or spherical grid overlaid on top of the standard problem geometry [34]. The mesh tallies employed in this dissertation use rectangular coordinates by using FMESH and specifying CORA, CORB and CORC. CORA entries represent planes perpendicular to the x-axis, CORB entries are planes perpendicular to the y-axis, and CORC entries are planes perpendicular to the z-axis. Also, the mesh tallies are energy binned to separate the thermal neutron flux from the rest. This is done to estimate the count rate predicted by the detectors within the RMS.

The mesh tallies used in this work employ cell average flux, F4 type tallies across the mesh. Hence, have the same working principle governed by Equation 4-1.

The energy group structure used to bin the tallies is shown in Table 4-1. For both the RMS designs, thermal neutron detectors are used to obtain the neutron signal emitted by the SNF assemblies, hence the energies of interest are the thermal neutrons below 0.025 eV. Including the cadmium neutrons (0.025 eV – 0.5eV) will provide more flux recorded in the detectors which will better the statistics by decreasing the associated uncertainties, hence lowering the non-detection ( $\beta$ ) probabilities for diversion scenarios. However, a more challenging approach is taken by assuming the detector only interacts with the thermal neutrons below 0.025 eV. Since the RMS can detect diversion scenarios in a reasonable time (< 5 minutes) using a smaller fraction of thermal neutrons, including the cadmium neutrons will only better the results. Thus, for all simulations performed using the internal and external RMS with dry casks, only the interactions below 0.025 eV are considered.

**Table 4-1 Neutron energy group structure used for calculation of external and internal RMS response**

<b>Energy range</b>	<b>Energy group boundaries (MeV)</b>
Thermal neutrons	0.00E-00 - 2.50E-08
Cadmium cutoff neutrons	2.50E-08 - 5.00E-07
Intermediate neutrons	5.00E-07 - 1.00E-03
Fast neutrons	1.00E-03 - 2.00E+01

Additionally, the energies of interest are the thermal neutrons below 0.025 eV. Including the cadmium neutrons (0.025 eV – 0.5eV) will provide more flux recorded in the detectors which will better the statistics by decreasing the associated uncertainties, hence lowering the  $\beta$  probabilities for diversion scenarios. However, a more challenging approach is taken by assuming the detector only interacts with the thermal neutrons below 0.025 eV. Since the RMS can detect diversion scenarios in a reasonable time (< 5 minutes) using a smaller fraction of thermal neutrons, including the cadmium neutrons will only better the results. Thus, for all simulations performed using the internal RMS and dry casks, only the interactions below 0.025 eV are considered.

#### **4.3.1. Variance Reduction Techniques**

To achieve stochastic statistical convergence for the tally values used in MCNP as well as to minimize total simulation time, variance reduction schemes such as geometry splitting, Russian roulette (through spatial importance sampling) and analog capture are used. The goal of variance reduction is to improve the tally precision, uncertainty in the mean, by increasing the history-scoring efficiency of the tally and decreasing the spread of nonzero history scores [45].

##### **4.3.1.1. Geometry Splitting and Russian Roulette**

Geometry splitting is a variance reduction technique that samples more particles in the spatial region of interest resulting in improved stochastic statistical convergence of the tally. In general, splitting is applied in regions that are expected to significantly contribute to the quantity of interest which are unlikely to reach these regions if an

analog Monte Carlo transport is employed. In important regions, neutrons are split into several neutrons, by using appropriate changes to the value of importance in the input and appropriate neutron weight adjustments.

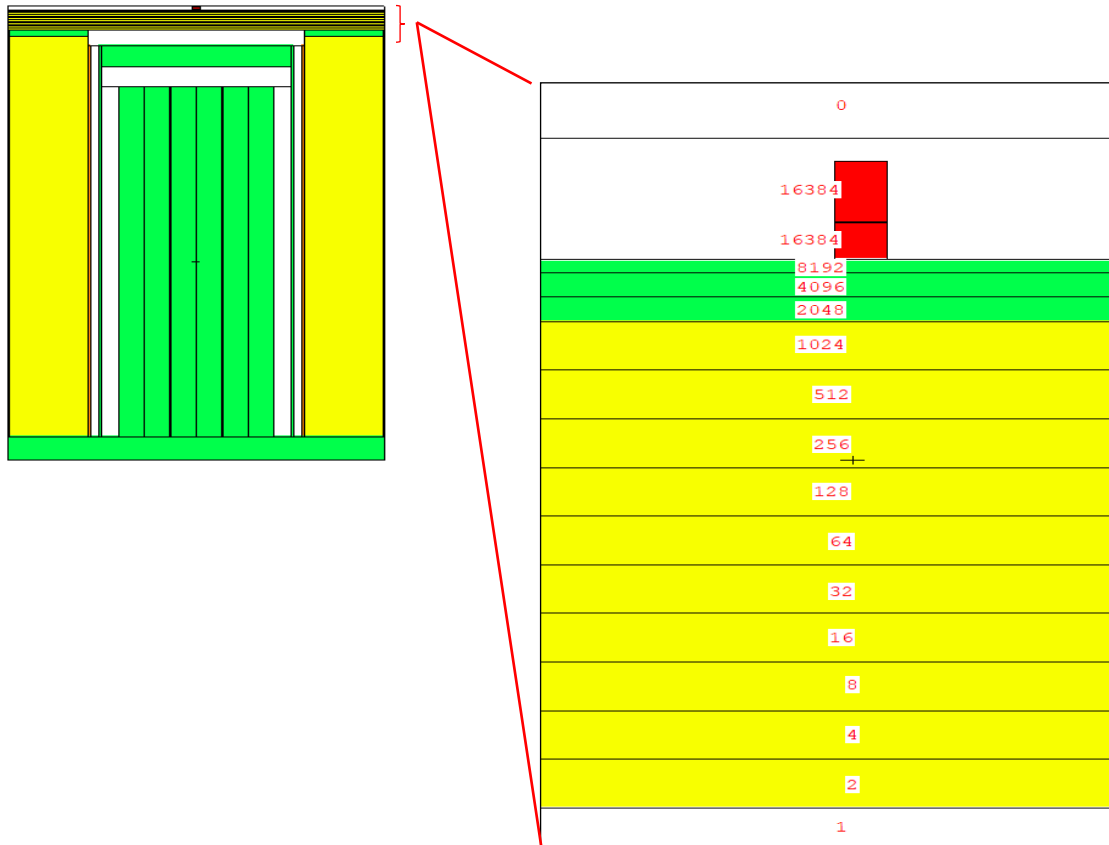


**Figure 4-3 Pictorial representation of importance sampling variance reduction method in the MCNP dry cask model cells.**

Russian roulette is the opposite of splitting. In unimportant regions, the Russian roulette game is played and the neutron's weight is either increased by the reciprocal of the survival probability or the neutron history is terminated [45].

In this dissertation, variance reduction is important in the external RMS to ensure statistically converged tally results. The thickness of concrete in the dry cask lid is 20 cm, followed by a stainless-steel layer of thickness 2.54 cm. Tracking particles through this amount of material provided results with high uncertainties (MCNP relative error > 0.10). In addition to that, it is difficult to obtain convergent results when the detector cell is much smaller than the whole particle transport system. Since the external RMS is much smaller than the entire problem geometry, many particles (that make it through the lid) will miss the detector without making any contributions to the tally.

To overcome this, both, geometry splitting, and Russian roulette variance reduction methods were used in the MCNP input for the concrete lid of the dry cask for the external RMS and the stainless steel MPC lid for the internal RMS. Figure 4-3 shows a Visual Editor rendering of the dry cask with importance sampling for the external RMS. The numbers in red represent the importance ascribed to each region in the MCNP input. The concrete material in the lid is partitioned into ten 2 cm thick layers. Each layer is assigned an importance higher than the one prior by a factor of 2. For instance, the first layer has an importance of 2, second has an importance of 4, and third has an importance of 8 and so on. Stainless steel material is divided into 3 layers where the first two layers are each 1 cm thick and the third is 0.54 cm. Since the stainless steel is on top of the concrete, the importance sampling number goes up by a factor of 2 for each layer with reference to the last (tenth) layer of concrete. When using this importance sampling variance reduction technique, it is important critical to keep the ratio of adjacent cell importance values to less than 4 for better tally convergence.

#### **4.3.1.2. Analog Capture (CUT:n)**

When using importance biasing (or importance sampling) with geometry splitting, it is crucial to change the default neutrons from implicit capture to analog capture. In an analog random walk simulation, the energy deposited inside a given volume is an unbiased estimate of the flux tallies integrated over the volume [46]. If a considerable fraction of the simulated particles crosses the detector cell, the method is efficient. However, that is not the case with the external RMS, making implicit capture extremely inefficient. The use of analog capture prevents low weight neutrons generated from being overly killed by Russian roulette from the default weight cutoff [47]. Analog capture is implemented in the MCNP input using the CUT:n card feature. The CUT card specifies a minimum energy, time and particle weight below which the particle is killed. The parameters used in these simulations were 'CUT:n 2j 0 0' where n represents neutrons, 2j represents default entries of time (very large) and energy (0 MeV) followed by the weight cutoffs which are specified as zero.

#### **4.3.2. Effect of Variance Reduction Techniques on the External RMS Results**

MCNP uses ten statistical checks to assess the statistical convergence of each tally based on the results for the estimated mean, relative error (R), variance of variance (VOV), figure of merit (FOM), and slope of the largest history scores of  $f(x)$  [47]. The checks are:

- Mean should not have an increasing or decreasing trend as a function of number of particles, N, simulated.
- Magnitude of R is  $< 0.10$  for a non-point detector tally.

- R monotonically decreases as a function of N.
- $1/\sqrt{N}$  decrease in R as a function of N.
- Magnitude of VOV is  $< 0.10$  for all types of tallies.
- VOV monotonically decreases as a function of N.
- VOV decreases as  $1/N$ .
- FOM is statistically constant as a function of N.
- Nonmonotonic behavior in FOM as a function of N.
- The slope of the top 25 to 201 largest history scores, x, should be  $>3.0$  such that the second moment existence requirement of the central limit theorem is satisfied.

The FOM is the best measure of computational efficiency. It is calculated using Equation 4-2.

$$\text{FOM} = \frac{1}{\text{Time} \cdot R^2} \quad \text{Eq. 4- 2}$$

The effect of variance reduction on the 10 statistical checks for the external RMS for various configurations is shown in Appendix B. Figure 4-4 shows the FOM for various configurations of the external RMS (this was prior to a final size being selected). The 2x2, 4x2, 3x3 and 4x4 represent detector configurations with 4, 8, 9 and 16 detectors respectively. It also shows the FOM for the Reference Simulation (RS) labelled 'Full' and all the diversion scenarios labelled 'DS'. DS0 was not included as the variance reduction was performed on the lid of the cask which is absent in DS0.

Three variations of FOM are shown in Figure 4-4:

- No VR is performed where neither geometry splitting, nor analog capture is used in the problem geometry.
- With VR Geometry Splitting is used where only geometry splitting with importance biasing is used.
- With VR Geometry Splitting + Analog capture is used where both geometry splitting with importance biasing and analog neutron capture is used.

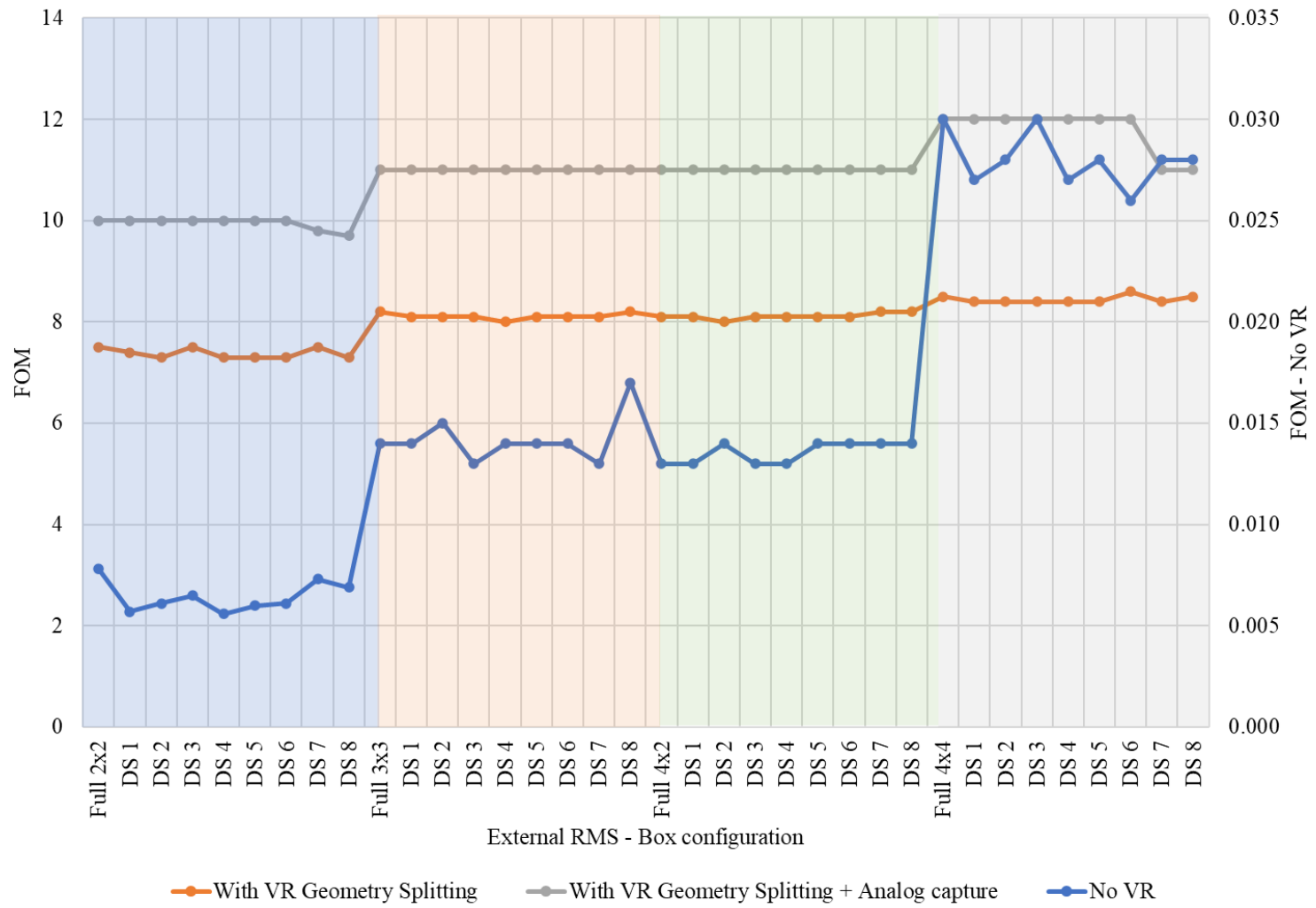


**Figure 4-4 FOM of external RMS box configurations**

From Figure 4-4, the lowest FOM corresponds to the cases with no variance reduction, followed by VR with geometry splitting and finally the highest FOM for VR with geometry splitting and analog capture. The use of geometry splitting and analog capture increased the FOM by a factor of ~1100 for the 2 x 2 configuration which was the smallest detector size case. For the 3 x 3 configuration, the improvement was a factor of ~573, for the 4 x 2 configuration, the improvement was a factor of 599 and the 4 x 4 configuration had an improvement by a factor of 301. In addition, computational time decreased by an average of 14% by employing VR techniques. Thus, based on these results, it is concluded that the use of selected variance reduction schemes significantly improved the computational efficiency of the MCNP simulations performed.

#### **4.4. Statistical Analysis of MCNP Results of Diversion Scenarios**

In order to determine if the proposed RMS designs were viable, statistical analysis was performed based on the output of the neutron detector tally results within the RMSs. The results of detector counts were assumed to follow a Gaussian (normal) distribution around the mean with the uncertainties predicted by MCNP and propagated error in counts. Figure 4-5 shows analysis results of two cases: Reference Simulation (RS) with no diversions and a Diversion Scenario (DS), where an assembly diversion has occurred. In this case, the mean value of detector results,  $\mu_{DS} < \mu_{RS}$ .

The false alarm probability ( $\alpha$ ) is the probability that the RMS detects a SNF assembly diversion when no such diversion occurred. This number is kept at a reasonably low rate (5%) so that the system does not alarm often when SNF assembly

diversions are not happening. If  $\alpha$  was high, the system would produce a lot of false alarms; hence the operator may not trust the system and turn it off / ignore the alarms, thus rendering this design impractical. The value of  $\alpha$  can also be changed to other values, such as setting it to  $1\sigma$ ,  $2\sigma$  or  $3\sigma$  uncertainties from the mean [43] of the RS simulation. It is worth to note that minimizing the false alarm probability will increase the non-detection probability ( $\beta$ ), which is undesired. Striking a balance between these  $\alpha$  and  $\beta$  values is essential. One way to reduce  $\alpha$  without increasing  $\beta$  is to increase the measurement time. A longer measurement time corresponds to higher counts in the detectors, and lower uncertainty, which will make the Gaussian distributions narrower. When this happens,  $\beta$  will not increase. Measurement time is a critical parameter and should be kept reasonable. For this work, measurement times of less than 5 minutes was found to be reasonable.

Next, in order to calculate the alarm threshold (T), the NORMINV function in Microsoft Excel software is used. This function calculates the inverse of the cumulative normal distribution function for a specified false alarm probability ( $\alpha$ ) [48]. A value of 5% was chosen for  $\alpha$  to avoid too many false alarms.

Using the set alarm threshold (T), the non-detection probability ( $\beta$ ) is calculated for each SNF assembly diversion scenario (DS). The non-detection probability is the probability that a diversion is not detected by the RMS when a diversion did occur. This is done by using the NORMDIST function in Microsoft Excel software. This function returns the normal distribution for the specified threshold, mean and standard deviation

[49]. The goal of this work is to keep  $\beta$  less than 20% for every DS as per the recommendation of the IAEA [50].

In order to calculate uncertainties in the Gaussian distribution for all cases, the following was done:

- 1) Perform MCNP simulation of RS and all DS with each RMS.
- 2) Obtain output from MCNP by tallying in the active area of the detectors (cell averaged flux, F4 tallies) within the RMS.
- 3) Convert tally output to counts per second based on manufacturer provided specifications of thermal neutron sensitivity (cps/nv) for the detector used in the corresponding RMS (1 cps/nv for fission chambers in internal RMS and 9.6 cps/nv for eight microstructure semiconductor neutron detectors in external RMS).
- 4) Total uncertainty is calculated by adding MCNP uncertainty and the detector uncertainty as shown in Equation 4-3.

$$\sigma_{\text{total}} = \sqrt{\sigma_{\text{MCNP}}^2 + \sigma_{\text{detectors}}^2} \quad \text{Eq. 4- 3}$$

where:

- $\sigma_{\text{total}}$  = Total uncertainty
- $\sigma_{\text{MCNP}}$  = Stochastic uncertainties in MCNP tallies
- $\sigma_{\text{detectors}}$  = Uncertainties in detector response

It is worthwhile noting that the stochastic uncertainties in MCNP tallies can be minimized by performing variance reduction techniques, hence the large contributor of uncertainties in these calculations are from the detector response i.e  $\nu$ counts.

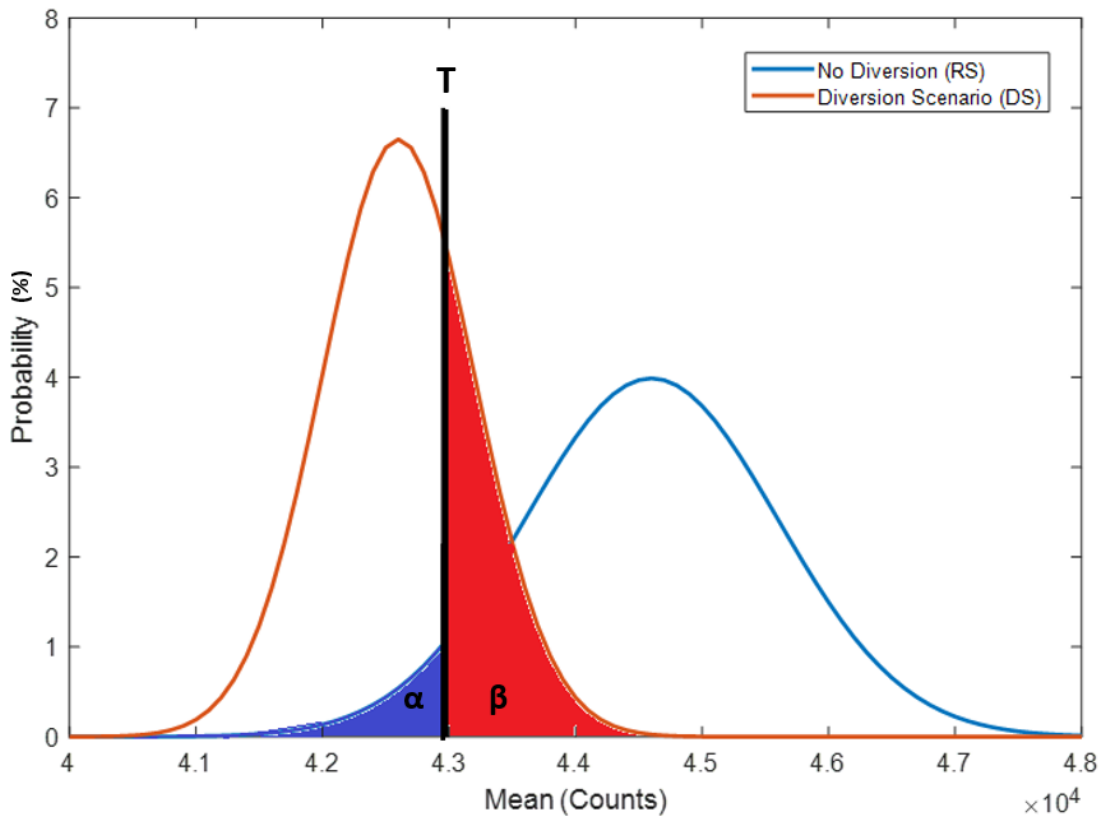


**Figure 4-5 Graphical display of false alarm probability,  $\alpha$  and non-detection probability,  $\beta$  for 5% alarm threshold.**

As previously discussed, both RMS designs modelled in MCNP employ average cell flux tallies (F4) that are energy binned such that the thermal neutron flux is obtained within the detector cells.

Thermal neutron sensitivity is a parameter usually provided in units of  $\frac{\text{counts per second}}{n \cdot v}$  where n is the neutron density, which is the number of neutrons per cubic centimeter (expressed as neutrons/cm<sup>3</sup>), and v is the neutron velocity which is the distance the neutrons travel in 1 second (expressed in centimeters per second, or cm/sec). Consequently, neutron flux (nv) is measured in  $\frac{n}{\text{cm}^2\text{s}}$  [51]. By multiplying the manufacture provided thermal neutron sensitivity value with the thermal neutron flux provided by MCNP, a predicted count rate can be determined as shown in Equation 4-4.

$$\text{Count rate} = \text{Thermal neutron sensitivity} \left( \frac{\text{cps}}{\frac{n}{\text{cm}^3} \cdot \frac{\text{cm}}{\text{s}}} \right) \times \text{Flux} \left( \frac{n}{\text{cm}^2\text{s}} \right) \quad \text{Eq.4- 4}$$

The total counts obtained by the detectors is obtained by multiplying the count rate by the measurement time. The total counts obtained are used to plot the Gaussian distributions shown in Figure 4-5 with their associated uncertainty values. From there the false alarm probability,  $\alpha$  and non-detection probability,  $\beta$  are calculated. The measurement time is determined by finding the time that corresponds to the first instance that all the  $\beta$  probabilities for all diversion scenarios is less than 20%.

## 5. DEVELOPMENT OF THE REMOTE MONITORING SYSTEM CONFIGURATIONS

### 5.1. Procedure

Khudoleeva et al. had developed a preliminary design for a RMS deployed inside the dry cask prior to it being sealed [52]. Using that design concept, the objective of this work was to optimize the internal RMS by adjusting the dimensions of its components in order to improve the non-detection probabilities ( $\beta$ ) for SNF assembly diversions previously achieved [53]. Khudoleeva's work did not consider assemblies with different loading patterns, fuel burnups and multiple cask scenarios, which this work will address. In addition, a second RMS design is proposed to be placed on the exterior of the dry cask using different detectors. For this second approach, the detector was optimized, and all  $\beta$  probabilities were calculated for assembly diversion scenarios.

In order to come about a preliminary design for an RMS, the following steps were performed.

Define design requirements by:

- Determining inherent limitations of dry cask storage systems
- Investigating the neutron flux behavior in areas of interest in and around the dry cask

Optimize previously proposed internal RMS by:

- Changing the amount of shielding surrounding the detectors
- Determining the width of cadmium to be placed within the RMS

Design new external RMS by:

- Investigating the feasibility of the concept
- Selection of detectors
- Optimization of detector array and placement of detectors

The following sections will describe in detail each of the steps taken to arrive at a final design for both the internal RMS and the external RMS.

## **5.2. Monitoring Limitations of SNF Dry Casks**

Since the 1980s, it has been evident that monitoring the condition of SNF inside dry casks without exposing the fuel has been a huge challenge [41]. The cask is designed to shield the radiation within such that the dose rates outside comply with the safety regulations set by the competent authority. The US Code of Federal Regulations, 10 CFR Part 72, requires that spent fuel storage and handling systems be designed with adequate shielding thickness to provide sufficient radiation protection under normal, off normal and accident-level conditions[55]. While this is great from a radiation safety standpoint, it becomes a challenge for nuclear safeguards perspective to maintain the CoK once the cask is sealed.

Hence, a two-pronged approach is used to achieve the goal of maintaining CoK after a dry cask has been sealed. Both approaches (internal and external RMS) will be discussed in the following sections. In general, the RMS should facilitate in the following monitoring in the following ways:

- Reduce number of on-site inspections to the IAEA/regulating body

- Provide CoK after the sealing of the dry cask and must be highly reliable
- Remain cost effective (< 1% cost of the dry cask)

### **5.3. Proposed RMS Approaches**

The first approach involves using an internal RMS which is placed inside the dry cask – in the air gap between the MPC and lid prior to being sealed. The RMS will stay within the cask for its lifetime and continually report information regarding the contents of the cask to the IAEA. While the internal RMS will be placed outside the MPC, it is still exposed to high neutron and gamma radiation. Hence, it is imperative that the RMS should be able to withstand a high radiation environment and last approximately 40 years (with relicensing of the dry cask every 20 years) [56,57]. This approach can be used for dry casks that are yet to be sealed.

The second approach is the use of an external RMS. This RMS will be placed outside the dry cask on its lid after it has been sealed. While dry casks are designed to shield radiation, there are still radiation signatures that escape which can be used to provide information regarding the SNF inside the dry cask [23]. This system will be placed outside the dry cask and can be moved when necessary. A fingerprint will be taken once a cask is sealed, then measurements can be taken whenever necessary at a later time. For instance, upon sealing the cask, these detectors are placed on the lid. They can stay there and continually monitor progress or they can be removed and placed back when reverification is needed. The initial fingerprint and the new fingerprint are

compared to determine if any changes to the signal in the reference timeframe is noticed after the appropriate correction for temporal decay is done.

#### **5.4. Neutron Flux Inside a Dry Cask**

In this section, the neutron flux calculations inside and around the dry cask is quantified using MCNP simulations by utilizing mesh tallies.

For the internal RMS design, previous work located this RMS inside the air gap between the MPC lid and the concrete [52]. This is shown in Figure 5-1. The yellow box represents the air gap where the RMS is placed inside a dry cask. The height of this gap is 18 cm. The two red lines denote the positions of the mesh tallies, FMESH performed in MCNP. The top position mesh tally is underneath the concrete lid (at the top of the air gap) and the bottom position mesh tally is above the MPC lid (at the bottom of the air gap). The results of the mesh tallies are shown in Figure 5-2

In Figure 5-2, the x and y-axes represent the position in centimeters (cm) while the color denotes the thermal neutron flux in  $n. cm^{-2}s^{-1}$  where yellow is high and blue is low. In this simulation, 32 SNF assemblies are present in the dry cask and all assemblies are homogenous and have a burnup of 45 GWd/MTU and a cooling time of 3 years. Figures 5-2 (a) and (b) have a maximum thermal flux in the center of the cask of approximately  $1.6E+03 n. cm^{-2}s^{-1}$ .

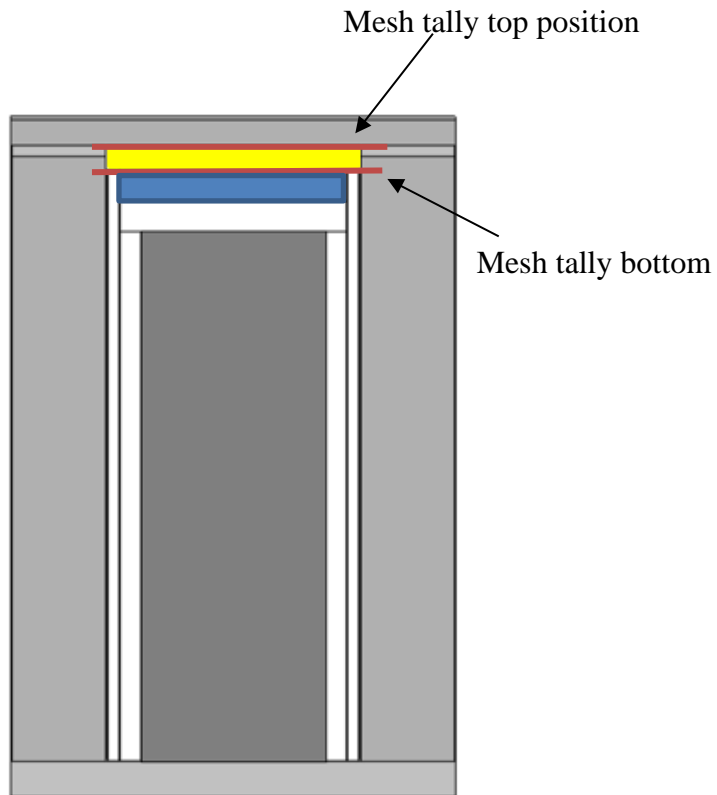
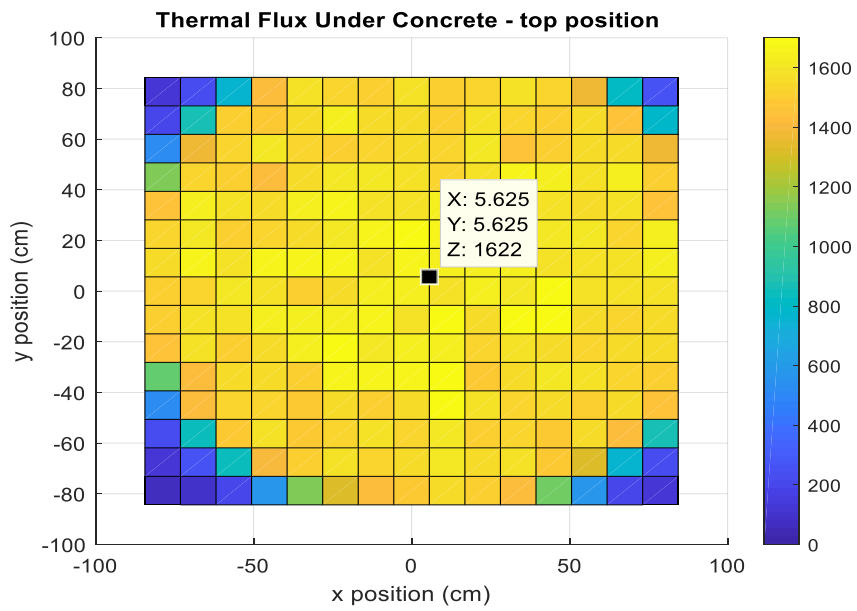


**Figure 5-1 Internal RMS location denoted by yellow box and mesh tally positions by red lines. Blue box denotes MPC lid**

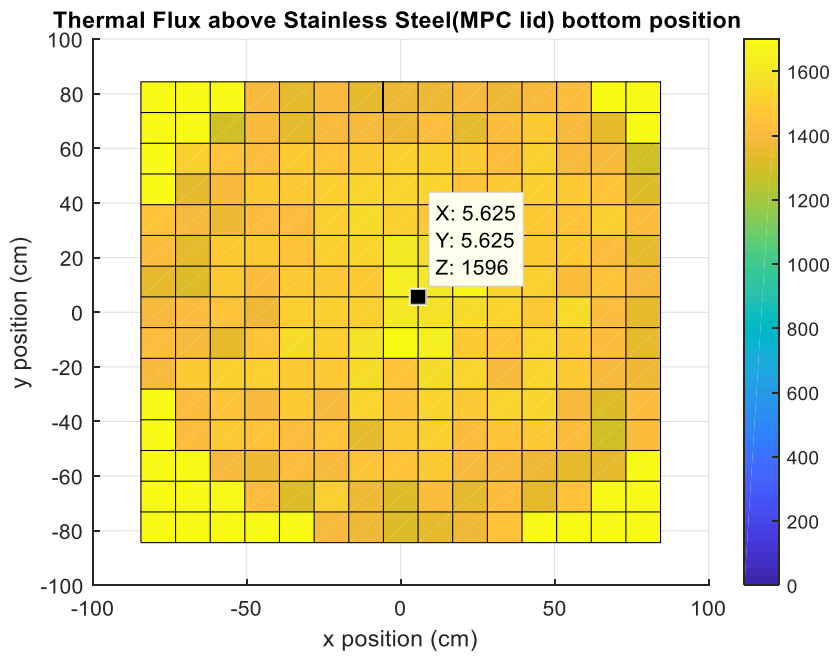
The thermal flux is lower on the periphery compared to the center because of the leakage of neutrons into the concrete is more probable from the peripheral SNF assemblies than the middle ones hence the leaked neutrons in the periphery do not contribute to the mesh tallies on the top. From these mesh tallies shown in Figure 5-2, the characteristic thermal neutron flux is calculated with self-shielding from surrounding assemblies but without attenuation from the dry cask lid. It is concluded that the thermal neutron flux is high in the air gap due to the thermalization and reflection of fast neutrons in the concrete lid. Concrete has a high hydrogen content that aids in

thermalizing fast neutrons emanating from spontaneous fission and alpha radiation interactions with oxygen in the SNF material.

Also, the thermal flux in the top mesh position (Fig 5-2(a)) is slightly higher than that in the bottom mesh position (Fig. 5-2 (b)). This is because more thermalized neutrons are entering the top mesh compared to the bottom mesh due to the proximity to the concrete lid leading to relatively large number of scattered neutrons reaching the top mesh tally region rather than the lower mesh tally region. Finally, the bottom position mesh (Fig. 5-2 (b)) has a higher thermal flux in the corners compared to the center as the corners are located past the MPC within the concrete canister. Hence, the difference is noticeable for the parts under the MPC lid versus in the corners which are within concrete.



(a)



(b)

**Figure 5-2 Thermal flux mesh tallies at the (a) top and (b) bottom positions**

**Table 5-1 Energy dependent flux tallied below and above the stainless steel MPC lid and corresponding transmission factor**

Upper Energy Bin Limit (MeV)	Below Stainless Steel		Above Stainless Steel		% Transmission
	Flux (n.cm <sup>-2</sup> .s <sup>-1</sup> )	MCNP Stochastic Error (n.cm <sup>-2</sup> .s <sup>-1</sup> )	Flux (n.cm <sup>-2</sup> .s <sup>-1</sup> )	MCNP Stochastic Error (n.cm <sup>-2</sup> .s <sup>-1</sup> )	
2.50E-08	7.14E+01	1.45E+00	1.45E+03	6.23E+00	2027
5.00E-07	1.30E+03	6.35E+00	7.54E+03	1.58E+01	582
2.00E+01	2.49E+05	1.25E+02	5.93E+04	5.93E+01	24
Total	2.51E+05	1.25E+02	6.83E+04	6.15E+01	27

In addition, Table 5-1 shows the energy dependent flux tallied below and above the stainless steel MPC lid (shown in blue in Figure 5-1). The flux is calculated using F4 tallies in a 1 cm thick cylinder with the same radius of the MPC lid in two positions: above and below the MPC lid. The neutron flux tally is energy binned to represent the thermal neutrons (0-0.025 eV), cadmium cut off thermal neutrons (0.025 eV- 0.5 eV) and intermediate/fast neutrons (0.5 eV – 20 MeV). For calculating the response of the thermal neutron detectors in both RMS designs, only the thermal bin is used. The rest of the bins is used for optimizing additional materials in the RMS designs. While thermal neutron detectors respond to neutrons that are in the epithermal and cadmium cutoff region of energies, a conservative approach is taken to determine the response of the

RMSs with only thermal neutrons. Increasing the energy range will only increase the number of counts recorded by the detectors and hence improve the statistics.

From Table 5-1, it is seen that there is a total reduction in neutron flux of 73% as only 27% of all the neutrons make it through the MPC lid. The MPC lid is made of 24 cm of Stainless Steel-304. Looking into the composition of this material,  $^{56}\text{Fe}$  makes up the largest fraction of the alloy. The total neutron cross-section is the likelihood that a neutron of a certain energy will interact with a target nucleus. These cross-sections can vary greatly with the kinetic energy of the neutron. Appendix C shows the neutron elastic scattering and radiative capture cross sections for  $^{56}\text{Fe}$ . It can be seen that elastic scattering cross section is constant for energies up to  $\sim 10$  keV. However, for all energies between 10 keV and 2.2 MeV, there is resonance structure that occurs such that the scattering cross section increases. For all intermediate/fast neutrons, the scattering cross section in  $^{56}\text{Fe}$  is higher than the absorption cross section. This proves that the intermediate/fast neutrons undergo a lot of scattering and are thermalized. The thermalized neutrons do not get captured in stainless steel as their mean free path is large. This also contributes to the high thermal flux in the void region above the MPC lid in addition to the reflection in concrete which increases the value of the tallied neutron fluxes. The relatively high thermal neutron flux in this region makes the air gap a suitable position for the internal RMS.

### 5.5. Neutron Flux Outside Dry Cask

The external RMS design proposed is housed on the top of concrete lid of the dry cask. When deciding on the placement of this RMS, two locations were considered: on the top of the lid and around the body (radially). This is shown in Figure 5-3, where the blue regions represent potential locations for the external RMS. From a literature review, it was found that SNF assemblies tend to shield each other and prevent the radiation signatures from escaping, hence making it a challenge to detect internal SNF assemblies using detectors placed on the radial periphery as shown in Figure 3(b). This would be an issue for detecting diversions of SNF assemblies from central locations [33].

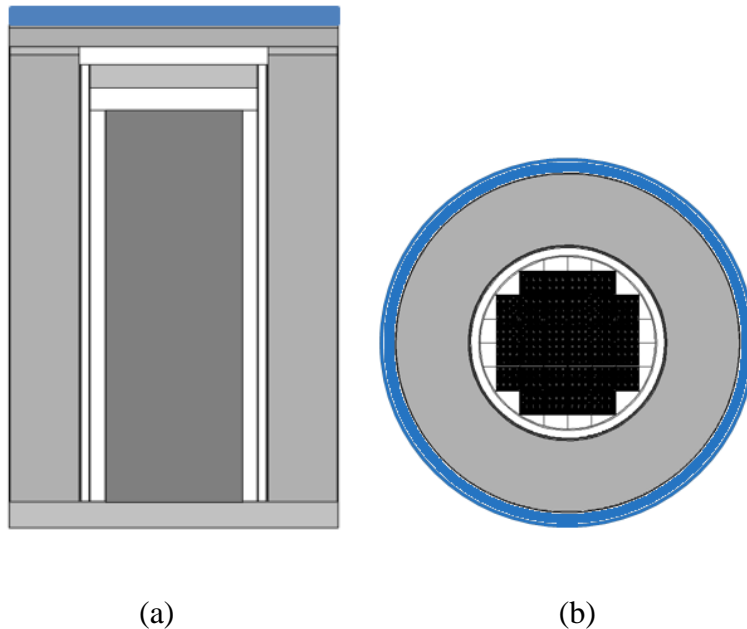


**Figure 5-3 Location for external RMS shown in blue on (a) the lid of the dry cask and (b) around the body**

From past studies, [8,58] it was shown that when a diversion of an internal assembly (not near the circumference) occurs, the odds of detecting that diversion is very low if the detectors are placed on the outside of the dry cask radially (Fig. 4-3.b). In that conceptual study, one hundred  $^4\text{He}$  neutron detectors were placed around the dry cask radially to obtain radiation signal about the contents of the dry cask. However, the study proved that the internal assembly diversions were difficult/impossible to detect.

Hence, in this study, the neutron flux profile on the top of the lid of the dry cask is investigated as a potential location for placement of the external RMS. The neutron flux is calculated using MCNP F4 tallies in a 1 cm thick cylinder with the same radius of the outer cask. The energy dependent neutron fluxes were tallied and are given in Table 5-2.

**Table 5-2 Energy dependent neutron flux on the lid of a dry cask**

<b>Upper Energy Bin Limit (MeV)</b>	<b>Flux (n.cm<sup>-2</sup>.s<sup>-1</sup>)</b>	<b>MCNP Stochastic Error (n.cm<sup>-2</sup>.s<sup>-1</sup>)</b>
2.50E-08	1.71E+01	2.07E-01
5.00E-07	1.66E+02	7.47E-01
1.00E-01	3.69E+02	1.33E+00
2.00E+01	6.67E+01	7.52E-01
Total	6.18E+02	1.73E+00

From Table 5-2 it can be noted that the thermal neutron flux (<0.025 eV) exiting the cask is  $\sim 17 \text{ n. cm}^{-2}\text{s}^{-1}$ . This neutron flux is  $\sim 2$  orders of magnitude lower than that present in the internal RMS void location. Since the neutron flux is quite low, it would require long measurement times to get good statistics for the external RMS to be able to detect diversions of SNF assemblies. However, the thermal neutron energy bin only contributes 2.76% of the total neutron flux exiting the cask through the lid. The intermediate/ fast neutrons make up a large portion of the flux exiting the cask; thus, polyethylene moderation is placed on the top of the lid to increase the fraction of thermal neutrons by moderating the intermediate/fast neutrons.

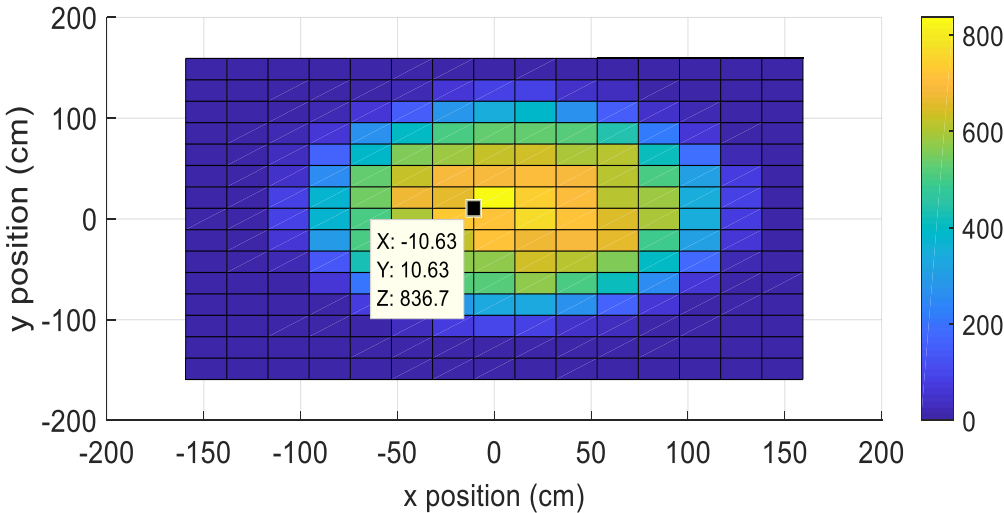


**Figure 5-4 Thermal neutron flux on the dry cask lid**

It is seen that in the final RMS configuration with 1.5 cm of polyethylene on top of the lid and 2.5 cm above the detectors, the thermal flux increased by >1300%. The optimization of polyethylene will be discussed in the following sections. Figure 5-4 shows the thermal neutron flux map on the top of the cask lid with optimized polyethylene moderation. The mesh had a thickness of 0.5 cm and spanned over the entire lid. As expected, the thermal neutron flux is highest in the center of the cask compared to the periphery due to presence of SNF in the center. The maximum thermal neutron flux is  $836.7 \text{ n. cm}^{-2}\text{s}^{-1}$ , making the lid a suitable position for the external RMS.

## **5.6. Internal RMS**

The internal RMS consists of two fission chamber detectors arranged in a specific configuration to derive optimal neutron radiation signal for identifying SNF assembly diversions. The fission chambers are encased in polyethylene and have a natural cadmium sheet underneath the polyethylene as shown in Figure 5-5.

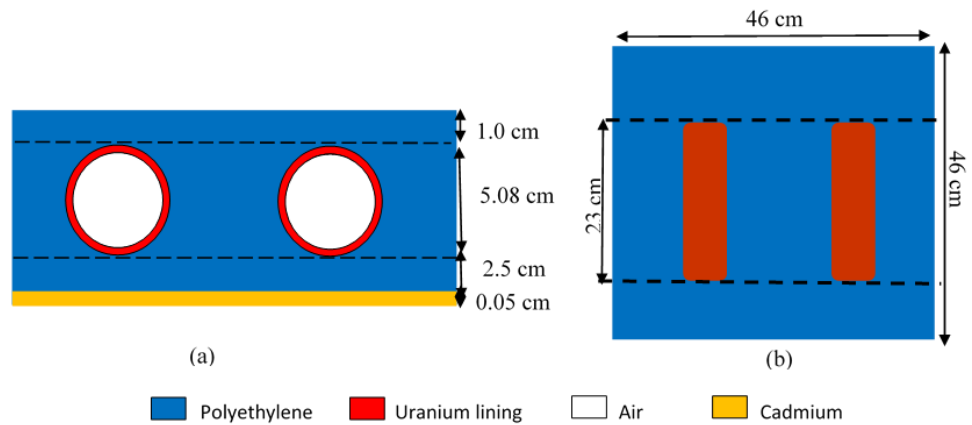


**Figure 5-5 Internal RMS with fission chambers (denoted by uranium lining and air), polyethylene and cadmium shown in (a) front view and (b) top view**

The total height of the internal RMS is 8.63 cm with a width of 46 cm. It is placed in the air gap between the MPC stainless steel lid and the concrete lid of the dry cask. This is shown in Figure 5-6.

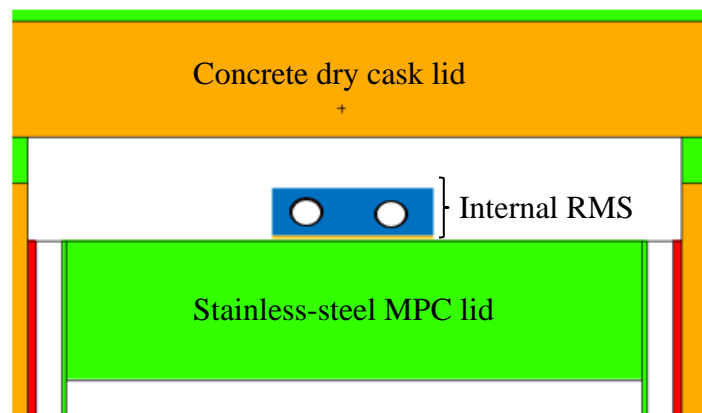


**Figure 5-6 Position of internal RMS within dry cask**

### **5.6.1. Function of Each Component in the Internal RMS**

The RMS components include fission chamber detectors, polyethylene and cadmium. Functionality of each of the RMS components are described below.

#### **5.6.1.1. Fission Chambers - Mode of Operations**

Fission chamber detectors are widely used in the nuclear industry to monitor reactor power and for spent nuclear fuel measurements [59–61]. Hence, these detectors can handle harsh radiation environments (neutron flux of  $5 \times 10^{13} \text{ n.cm}^{-2}.\text{s}^{-1}$  and gamma flux of up to  $10^8 \text{ R/h}$ ) and high temperatures (up to  $300 \text{ }^\circ\text{C}$ ) [62]. It is also important that fission chambers are operable in high gamma flux environments and due to the high neutron-to-gamma signal ratio, the large fission pulses permit discrimination against gamma pulses and pulse pile-up [63]. This means that fission chambers are almost insensitive to gammas depending on the mode of operation.

Fission chambers are essentially ionization chambers coated with a small thickness of fissile material ( $1.4 \text{ mg.cm}^{-2}$  in model used) along the wall. The chamber is typically filled with a noble gas such as argon. When voltage is applied between the outer and inner electrodes, a radially symmetrical electric field between the cathode and the anode of the chamber is created. The working principle of fission chamber detectors is as follows [64]:

- 1) Incident neutron is absorbed in the fissile nucleus and causes fission.

- 2) Fissile nucleus splits into two fission fragments which travel in opposite directions, causing at least one of the fragments to travel into the gaseous region of the detector.
- 3) The heavy fission fragments have a high linear energy transfer and will deposit most if not all of their energy in the fill gas by ionizing the gaseous atoms.
- 4) Due to the applied voltage, free electrons are collected on the inner anode wire, producing a current which is the output signal of the fission chamber.

Fission chambers are typically used in the core of nuclear reactors and outside the core for power calibration by estimating the thermal neutron flux. In a reactor, there are three main flux ranges depending on the power at which the reactor is operating at: startup range, intermediate range and power range. Each range has different thermal neutron fluxes [65]. To handle this wide measurement range with a single detector, fission chambers are commonly used because they are operable in pulse mode, current mode and Campbelling or Mean Squared Voltage (MSV) mode [59,62,65,66].

At low thermal neutron fluxes outside the core ( $<10^5$  n/cm<sup>2</sup>s), pulse mode can be used. At this range, the fission rate is so low that each electronic pulse induced by a nuclear fission can be counted event by event [62]. The event rate is related to the detector fission rate. Pulse mode can be used because the average delay between two pulses is much larger than the pulse duration [67].

At high thermal neutron fluxes ( $>10^7$  n/cm<sup>2</sup>s), the fission rate becomes very large. The neutron flux here is so large such that gamma ray induced current in the chambers are no longer significant [62]. Due to the high energy deposited by a neutron compared to a gamma interaction in the counting gas, the fission chamber is the only detector capable of using fluctuations to create a neutron proportional signal [68]. At this range, fission chambers operate in the current mode. Current from a random current pulse source is proportional to the average pulse rate and thus charge produced per event is proportional to the pulse height.

At intermediate thermal neutron fluxes, similar to the current mode, the pulses start overlapping and cannot be individually processed anymore [66,67]. In this region, the gamma-ray induced events are still significant compared to the neutron flux and therefore current mode poses a challenge to neutron detection because it comes with a significant gamma contribution and is not able to discriminate against gammas. Hence, simple current mode is not suitable for only neutron detection [62,66,67]. In order to account for gammas, a second chamber without fissile material deposit coupled to the first chamber can be used [62]. Another way to discriminate this is to operate the fission chambers in Campbell or MSV mode. The Campbell theorem states that the mean square voltage of the signal fluctuation is proportional to the neutron fluence rate. To obtain this proportionality the signal, therefore, has to be squared. Unlike pulses or currents which give the required value directly, the neutron fluence rate is obtained by calculation [68]. By squaring the signal, the difference in charge deposited by gammas

and neutrons becomes more apparent, making this detector viable for discrimination against gammas.

This work will use fission chamber detectors in pulse mode due to the relatively low thermal neutron fluxes and the need to discriminate gamma interactions from neutron interactions.

The internal RMS is designed to stay inside a dry cask for approximately 40 years. However, the gradual consumption of neutron-sensitive material over a long period of time is an issue. This phenomenon is known as burnup. Typically, fission chambers have a highly enriched uranium lining (>90%  $^{235}\text{U}$ ). During extended exposure to neutrons, the fissile  $^{235}\text{U}$  atoms deplete, which leads to decreased neutron sensitivity. A typical fission chamber becomes 10% less sensitive to neutrons after a fluence of  $1.4 \times 10^{14} \text{ n.cm}^{-2}$  [69,70]. A 50% decrease in relative sensitivity corresponds to an integrated neutron exposure of approximately  $1 \times 10^{21} \text{ n.cm}^{-2}$ . To give perspective to this number, an exposure of  $5 \times 10^{21} \text{ n.cm}^{-2}$  is equivalent to ten years of exposure at a flux level of  $1 \times 10^{13} \text{ n.cm}^{-2} \text{ s}$ . Hence, this is not an issue for SNF in dry casks as the flux seen by the detectors is through the MPC lid shielding is approximately  $6.82 \times 10^4 \text{ n.cm}^{-2} \text{ s}^{-1}$ . Of this, the thermal flux is  $1.45 \times 10^3 \text{ n.cm}^{-2} \text{ s}^{-1}$ .

Finally, in order to calculate the response of the fission chambers in count rate from MCNP, some calculations need to be done. The sensitivity of the fission chamber is a combination of two factors [71]:

- a) Fission product efficiency (FPE): probability that a neutron entering the detector causes a fission event to occur in the sensitive material (units are fissions. $s^{-1}$ per  $cm^{-2}s^{-1}$  or fps/nv).
- b) Probability of detection (PD): probability that a fission product from a fission event is ejected into the gas chamber with sufficient energy to be registered as a count (units are counts per fission or cps/fps).

The sensitivity,  $S$  of the fission chamber is then given by Equation 5-2 and has units of cps/nv.

$$S = FPE \times PD \quad \text{Eq. 5- 2}$$

The FPE and PD can be calculated in MCNP, however, this value is provided by the manufacturer to be 1 cps/n. $cm^{-2}.s^{-1}$  in the pulse mode [72]. The count rate (cps) registered in the detectors can be calculated by multiplying the source strength ( $n.s^{-1}$ ), thermal neutron flux in the detector from MCNP F4 tally outside the fissile region ( $n. cm^{-2}$ ) and sensitivity (cps/n. $cm^{-2}.s^{-1}$ ). Total counts are obtained by multiplying the count rate by the measurement time in seconds.

#### **5.6.1.2. Fission Chambers – Position and Number of Detectors**

The number of detectors were determined by considering not only the minimization of non-detection probabilities,  $\beta$ , but also robustness. In this scenario, since the RMS will stay in a dry cask for about 40 years, redundancy with the number of

detectors is necessary, in case one detector fails, there will be another that can provide signal.

MCNP simulations were performed using three fission chambers: one fission chamber in the center as shown in Figure 5-7, and two in the same configuration as shown before in Figure 5-5. To determine if one detector was sufficient to distinguish all diversion scenarios, the response from each detector was obtained individually using average cell flux tallies, F4, in MCNP. For each diversion scenario, the source strength was multiplied by the appropriate number of SNF assemblies present. Figure 5-8 shows the  $\beta$  probabilities (%) obtained for a single fission chamber detector in the center and two fission chamber detectors in the RMS configuration where  $D_L$ ,  $D_R$  and  $D_C$  refer to the left, right and center detectors. Their corresponding  $\beta$  probabilities are shown as  $\beta_L$ ,  $\beta_R$  and  $\beta_C$ .

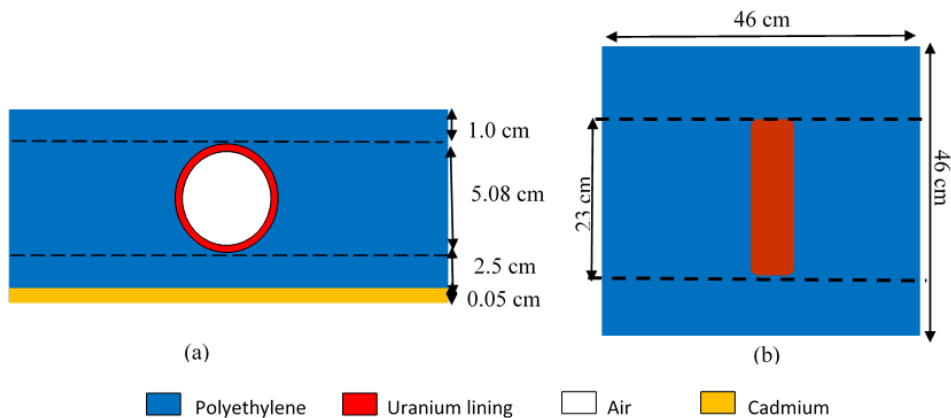


**Figure 5-7 Internal RMS with one fission chamber in the center**

Each simulation was performed separately. The measurement time was assumed to be 3 seconds. For all the cases, the false alarm probability,  $\alpha$  was set at 5%. The measurement time is determined by finding the time that corresponds to the first instance that all the  $\beta$  probabilities for all diversion scenarios is less than 20%.

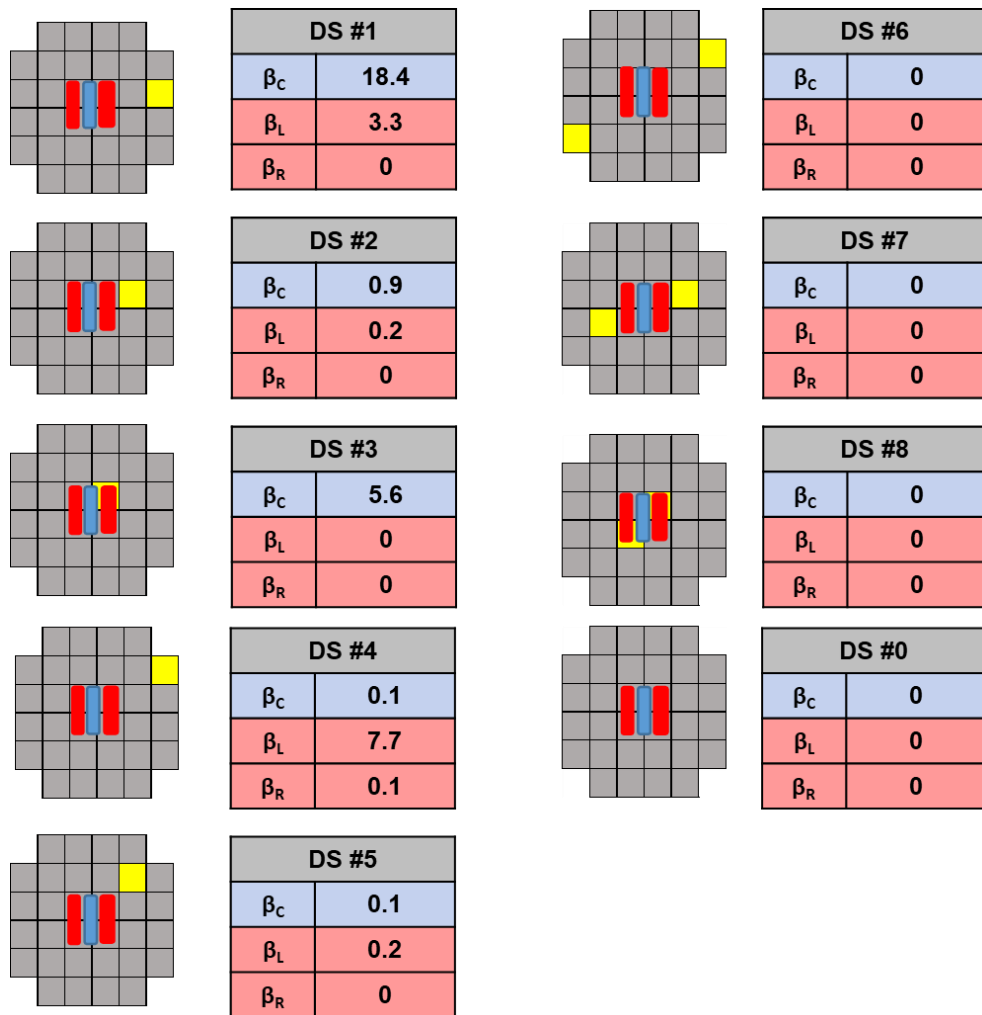


Figure 5-8  $\beta$  probabilities (%) for each fission chamber where  $D_C$  is the center detector in blue,  $D_L$  and  $D_R$  are the left and right detectors in red.  $\beta_C$ ,  $\beta_L$  and  $\beta_R$  are the corresponding  $\beta$  probabilities. The yellow square designates position of diverted assembly. All results are for 3 s measurement time and 5%  $\alpha$

From Figure 5-8, considering the output of each detector individually, the following observations are made:

1. All the diversion scenarios have  $\beta$  probabilities below the IAEA guidelines of 20% - Highest is 18.4% for DS1 for the central detector.
2.  $D_L$  and  $D_R$  have  $\beta$  probabilities less than 8% for all the diversion scenarios.
3. For all the single assembly diversion cases (DS 1-5), as the diversion occurs closer to the center of the cask where the detectors are located, detecting the diversion becomes easier due to the proximity to the detector and less self-shielding from surrounding assemblies – there will be a larger drop in flux as the diversions occur closer to the center for example from DS1 to DS2 to DS3 such that the neutron flux observed by the detectors correspondently becomes lower.
4. A detailed observation of the flux received by  $D_C$  reveals that it always receives fewer counts than the detectors in the left and right position with the exception of DS0 (open lid case), where  $D_C$  receives a higher flux than both the other detectors. These flux changes are summarized in Table 5-3.

**Table 5-3 Thermal neutron flux in  $D_C$ ,  $D_L$ , and  $D_R$  which are the center, left and right fission chamber detectors for all diversion scenarios (DS) and the percentage difference in thermal flux between  $D_C/D_L$ ,  $D_C/D_R$  and  $D_L/D_R$**

DS	Thermal neutron flux ( $n.cm^{-2}.s^{-1}$ )			% Difference		
	$D_C$	$D_L$	$D_R$	$D_C/D_L$	$D_C/D_R$	$D_L/D_R$
RS	1.05E+04	1.09E+04	1.09E+04	-3.40	-3.40	0.00
0	6.33E+03	6.23E+03	6.23E+03	2.93	2.93	0.00
1	1.03E+04	1.07E+04	1.06E+04	-3.95	-3.02	0.90
2	1.02E+04	1.06E+04	1.04E+04	-3.73	-2.26	1.41
3	1.02E+04	1.05E+04	1.04E+04	-2.06	-1.48	0.56
4	1.01E+04	1.07E+04	1.06E+04	-5.84	-4.64	1.14
5	1.00E+04	1.06E+04	1.05E+04	-5.83	-4.52	1.24
6	1.00E+04	1.04E+04	1.04E+04	-3.62	-3.62	0.00
7	9.72E+03	9.87E+03	9.89E+03	-1.56	-1.77	-0.20
8	9.55E+03	1.02E+04	1.02E+04	-6.81	-6.81	0.00

From Table 5-3, the thermal flux in  $D_C < D_R < D_L$ . Since the diversion scenarios are taking place on the right side of the cask,  $D_R$  records a larger reduction in thermal neutron flux than  $D_L$ . However, the difference in  $D_L$  and  $D_R$  is very small (<1.5% for all DS).  $D_C$  on the other hand, has fluxes between 1.5% and 7% less than the other detectors. A possible explanation for this drop in flux is that since  $D_C$  is centrally located, the neutrons that make it to the polyethylene box surrounding the detector are

thermalized more and are stopped in the polyethylene before reaching  $D_C$ . Since  $D_R$  and  $D_L$  are closer to the edges of the polyethylene box, they receive a higher flux as less thermalization and absorption happens prior to reaching the detectors. Thermal neutrons are necessary for detection, hence, a ‘sweet spot’ needs to be achieved such that the thickness of polyethylene is enough to thermalize the neutrons but not absorb them. This study shows that the position of the detector is important with regards to maintaining low  $\beta$  probabilities and receiving adequate counts for reliable counting statistics. In order to negate this effect, longer counting times (over 10 seconds) allows for all detectors to have low  $\beta$  probabilities of 0 for all diversion scenarios.

For the purpose of this work,  $D_R$  and  $D_L$  show very similar results for all the diversion scenarios and have the same trends for flux. These two detector positions are included in the final RMS design as they are reliable (even if one fails, the results from the other would be sufficient to determine if a SNF assembly diversion occurred).

Using  $D_R$  and  $D_L$ , DS1 and DS4 are the most challenging diversions to detect as they are the furthest away from the detectors. However, when the measurement time increased,  $\beta$  probabilities decreased for  $D_C$ ,  $D_R$  and  $D_L$ . i.e. for a 10-second measurement time,  $\beta$  is 0% for all DS in all detectors.

All of the two-assembly diversion scenarios (DS6 through DS8) and the open lid scenario (DS0) are always 100% detectable.

### 5.6.1.3. Polyethylene

For this work, all the polyethylene used is high density polyethylene (HDPE). Polyethylene is a neutron moderator that slows down high energy neutrons to thermal neutron energy ranges that can be detected by the fission chamber detectors. Polyethylene is made of carbon and hydrogen. Hydrogen works well as a neutron moderator because its mass is almost identical to that of a neutron. This means that one collision will significantly reduce the energy of the neutron according to the laws of conservation of energy and momentum [73]. Due to its high neutron scattering cross section, materials with high hydrogen content are frequently chosen as neutron moderators.

Using a moderator is essential as most of the neutrons born from SNF are in the fast range as they originate from spontaneous fission and ( $\alpha$ , n) reactions. From Table 5-1, the fraction of thermal neutrons entering the cavity where the internal RMS is placed is ~2% of the total incoming flux. In order to increase the fraction of thermal neutrons and improve detection efficiency, the fission chamber detectors are surrounded with polyethylene. The amount of polyethylene surrounding the RMS was optimized by Khudoleeva et al. [53] Figure 5-5 shows the thicknesses of polyethylene surrounding the detectors. However, the design was changed to increase the sensitivity of the detectors to the various diversion scenarios. In the model proposed by Khudoleeva et al., there was 2.5 cm of polyethylene underneath the cadmium sheet as shown in Figure 5-9. In the model used for the internal RMS in this work, cadmium is placed at the bottom of the

polyethylene as opposed to being under the detectors. Better  $\beta$  probabilities have been obtained due to this change.



**Figure 5-9 Internal RMS configuration from Khudoleeva et al.**

#### **5.6.1.4. Cadmium**

Cadmium is widely used in the nuclear field, as it is a strong thermal neutron absorber. In natural cadmium, 12.2% is made up of  $^{113}\text{Cd}$ . At a neutron velocity of  $2200 \text{ m}\cdot\text{s}^{-1}$ , the absorption cross section of  $^{113}\text{Cd}$  is  $\sim 20,000$  barns [74]. The cadmium cut off energy is  $\sim 0.5 \text{ eV}$  [75]. Employing this cadmium cut off energy, a thin layer of cadmium was placed between the MPC lid and the polyethylene box (refer to Figure 5-5). While it may seem counter intuitive to place a thermal neutron absorber close to the detectors, cadmium serves to suppress the thermal flux from the central assemblies under the RMS while increasing the sensitivity of the RMS to peripheral assemblies since they are already at a disadvantage of distance and detector solid angle.

The thickness of the cadmium sheet was determined to be  $0.05 \text{ cm}$  from previous work by Khudoleeva et al., [76]. However, the size (width x length) of the sheet was not optimized, rather chosen to match the size of the polyethylene box. To optimize the size,

a series of MCNP simulations were performed where the size of the cadmium sheet was varied in increments of 11.2 cm, which corresponded to half an assembly width until the maximum physical allowable size of 135.6 cm x 135.6 cm. Since the dry casks is symmetric due to uniform loading patterns, the cadmium sheet was designed as a perfect square and both the x and y lengths were altered at the same time. In order to determine which dimensions were optimal for the RMS, the FMESH tally coupled with average cell flux, the F4 tally was used to provide thermal neutron flux maps for each simulated case. The ratio of the thermal neutron flux at the cask edge to the cask center above the cadmium sheet were calculated. A flux map example for one of the cadmium sizes is shown in Figure 5-10. The thermal neutron flux drops in the center due to the presence of cadmium. A high ratio of corner to center indicates that the flux under the detectors have been suppressed and the corner SNF assembly diversions can be more easily detected.

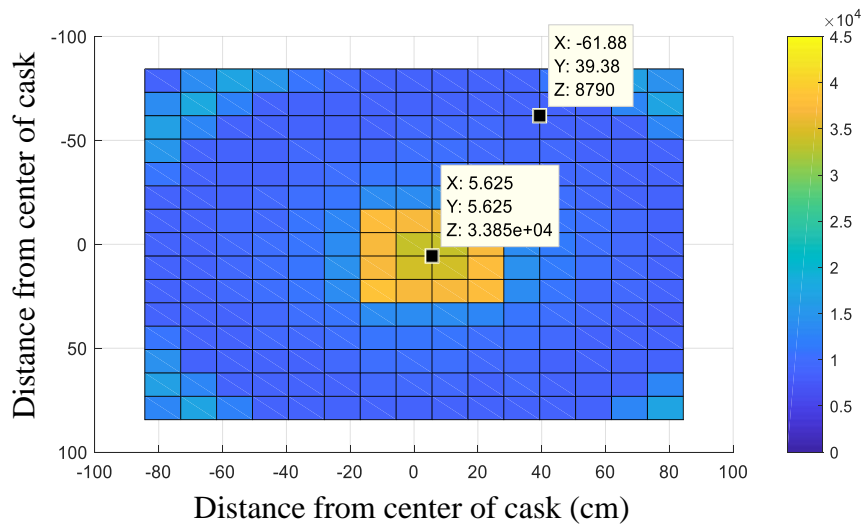


**Figure 5-10 Mesh tally indicating the thermal neutron flux above cadmium and in the corner. Reprinted from 43.**

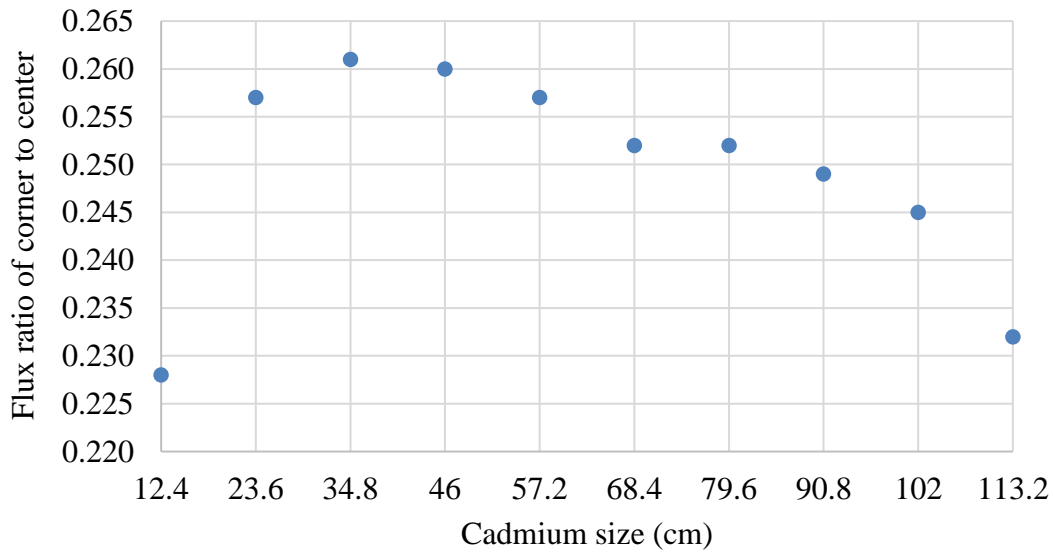


**Figure 5-11 Flux ratio versus cadmium size**

Figure 5-11 shows the size of the cadmium sheet for a thickness of 0.05 cm and the corresponding corner to center flux ratios. The cadmium size in Figure 5-11 corresponds to length. From these neutron flux ratios in Figure 5-11, the 34.8 cm x 34.8 cm dimension contributed to the largest ratio, after which, increasing the cadmium dimensions only provided diminishing returns. The 46 cm x 46 cm cadmium dimension was also tested as the difference in flux ratio between this dimension and the former was less than 0.4%. Using these cadmium dimensions, SNF assembly diversion scenarios were simulated using MCNP6 and the corresponding  $\beta$  probabilities were calculated (refer to Figure 4-1 for diversion scenario locations). The  $\beta$  probabilities for three dimensions: 34.8 cm x 34.8 cm, 46 cm x 46 cm and 135.6 cm x 135.6 cm (largest size) are shown in Table 5-3. The largest cadmium size of 135.6 cm x 135.6 cm is shown to

prove that cadmium aids in making the detector array more sensitive to the periphery, however, adding too much cadmium can be detrimental to the system.

In order to verify that cadmium does indeed help in sensitizing the detector array to the peripheral assembly diversions, all diversion scenarios were performed for the internal RMS without cadmium as a benchmark comparison. The results are shown in Table 5-4 as the '0' cadmium size. Focusing on this case, in the right detector, DS1, DS4 and DS5 have  $\beta$  probabilities over 20% for a 2 second measurement time. However, adding cadmium to the system significantly reduces the  $\beta$  probabilities in all cases. This is evident in both the 34.8 cm x 34.8 cm, 46 cm x 46 cm sizes. DS1, DS4 and DS5 are assembly diversions that take place in the corners and are farther away from the detectors unlike DS2 and DS3. Thus, showing a drop in  $\beta$  probabilities for these cases indicate that diversions of peripheral assemblies will be indicated in the RMS. However, in the 135.6 cm x 135.6 cm size,  $\beta$  probabilities of the left detector is much higher for DS1, DS4 and DS6 (compared to the smaller cadmium sizes and 0 cadmium). Adding more cadmium than necessary to the system negates the ability of the detectors to identify potential diversions in peripheral assemblies.

**Table 5-4  $\beta$  probabilities (%) for all diversion scenarios for different cadmium sizes using a 2-second measurement time and 5%  $\alpha$**

	Cd size (cm)	DS1	DS2	DS3	DS4	DS5	DS6	DS7	DS8	DS0
Left Detector	0	1	0	0	2	0	0	0	0	0
	34.8 x 34.8	8	0	0	14	2	0	0	0	0
	46 x 46	2	0	0	3	1	0	0	0	0
	135.6 x 135.6	14	0	0	26	3	19	0	0	0
Right Detector	0	53	11	1	66	31	1	0	0	0
	34.8 x 34.8	1	0	0	1	0	0	0	0	0
	46 x 46	0	0	0	0	0	0	0	0	0
	135.6 x 135.6	0	0	0	0	0	0	0	0	0

The optimal dimension of cadmium was chosen to be 46 cm x 46cm as it provided lowest  $\beta$  probabilities for both detectors. DS1 and DS4 are the most challenging cases to detect as they are in the far corners away from the detectors. It is seen that by using 46 cm x 46 cm of cadmium, the  $\beta$  probabilities 0 for all DS in the right detector and are under 3% in the left detector. The 34.8 cm x 34.8 cm size had higher  $\beta$  probabilities for DS1 and DS4 in the left detector. Hence, this proves that a cadmium size of 46 cm x 46 cm is suitable and has been optimized for the internal RMS.

## 5.7. External RMS

The second approach to this work involves a whole new type of RMS that uses an array of micro-structured semiconductor neutron detectors (MSNDs). The MSNDs represent a compact, low-cost, high efficiency means of solid-state thermal neutron detection. These detectors claim to have thermal neutron efficiencies as high as 30% for single sided and over 65% for double sided configurations [77]. To provide a comparison, fission chambers generally have an intrinsic efficiency of 0.5 - 1% [78]. Employing this feature of MSNDs, a set of MCNP6 simulations were performed to find the optimal configuration of these detectors that can be placed on top of the lid of a dry cask to detect any diversion of SNF assemblies from the cask. The working principle of these detectors relies on the  ${}^6\text{Li} (n,t) {}^4\text{He}$  reaction which is shown in Equation 5-3 [79].



The detector consists of a Si diode with etched channels backfilled with nano-sized  ${}^6\text{LiF}$  powder [80]. Hence the absorption of a neutron creates a 2.7276 MeV triton and a 2.0533 MeV alpha particle. The charged particle progenies from the neutron interaction are ejected in opposite directions and are easy to detect due to their high energy, and charge to mass ratio.  ${}^6\text{Li}$  has a large microscopic thermal neutron absorption cross section of 940 barns hence aiding with the high efficiency [81]. The crystalline density of  ${}^6\text{LiF}$  is  $2.55 \text{ g.cm}^{-3}$  while the overall density achieved for the final MSND was  $0.892 \text{ g.cm}^{-3}$  with a  ${}^6\text{LiF}$  packing fraction of 35% [80].

When using MSNDs in a RMS, Domino® neutron detectors D411S-30-D25-V5.4 from Radiation Detection Technologies Inc. were chosen. Each detector has an active area of  $4.0 \text{ cm}^2$  and can be stacked to form larger arrays depending on the goal [77].

For the purpose of this work, modelling of MSNDs was not done, void cells with realistic dimensions were used to represent the detectors in the RMS model. Each detector is fabricated as 0.05 cm thick with an active area of dimensions 2 cm x 2 cm [77] hence the model had the same dimensions.

From the specification sheet provided by the company [82], the neutron sensitivity of a single detector is  $1.2 \text{ cps/nv} \pm 0.04 \text{ cps/nv}$  where cps is counts per second and nv is the flux in  $\text{cm}^{-2} \cdot \text{s}^{-1}$ . It has a thermal neutron efficiency of 30% when measured with an ANSI moderated  $^{252}\text{Cf}$  source at 0.25 m distance. Stacking this detector with another one such that there are two detectors side by side increases the neutron sensitivity linearly, making it  $2.4 \text{ cps/nv} \pm 0.08 \text{ cps/nv}$  for the stacked configuration. Hence, MSNDs are extremely sensitive to thermal neutrons and would be excellent candidates for the external RMS. In addition, the gamma rejection rate for a single detector is  $<1 \text{ cpm}$  at  $50 \text{ mR} \cdot \text{h}^{-1}$  with a  $^{137}\text{Cs}$  source [82].

The final design of the external RMS comprised of eight MSNDs in a 4 x 2 array. It has a total active area of  $8 \text{ cm} \times 4 \text{ cm} = 32 \text{ cm}^2$ . This array of detectors is encased in polyethylene moderation with 1.5 cm thick polyethylene under the detectors and 2.5 cm thick polyethylene above the detectors as shown in Figure 5-12. Polyethylene serves as a

medium to thermalize neutrons that are in the intermediate and fast range that exit the dry cask as well as reflect the scattered neutrons back into the system. Figure 5-12 shows a rendering of the external RMS with the active volume of the detectors modelled, enveloped in polyethylene and their corresponding dimensions. The corresponding sensitivity for eight detectors is  $9.6 \pm 0.32$  cps/nv.

The external RMS is placed on the top of the dry cask lid at its center to be equally sensitive in all radial directions. In order to optimize the thickness of polyethylene and the number and position of MSNDs in the external RMS, MCNP simulations were performed. The following subsections explain how the final external RMS design was devised.

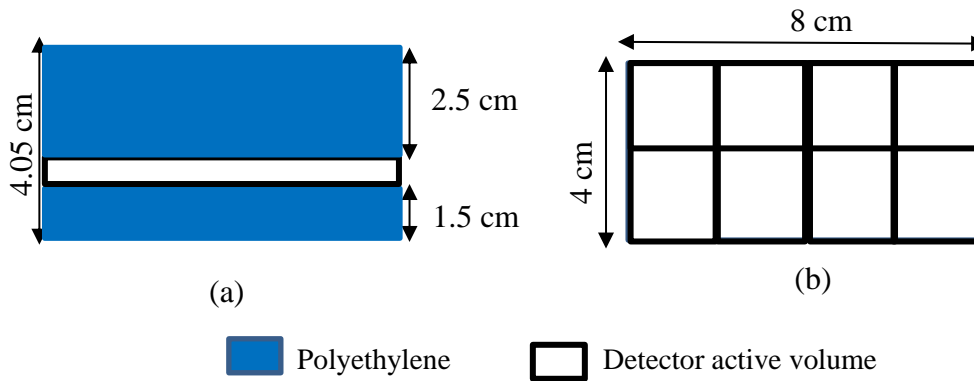


**Figure 5-12 External RMS with MSND detectors shown in (a) front view and (b) top view**

### 5.7.1. Polyethylene Optimization

The thermal neutron flux exiting the cask is  $\sim 17.1 \text{ n.cm}^{-2}.\text{s}^{-1}$  when it was fully loaded with 32 SNF assemblies. This was obtained from a MCNP simulation using average cell flux tally, F4 in a 0.05 cm thick cylindrical cell (with the same radius of the cask) above the lid of the dry cask. To increase the fraction of thermal neutrons, avoid long measurement times, and improve detection efficiency, MSNDs were placed inside a polyethylene box. Polyethylene will provide moderation for intermediate/ fast energy neutrons and slow them down to thermal energy ranges such that they are detectable by the MSND array.

Initially, the number and position of MSNDs used was still unknown. First, to determine the amount of polyethylene needed, an array of MCNP simulations were performed. From Figure 5-12 (a), it is shown that there are two dimensions of polyethylene that need to be optimized: bottom (under the detector cells) and top (above the detector cells).

In the first simulation, the entire lid of the dry cask was covered with varying thicknesses of polyethylene to obtain the ‘best case scenario’ (in reality, the whole lid will not be used, rather an optimized area will be determined). The neutron flux above that layer of polyethylene was measured using a F4 tally in MCNP simulations, which calculated the average flux in a cell. The cell was defined to be 0.05 cm thick to correspond to the thickness of the MSND and had a radius of 166.52 cm to correspond radius of the lid. Additional thicknesses of polyethylene were added on top of the tally

cell to increase reflections of thermal neutrons. The energy group structure used to bin the tallies is shown in Table 5-5.

Simulation were performed for the bottom polyethylene thickness of 0 to 2.0 cm in steps of 0.5 cm while the top polyethylene varied from 0 to 3.0 cm in steps of 0.5 cm and a 1cm step between 3.0 cm and 4.0 cm thickness.

The energies of interest from the group structure shown are the thermal neutrons below 0.025 eV. Figure 5-13 shows the thermal neutron flux as a function of polyethylene thicknesses below and above the detector cells. The x-axis shows the thickness of polyethylene above the detector cells while various lines correspond to the thickness of polyethylene below the detector (between the detectors and the cask lid).

Focusing on just the polyethylene thickness below the detectors, there is a large jump (38.6%) in thermal neutron flux from 0 to 0.5cm of polyethylene indicating tremendous increase in the thermal neutron flux seen by the detectors. Closer observation shows that for the 0.5 cm, 1 cm, 1.5 cm, and 2 cm thicknesses, the 1.5 cm and 2 cm thicknesses provide the highest neutron flux regardless of the thickness of polyethylene above the detectors. It was seen that between the 1.5 cm and 2 cm of polyethylene below the detectors, there was a drop in thermal flux of ~1%. Thus, 1.5cm of polyethylene was the point before diminishing returns in thermal neutron flux for additional thickness. As the thickness of polyethylene is increased, no additional increase in thermal flux is observed because neutrons are being absorbed by polyethylene.

The same methodology is used for the amount of polyethylene above the detectors. It is seen that the trends are continually increasing thermal flux with increasing polyethylene thickness. The point of diminishing returns occurs at 2.5 cm of polyethylene behind the detectors as any further increase constituted only ~ 1% increase in thermal neutron flux. The neutron flux recorded in the thermal (0-0.025 eV), cadmium cut off (0.025 eV- 0.5 eV) intermediate (0.5eV to 1 keV) and fast (1 keV – 20 MeV) neutron energy ranges for various configurations of polyethylene are shown in Appendix D.

The final design used 1.5 cm and 2.5 cm thicknesses of polyethylene below and above the detector cells respectively.

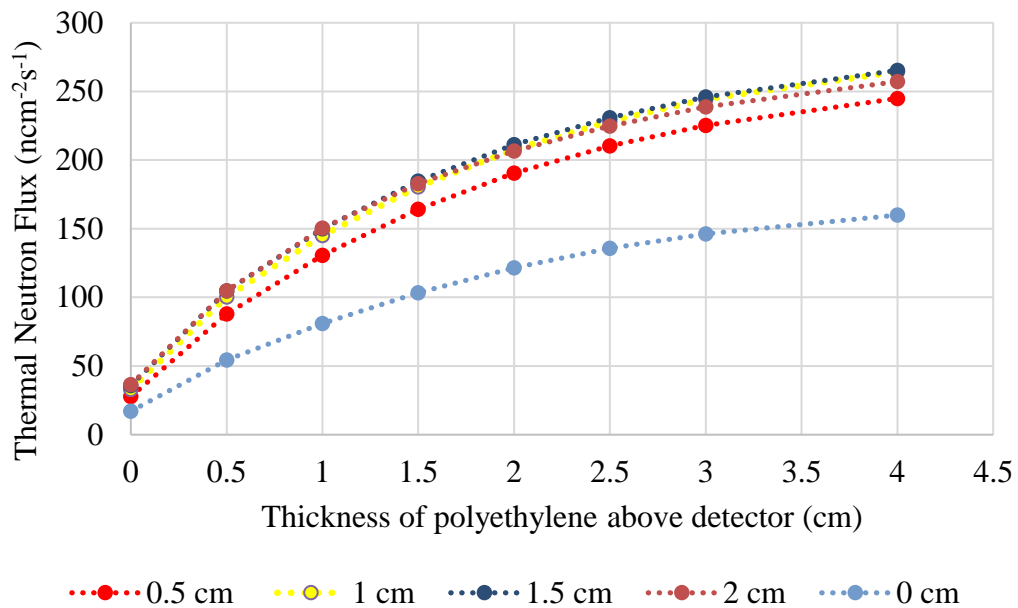


**Figure 5-13 Thermal neutron flux as a function of polyethylene thicknesses above the detector cells and the lines represent the variation of polyethylene thicknesses below the detector cells.**

### 5.7.2. Number of Detectors/Array Size

An array of detector configurations using MSNDs were studied to optimize non-detection probabilities ( $\beta$ ) for various SNF assembly diversion scenarios. The configurations are shown in Figure 5-14 where the thickness of each detector is 0.05 cm and the area was 2 cm x 2 cm. For each configuration, there were different dimensions tested. All the configurations, dimensions and number of detectors used are shown in Table 5-5. While the cask's concrete lid has a radius of 166.52 cm, the SNF assemblies inside are contained by the MPC which has a radius of 84.46 cm. Hence, aside from the Full lid case, all the other cases (Line and Plus; see Figure 5-14) had maximum dimensions that corresponded to the radius of the MPC.

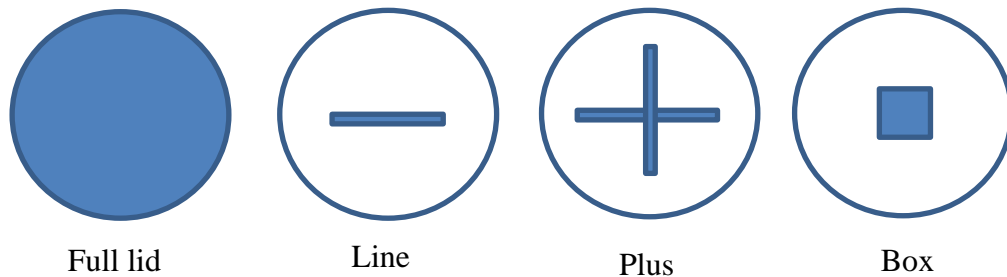


**Figure 5-14 MSND array configurations on the lid of the dry cask where the blue cells represent the position of the detector in different configurations on the lid (circle)**

**Table 5-5 Configurations, dimensions and number of detectors used for each MCNP simulation performed where R is radius, L is length, W is width, x is the horizontal plane and y is the vertical plane**

<b>Configuration</b>	<b>Name</b>	<b>Dimensions (cm)</b>	<b>Number of detectors</b>
Full Lid		R: 166.52	~21778
Line	Single	L: 168	168
		W: 2	
	Double	L: 168	336
		W: 4	
Plus	Single	L: 168 (x) + 164 (y)	332
		W: 2	
	Double	L: 168 (x) + 164 (y)	664
		W: 4	
Box	2 x 2	L: 4	4
		W:4	
	3 x 3	L: 6	9
		W:6	
	4 x 4	L:8	16
		W:8	
	4 x 2	L:8	8
		W:4	

In the *Full lid* configuration, the entire dry cask lid was assumed to be filled with detectors. This is an improbable case as this would require ~ 21778 detectors to be linked together to provide the neutron signal. It is simulated to show an ideal scenario.

The *Line* configuration is simulated in two ways: single and double. In the single configuration, the line is 168 cm long and 2 cm wide such that it hosts 168 MSNDs. In the double configuration, the width of the line is doubled such that two single lines stacked next to each other. The width is now 4 cm while the length remains 168 cm. In this double configuration, 336 MSNDs are used.

The *Plus* configuration is also setup similarly to the *Line* where there are single and double widths. The length of the *Plus* configuration is broken up into two parts: horizontal (x) and vertical (y). In the horizontal position, the flat part of the *Plus* is 168 cm long and 2 cm wide in single and 4cm wide in double. In the vertical position, the box is 164 cm in length and 2 cm wide in single and 4cm wide in double.

The previous configurations are test cases to see if a spread in the horizontal and vertical axes are necessary to detect a diversion. The *Box* configuration is a rectangle in the center of the cask's lid. Four dimensions are simulated to determine if a rectangle with fewer detectors can perform better than the other configurations and decide if position sensitivity is crucial.

For all the configurations, there is 1.5 cm of polyethylene below the detectors and 2.5 cm above replicating the dimensions of the respective configuration. All diversion scenarios were simulated for each of the cases to determine the best external RMS configuration. The results from this study is shown in Table 5-6.

It is important to note that the sensitivity of a single MSND is 1.2 cps/nv  $\pm$  0.04 cps/nv. For each of the configurations shown in Table 5-5, the  $\beta$  probabilities were calculated using the mentioned sensitivities multiplied by the number of detectors present. Error propagation was performed using Equation 5-4.

$$\sigma_{total} = \sqrt{\sigma_{MCNP}^2 + \sigma_{detectors}^2 + \sigma_{Sensitivity}^2} \quad \text{Eq.5- 4}$$

where:

- $\sigma_{total}$  = Total uncertainty
- $\sigma_{MCNP}$  = Stochastic uncertainties in MCNP tallies
- $\sigma_{detectors}$  = Uncertainties in detector measurements =  $\sqrt{v}$ counts
- $\sigma_{sensitivity}$  = Uncertainties in detector sensitivity

All the results of the non-detection probabilities ( $\beta$ ) presented in Table 5-6 are for a measurement time of 5 seconds; increasing the measurement time will decrease the  $\beta$  probabilities, hence achieving better results. The measurement time of 5 seconds was chosen to decrease most of the  $\beta$  probabilities to less than 20%. It is seen that the *Full Lid* configuration provides excellent results and every single diversion scenario is 100% detectable. Since the whole lid is covered with detectors, this is expected. Even if the measurement time was 1 second, the same results are expected.

**Table 5-6  $\beta$  probabilities (%) for all configurations and all SNF diversion scenarios (DS) studied using a 5% false alarm probability ( $\alpha$ ) and 5-second counting time. Red numbers represent  $\beta$  probabilities over 20%**

Configuration	Name	$\beta$ probabilities (%)								
		DS0	DS1	DS2	DS3	DS4	DS5	DS6	DS7	DS8
Full Lid	-	0	0	0	0	0	0	0	0	0
Line	Single	0	0	0	0	0	0	0	22	0
	Double	0	73	0	0	0	0	0	0	0
Plus	Single	0	0	0	16	0	0	0	0	0
	Double	0	0	11	0	0	60	0	0	0
Box	2 x 2	0	13	3	1	21	7	1	0	0
	3 x 3	0	1	0	0	3	0	0	0	0
	4 x 4	0	0	0	0	0	0	0	0	0
	4 x 2	0	1	0	0	3	0	0	0	0

It is important to reiterate that one SQ of plutonium can be obtained from a diversion of two SNF assemblies. Hence, the goal of this work is to be able to detect with certainty even a single assembly diversion that has been substituted with a dummy assembly. Using that standard, any two assembly diversion scenarios (DS6 through DS8) with a  $\beta$  probability of more than 20% was immediately deemed not useful. Hence, from Table 5-6, the *Single Line*, was not useful as it had  $\beta$  probabilities over 20% for DS7.

Next, the *Double Line* and *Plus* configurations also showed relatively good results for a 5-second measurement time. In the *Double Line* configuration, all the  $\beta$  probabilities are 0% for all the diversion scenarios except DS1. It would take 30 seconds of measurement time to bring the  $\beta$  probability of DS1 to 19%. This is relatively long as there were other configurations that provided better results for a shorter measurement time. Since the *Double Line* configuration only looks at the horizontal spread, it becomes challenging to detect diversions happening in the periphery and corners.

Following that, it seems apparent that the *Plus* configuration would yield better  $\beta$  probabilities than the *Line* configuration due to a wider spread vertically in addition to the existing horizontal spread. Adding an entire row of detectors to the *Line* configuration to make it into a *Plus* should in theory show better results. This is true for some cases but false for others. For DS1 through DS5, all results are comparable between the *Single Line* and *Single Plus* except for DS3. The  $\beta$  probability of this case is 16% for the *Single Plus*. The combined output of all the detectors in the *Plus* configuration makes it less sensitive to the diversions happening in the center of the cask. For instance, the Double Plus detectors have higher  $\beta$  probabilities moving from

DS1 to DS2 and DS4 to DS5. This further illustrates that the widespread of the horizontal and vertical detectors enables better peripheral detection but reduce sensitivity to the center.

Finally, the *Box* configurations are of interest because they provide sufficiently low  $\beta$  probabilities with a fraction of the number of detectors required for the *Line* and *Plus* configurations. This is excellent as it decreases the cost of acquiring these MSNDs. Also, it will require less maintenance because checking tens of detectors for functionality is easier, cheaper, and faster than checking hundreds of detectors (used in other configurations).

The *Box* configuration is a rectangle with 4, 8, 9 or 16 detectors depending on the configuration. They will be placed in the center of the cask lid surrounded by polyethylene above and below. Starting with the *2x2 Box* configuration, it requires 4 detectors and has an active area of 16 cm<sup>2</sup>, which is 0.02% of total surface area of the dry cask lid. From Table 5-6, this configuration performs the worst of all the *Box* configurations. This is because of its very small size and short measurement time.

The *3x3 Box*, *4x4 Box* and *4x2 Box* all perform better than the *2x2 Box* for a 5-second measurement. All  $\beta$  probabilities for all the SNF assembly diversion scenarios are under 4%. Any one of these configurations would be a great choice. The conclusion was to choose the *4x2 Box* as it presented the same or better  $\beta$  probabilities as the other *Box* configurations and required the fewest number of detectors for the same measurement time.

## 6. ANALYSIS OF DIVERSION SCENARIOS USING BOTH RMS DESIGNS

In chapter 4, the SNF assembly diversion scenarios studied in this work as well as the methodology of calculating the false alarm probability ( $\alpha$ ) and non-detection probability ( $\beta$ ) were explained. Here, the results of the various SNF assembly diversion scenarios studied are presented for both internal (fission chamber configuration) and external (MSND configuration) RMS designs.

The count rate (cps) registered in the detectors can be calculated by multiplying the source strength ( $n.s^{-1}$ ), thermal neutron flux in the detector from MCNP cell average flux, F4 tally in the gas ( $n.cm^{-2}$ ) and sensitivity ( $cps/n.cm^{-2}.s^{-1}$ ). Total counts are obtained by multiplying the count rate by the measurement time in seconds.

For all the diversion scenarios (DS) studied, the activity corrected source strengths are listed in Table 6-1. In a complete scenario (or reference simulation, RS), there are 32 SNF assemblies where each assembly neutron source strength is  $4.74E+08$   $n.s^{-1}$ .

**Table 6-1 Total source strength of SNF for all diversion scenarios**

<b>Diversion Scenario</b>	<b>Number of assemblies</b>	<b>Source Strength (n.s<sup>-1</sup>)</b>
RS	32	1.52E+10
0	32	1.52E+10
1 to 5	31	1.47E+10
6 to 8	30	1.42E+10

In order to calculate  $\beta$  probabilities for the various diversion scenarios, the first step was to quantify the thermal neutron flux contributions of each assembly. Figure 6-1 shows the assembly number from 1 to 32, detailing each assembly location. In a homogenous fuel case, each SNF assembly had the same neutron emission rate of  $4.74E+08 \text{ ns}^{-1}$ . Hence, in this case, the relative contributions are dependent on location of the assembly and proximity to the RMS.

	<b>29</b>	<b>30</b>	<b>31</b>	<b>32</b>	
<b>23</b>	<b>24</b>	<b>25</b>	<b>26</b>	<b>27</b>	<b>28</b>
<b>17</b>	<b>18</b>	<b>19</b>	<b>20</b>	<b>21</b>	<b>22</b>
<b>11</b>	<b>12</b>	<b>13</b>	<b>14</b>	<b>15</b>	<b>16</b>
<b>5</b>	<b>6</b>	<b>7</b>	<b>8</b>	<b>9</b>	<b>10</b>
	<b>1</b>	<b>2</b>	<b>3</b>	<b>4</b>	

**Figure 6-1 Assembly numbers in a dry cask containing 32 SNF assemblies**

### 6.1. Internal RMS Homogenous Assembly Contributions

When the fuel is homogenous, there is a strong symmetry in the contributions of the fuel assemblies to the left and right detectors respectively. Figure 6-2 shows percentage contribution of each assembly to the left and right detectors within the internal RMS. These results were obtained from average cell flux, F4 tallies in MCNP. The grey boxes represent assemblies that contribute less than 3% to the signal seen by the detector while the white boxes represent assemblies that contribute more than 3%.

Generally, the peripheral assemblies contribute less than 3% each to thermal neutron flux seen by the detectors while the central assemblies contribute 4-5% each. In the left detector, the rightmost assemblies (10, 16, 22 and 28) contribute approximately 2% to the signal seen by the detector. This is the smallest contribution within the pattern. The same is seen for the right detector for the left most assemblies (5, 11, 17 and 23).

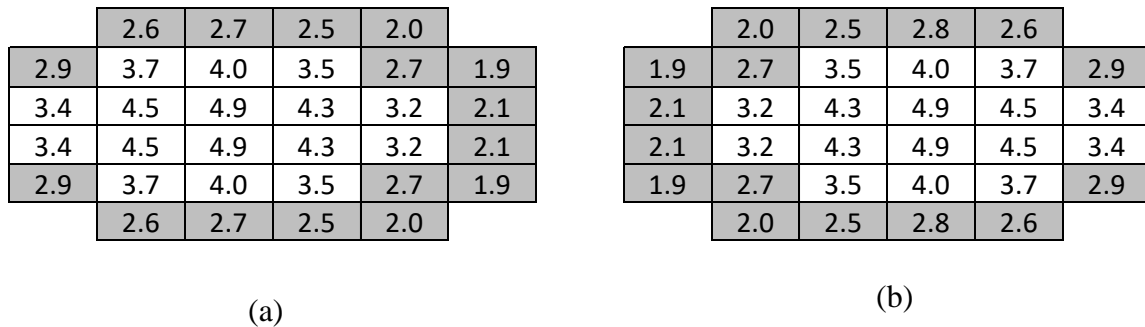


**Figure 6-2 Thermal neutron flux contributions (%) from each assembly to the (a) left and (b) right detectors within the internal RMS**

## 6.2. Internal RMS and Diversion Scenarios

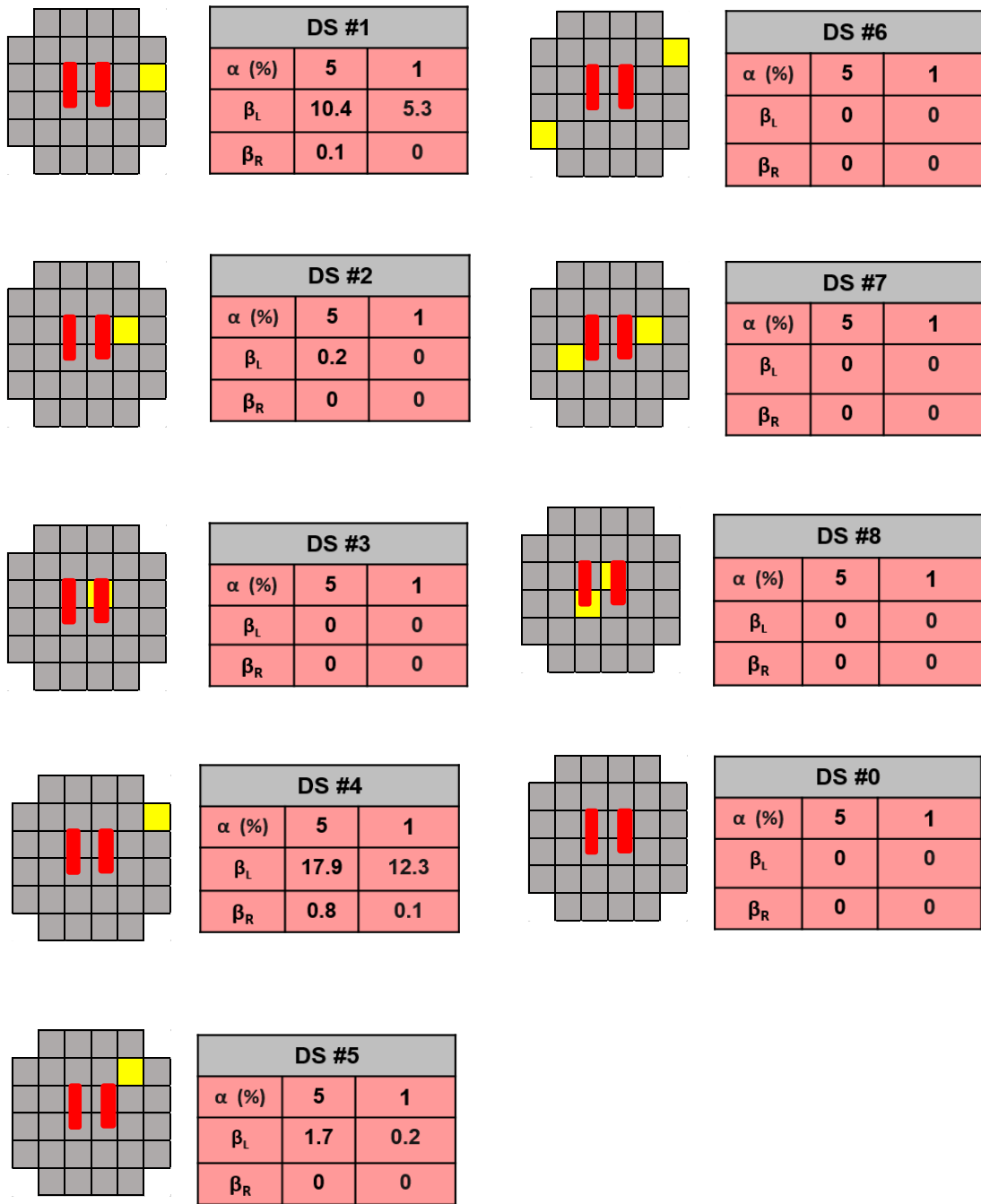
Figure 6-3 shows the  $\beta$  probabilities (%) for each fission chamber where  $D_L$  and  $D_R$  are the left and right detectors in red.  $\beta_L$  and  $\beta_R$  are the corresponding  $\beta$  probabilities. The yellow square designates position of diverted assemblies that have been replaced and  $\alpha$  is the false alarm probability (%). Depending on the need of the system,  $\alpha$  can be set to any threshold (1%, 5%, etc.). However, it should be noted that the lower the  $\alpha$  probability is set, the larger the non-detection,  $\beta$  probability becomes.

Figure 6-3 shows the  $\beta$  probabilities for all the diversion scenarios at two different  $\alpha$  thresholds: 5% and 1%. It is seen that for a measurement time of 2 seconds, for the 5% threshold, all the  $\beta$  probabilities are under 18% which is below the required 20% by the IAEA. Increasing the measurement time to 3 seconds drops all  $\beta$  probabilities below 8%. Also shown are  $\beta$  probabilities for a 1%  $\alpha$  threshold for a 4 second measurement time. All corresponding  $\beta$  probabilities are below 12% in all diversion scenarios at a 1%  $\alpha$  threshold.

For both thresholds, the highest  $\beta$  probabilities occur for DS1 and DS4 as they are the furthest measurements from the detector array in the center.

The results also indicate that the right detector has lower  $\beta$  probabilities for all diversion scenarios compared to the left. Since the diversions are taking place on the right side of the cask, the right detector has an advantage of proximity, thus identifies the diversions more easily than the left detector.

As the diversions happen closer to the center of the cask where the detectors are positioned, the  $\beta$  probability decreases significantly as it become easier to detect the diversion (and substitution) of the assemblies. Also, the two assembly diversion scenarios, DS6 – DS8 and the open lid scenario, DS0 are 100% detectable at 5% and 1%  $\alpha$  threshold using a 2-second measurement time. Finally, in order to obtain  $\beta$  probabilities below 20% when the  $\alpha$  threshold is reduced from 5% to 1%, the measurement time needs to be increased from 2 seconds to 4 seconds. If the measurement time of 2 seconds was used for a 1%  $\alpha$  threshold, the  $\beta$  probabilities for DS1 and DS4 in the  $D_L$  would be more than 20%.



**Figure 6-3  $\beta$  probabilities (%) for each detector and all diversion scenarios at 5%  $\alpha$  threshold using a 2-second measurement time and 1%  $\alpha$  threshold using a 4-second measurement time**

### 6.3. External RMS Homogenous Assembly Contributions

Assembly contributions (%) to the external RMS are shown in Figure 6-4. The grey boxes represent assemblies that contribute less than 3% to the signal seen by the detector while the white boxes represent assemblies that contribute more than 3%. When the fuel is homogenous, it is seen that the external RMS relies on the contributions of the central assemblies where each assembly contributes 3.1 – 4.4% to the total thermal neutron flux observed by the detectors. The peripheral assemblies contribute less than 3%. Since the peripheral assemblies share a smaller solid angle due to proximity to the center of the cask (where the detectors are), their contributions are significantly lower.

	2.4	2.7	2.7	2.4	
2.4	3.2	3.7	3.7	3.2	2.4
2.7	3.8	4.5	4.4	3.8	2.7
2.8	3.8	4.4	4.5	3.8	2.8
2.4	3.2	3.7	3.7	3.2	2.4
	2.4	2.7	2.7	2.4	

**Figure 6-4 Thermal neutron flux contributions (%) from each assembly to the external RMS**

### 6.4. External RMS and Diversion Scenarios

Figure 6-5 shows the  $\beta$  probabilities (%) for each diversion scenario with the external RMS. The blue box in the center represents the position of the external RMS detector. The yellow square designates position of diverted SNF assemblies that have

been replaced with a dummy assembly and  $\alpha$  is the false alarm probability (%). Depending on the need of the system,  $\alpha$  can be set to a different threshold. To demonstrate the robustness of this system,  $\beta$  probabilities for all diversion scenarios are calculated for 5%  $\alpha$  and 1%  $\alpha$  thresholds. The measurement time is determined by finding the time that corresponds to the first instance that all the  $\beta$  probabilities for all SNF assembly diversion scenarios is less than 20%.

In general, the external RMS takes a longer measurement time than the internal RMS to provide similar statistical results (5 seconds vs 2 seconds). The longer measurement time is needed due to the attenuation of neutrons in the concrete and stainless-steel lid. The shielding in the lid decreases the thermal neutron flux observed by the external RMS by two orders of magnitude (refer to Tables 5-1 and Table 5-2). Thus, a longer measurement time is needed to compensate for the decrease in flux and ensure the detector records sufficient counts for good counting statistics even with a high sensitivity of the MSNDs in the external RMS compared to the fission chambers in the internal RMS.

From Figure 6-5, it is seen that for a measurement time of 5 seconds with 5%  $\alpha$  threshold, all the  $\beta$  probabilities are less than 16%. Increasing the measurement time to 7 seconds reduces all  $\beta$  probabilities to 10% or lower. For the 1%  $\alpha$  threshold, the measurement time is increased to 9 seconds for corresponding  $\beta$  probabilities below 20%.

Like the internal RMS, the highest  $\beta$  probabilities occur for DS1 and DS4 as they are the furthest measurements from the detector array in the center. Since all the

assemblies are homogenized, this behavior is expected. Chapter 7 discusses different loading patterns, which are heterogeneous.

As the SNF assembly diversions happen closer to the center of the cask, where the detectors are positioned, the  $\beta$  probability decreases significantly as it becomes easier to detect the diversion (and substitution) of the assemblies. Two assembly diversions (DS6 through DS8) and the open lid scenario (DS0) provide large drops in thermal neutron flux and hence they are always 100% detectable.

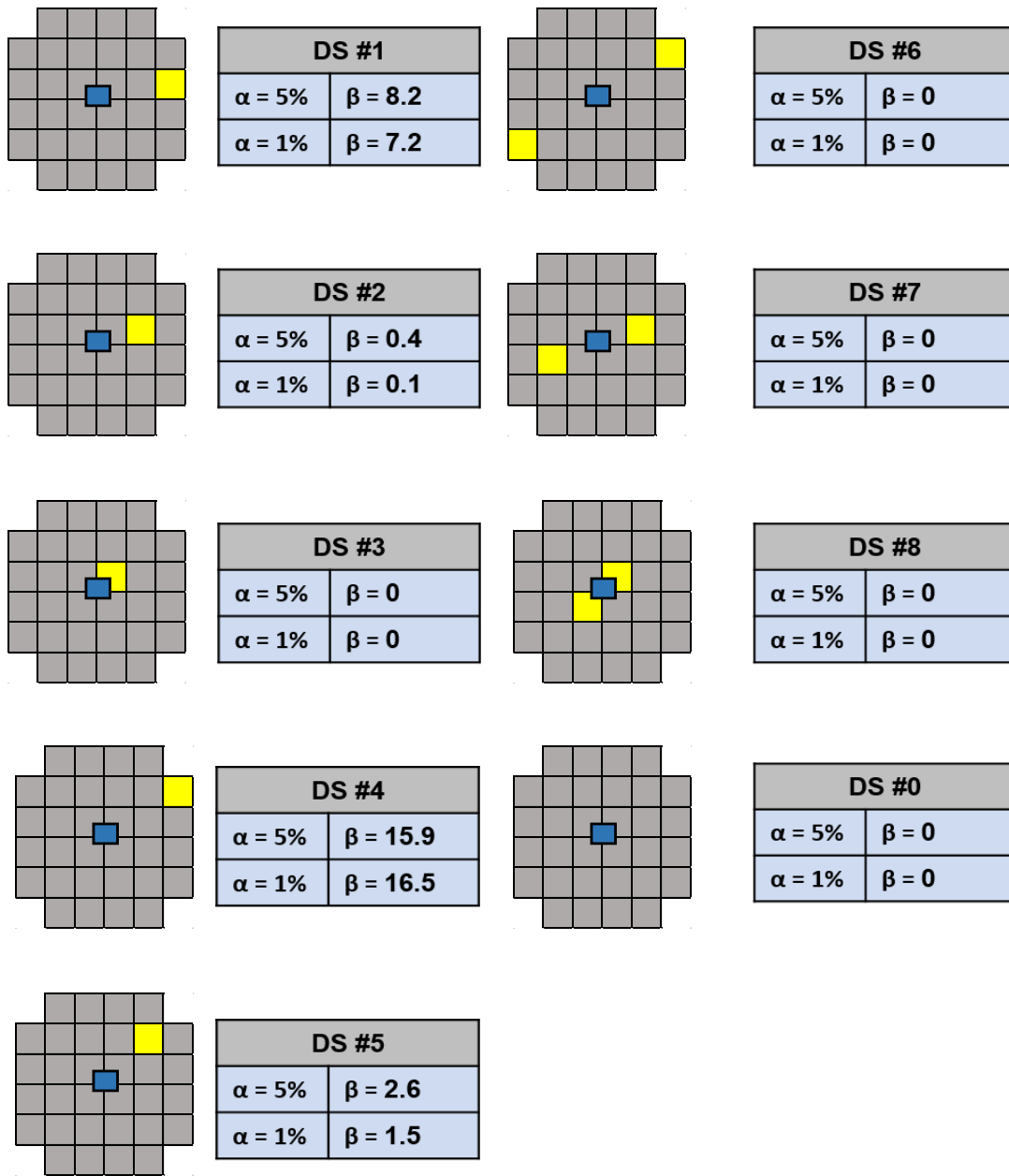


Figure 6-5  $\beta$  probabilities (%) for all diversion scenarios at 5%  $\alpha$  threshold using 5- second measurement time and 1%  $\alpha$  threshold using a 9- second measurement time

#### 6.4.1. Minimum Measurement Time

The goal of the RMS designs proposed is to be able to continually verify the presence of SNF assemblies inside the dry cask. In order to comply with this goal, measurements of neutron signal must be provided to the authorities in real time or as close to as possible. Hence, it is important to keep the measurement time relatively low. For a false alarm threshold of 5%, the measurement time was not to exceed five minutes to obtain  $\beta$  probabilities under 20% for all the SNF assembly diversion scenarios. Using these goals, the minimum measurement time (MMT) of both RMS systems is calculated.

The dominant neutron emitting isotope in PWR SNF is  $^{244}\text{Cm}$  [78]. It has a relatively short half-life of 18.1 years. In order to approximate the MMT of the system, it was assumed that all the neutrons come from  $^{244}\text{Cm}$  alone. Applying the radioactive decay equation for the known half-life of  $^{244}\text{Cm}$  and the given initial neutron emission rate ( $\text{n}\cdot\text{s}^{-1}$ ), the final neutron emission rate is

$$N = N_0 e^{-\lambda \cdot t} \quad \text{Eq. 6-1}$$

where  $N$  is the final neutron emission rate ( $\text{n}\cdot\text{s}^{-1}$ ),  $N_0$  is the initial neutron emission rate ( $\text{n}\cdot\text{s}^{-1}$ ),  $\lambda$  is the decay constant ( $\text{s}^{-1}$ ) and  $t$  is measurement time (s). When a dry cask is fully loaded, the neutron emission rate is  $1.52\text{E}+10 \text{ n}\cdot\text{s}^{-1}$ . Using Equation 6-1, the final neutron emission rate was calculated for up to ten half-lives of  $^{244}\text{Cm}$ .

From Figures 6-3 and 6-5, for a 5%  $\alpha$  probability, the diversion scenarios with the highest  $\beta$  probabilities are found to be for the diversion scenarios DS1 and DS4 for

both RMS designs. In order to minimize the measurement time, for a given neutron emission rate, the  $\beta$  probability is calculated as a function of time.

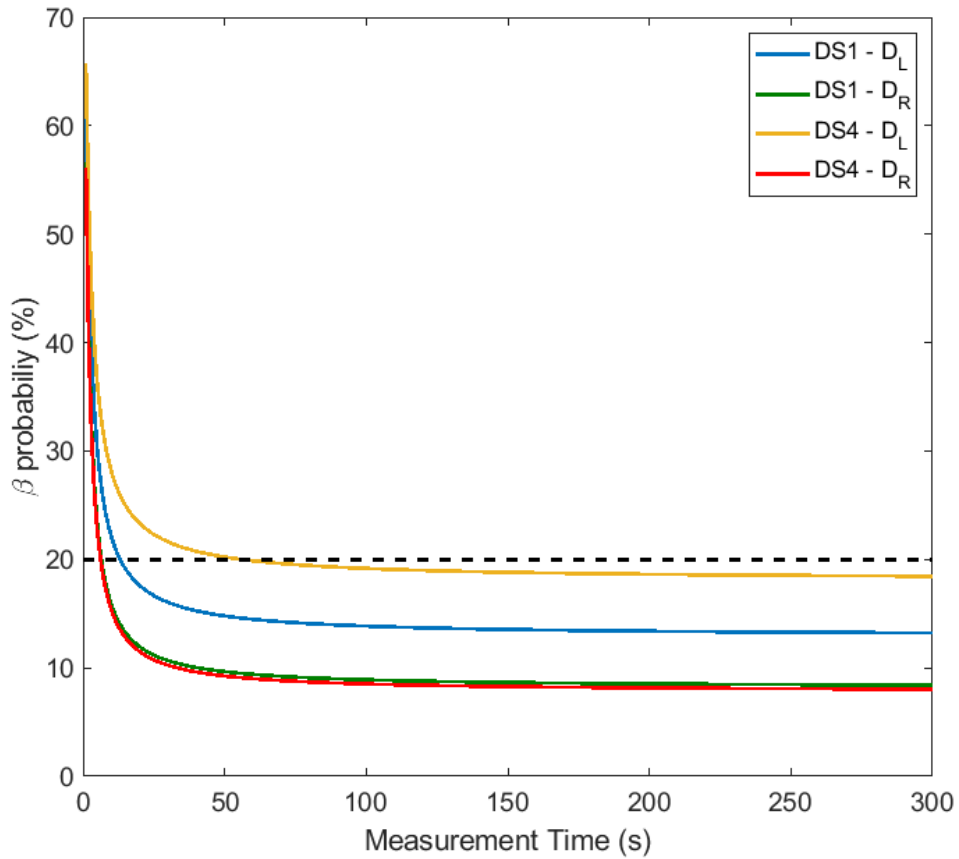


**Figure 6-6  $\beta$  probabilities (%) versus measurement time in the left, D<sub>L</sub> and right, D<sub>R</sub> detectors for DS1 and DS4 after 45 years of initial loading in the dry cask.**

If the dry cask is used as intended for a ~40-year lifetime, which is 2.5 half-lives later, the neutron emission rate will be  $2.69 \text{ E}+09 \text{ n.s}^{-1}$  (18% of the original). Figure 6-6 shows the response of the internal RMS with the right,  $D_R$  and left,  $D_L$  detectors for DS1 and DS4 after 2.5 half-lives (45.2 years) after the initial loading in the dry cask. Using this activity,  $D_L$  takes 14 seconds for DS1 and 57 seconds for DS4 to identify the diversion of an assembly for  $\beta$  probability to be less than 20%. For  $D_R$ ,  $\beta$  probabilities less than 20% are achieved for both diversion scenarios for a measurement time of 7 seconds. The measurement time of 7 seconds meets the criteria of being less than five minutes. Hence, if used as intended, the measurement system will work well as a ‘real time’ RMS for the entirety of its deployment.

Figure 6-7 shows the response of the external cask detector for DS1 and DS4 as a function of measurement time, after 2.5 half-lives (45.2 years) after the initial loading. The external RMS takes 127 seconds for DS1 and 151 seconds for DS4 to obtain  $\beta$  probabilities less than 20%. While these measurement times are much longer than that of the internal RMS, they are still well under the criteria of being less than five minutes. Therefore, these detectors are also capable of working well as a ‘real time’ RMS for the entirety of its deployment.

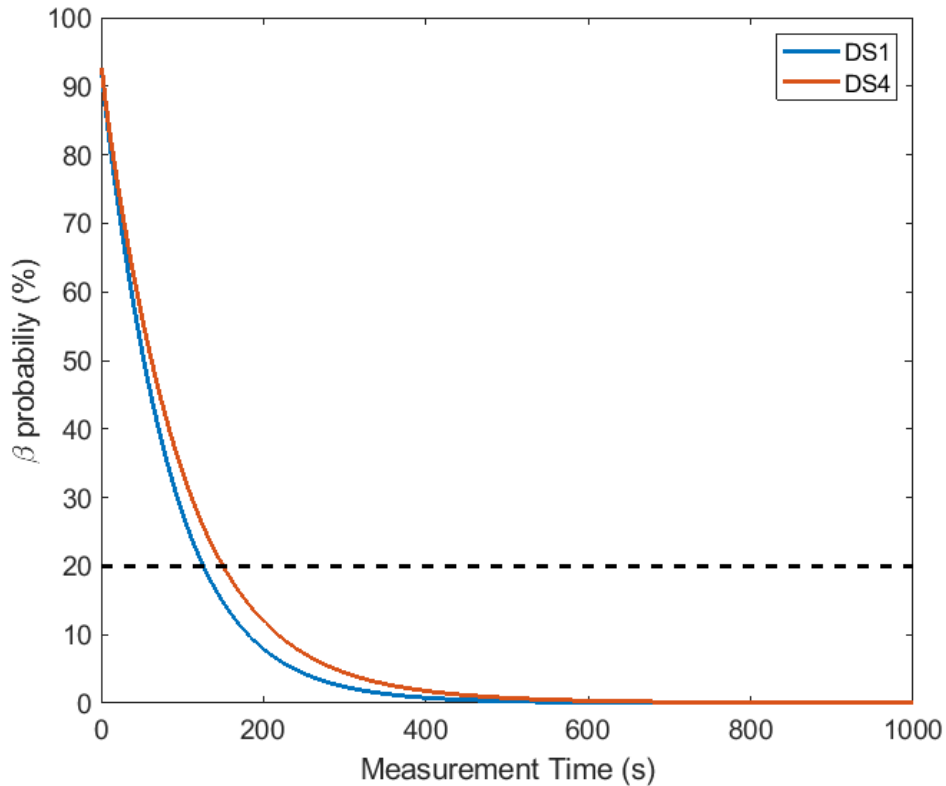


**Figure 6-7  $\beta$  probabilities (%) versus measurement time in the external RMS for DS1 and DS4 after 45 years of initial loading in dry cask.**

After ten half-lives, at 181.1 years, neutron emission rate is 0.1% of the original corresponding to  $1.48E+07 \text{ n.s}^{-1}$ . Figure 6-8 shows the response of the internal RMS with the right,  $D_R$  and left,  $D_L$  detectors for DS1 and DS4 after ten half-lives since initial loading.

Looking at DS1 of  $D_L$ , in order to obtain a  $\beta$  probability less than 20%, the measurement time needs to exceed 1130 seconds (18.83 minutes). In DS4, the same would be achieved in a 2.8-hour (171.2 minutes) measurement. For  $D_R$ ,  $\beta$  probabilities becomes less than 20% for both diversion scenarios at 1130 seconds (18.8 minutes).

These cases highlight the worst performance of the RMS, 181 years after initial loading.  $D_R$  performs much better than  $D_L$ , because the diversions taking place are closer in distance to  $D_R$ . In the event that  $D_R$  was broken, and  $D_L$  had to be relied on for one of these diversion scenarios, it would be extremely challenging/impossible to detect the diversion.

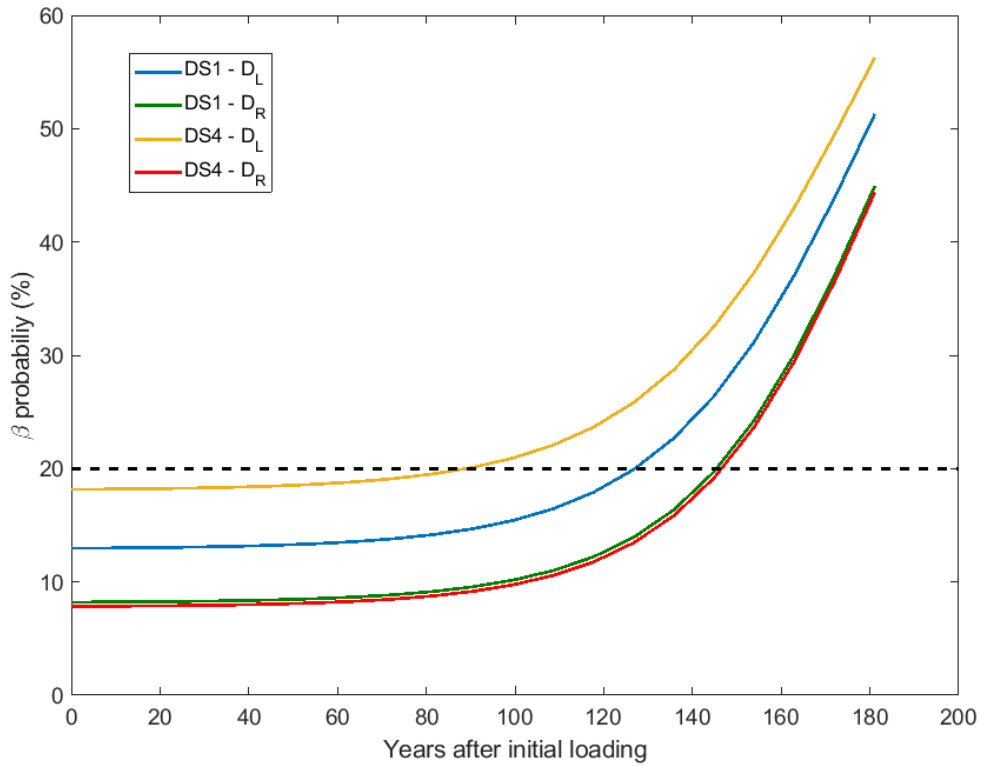


**Figure 6-8  $\beta$  probabilities for both detectors for DS1 and DS4 with the internal RMS as a function of time since initial cask loading.**

For the external RMS, it is seen that after ~ 60 years of initial loading, it becomes challenging to detect DS1 and DS4 with  $\beta$  probabilities less than 20%, for a 5-minute measurement, which is shown in Figure 6-9.

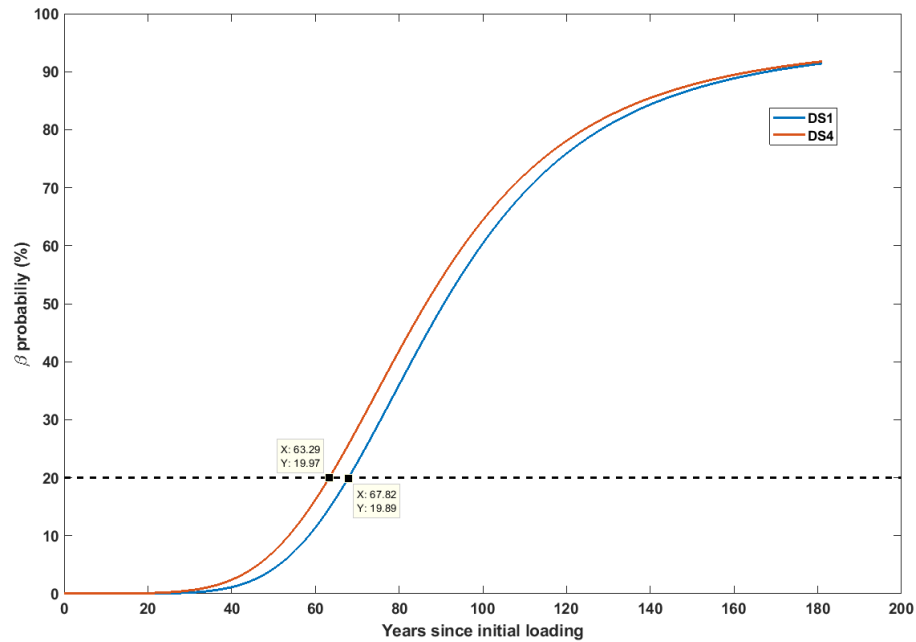


**Figure 6-9  $\beta$  probabilities (%) for DS1 and DS4 with external RMS as a function of time since initial cask loading**

The point at which measurement time exceeds 5 minutes for both diversion scenarios to obtain  $\beta$  probabilities less than 20% is 126.8 years for DS1 and 81.5 years for DS4 in  $D_L$ . Hence, as a conservative approach, 4.5 half-lives (81.5 years) is chosen for  $D_L$ . The same for  $D_R$  is 8 half-lives (145 years) after initial loading. If both detectors are functional, after 145 years of deployment, using the RMS would be impractical for a

real time monitoring system. If any one of the detectors fails, this number changes to 81.5 years.

## 7. CHARACTERIZATION OF RMS DESIGNS FOR HETEROGENEOUS SNF LOADING PATTERNS

The next set of MCNP simulations used real cask loading data from Oak Ridge National Laboratory that were available in literature [58]. The three loading patterns (LPs) provide a chance to test both the internal and external RMS designs with actual neutron source term values. However, there are some assumptions to be made using these loading patterns. There were no isotopic inventories or energy spectrum for the fuel, hence the same composition and energy spectrum were employed as before. The energy spectrum was that from a 4% initial enrichment, fuel burnup of 45 GWD/ MTU and a cooling time of 3 years. The source term values provided were the average neutron emission rate per assembly in units of neutrons per second ( $n.s^{-1}$ ).

Since symmetry can no longer be applied for diversion scenarios (DS), each assembly was diverted one at a time and replaced with a fresh fuel dummy assembly. The corresponding results and counting times are discussed in the following sections for both the internal and external RMS designs. The minimum time needed to achieve  $\beta$  probabilities less than 20% was chosen as the measurement time. Increasing the time further will decrease the  $\beta$  probabilities. For all diversion scenarios, a 5%  $\alpha$  threshold is used.

The oldest and coolest (low neutron emission rate) fuel is from LP2 which has an average neutron source strength of  $1.186E+08 n.s^{-1}$ . In this LP, generally, the coolest assemblies are placed in the center, surrounded by medium/hot SNF assemblies.

Following that, LP1 and LP3 are medium neutron strength with an average neutron emission rate of  $1.468\text{E}+08 \text{ n.s}^{-1}$  and  $1.510\text{E}+08 \text{ n.s}^{-1}$  respectively.

For both RMS designs, the individual assembly contributions will be discussed in the following sections. Since the loading pattern is heterogenous, neutron emission rate coupled with the assembly location (proximity to detectors and solid angle) are factors that determine the contributions of each assembly.

	29	30	31	32	
	1.23E+08	1.26E+08	1.27E+08	1.28E+08	
23	24	25	26	27	28
1.23E+08	1.48E+08	1.50E+08	1.51E+08	1.50E+08	2.01E+08
17	18	19	20	21	22
1.56E+08	1.49E+08	1.50E+08	1.27E+08	1.27E+08	1.51E+08
11	12	13	14	15	16
1.56E+08	1.29E+08	1.55E+08	1.48E+08	1.30E+08	1.57E+08
5	6	7	8	9	10
1.55E+08	1.59E+08	1.30E+08	1.23E+08	1.60E+08	1.56E+08
	1	2	3	4	
	1.57E+08	1.61E+08	1.67E+08	1.69E+08	

Loading Pattern 1

	29	30	31	32	
	1.22E+08	1.23E+08	1.22E+08	1.22E+08	
23	24	25	26	27	28
1.23E+08	1.21E+08	1.57E+08	1.57E+08	1.97E+08	1.96E+08
17	18	19	20	21	22
1.16E+08	1.64E+08	1.57E+08	1.58E+08	1.67E+08	1.20E+08
11	12	13	14	15	16
1.21E+08	1.60E+08	1.65E+08	1.77E+08	1.21E+08	1.86E+08
5	6	7	8	9	10
1.90E+08	1.83E+08	1.23E+08	1.23E+08	1.97E+08	1.95E+08
	1	2	3	4	
	1.13E+08	1.16E+08	1.54E+08	1.87E+08	

Loading Pattern 3

	29	30	31	32	
	1.36E+08	1.37E+08	1.39E+08	1.36E+08	
23	24	25	26	27	28
1.07E+08	1.07E+08	7.30E+07	7.15E+07	1.08E+08	1.01E+08
17	18	19	20	21	22
1.13E+08	7.16E+07	7.33E+07	7.34E+07	7.47E+07	1.15E+08
11	12	13	14	15	16
1.27E+08	7.17E+07	1.25E+08	1.64E+08	1.13E+08	1.31E+08
5	6	7	8	9	10
1.34E+08	1.62E+08	1.13E+08	1.13E+08	1.62E+08	1.64E+08
	1	2	3	4	
	1.44E+08	8.97E+07	1.99E+08	1.47E+08	

Loading Pattern 2

Name	Color	Range (n.s <sup>-1</sup> )
Cool	Cool	7.00E+07 - 1.32E+08
Medium	Medium	1.32E+08 - 1.76E+08
Hot	Hot	> 1.76E+08

Figure 7-1 Three different loading patterns where the numbers in each box are the assembly number, and average neutron emission rate (n.s<sup>-1</sup>)

### 7.1. Internal RMS Results for Various Heterogeneous Loading Patterns

In the heterogeneous loading patterns, each SNF assembly has different neutron emission rates. Hence, to characterize the RMS for the three heterogeneous loading patterns, each assembly was diverted one at a time and replaced with a fresh fuel dummy assembly. The percentage contributions of each assembly to the thermal neutron flux in the left detector,  $D_L$  and right detector,  $D_R$  and the corresponding  $\beta$  probabilities for all diversion scenarios are shown in Figure 7-2. The measurement time is the minimum time needed by both detectors in the internal RMS to achieve  $\beta$  probabilities less than 20% and is indicated in Figure 7-2. For each assembly, the top to bottom numbers are the assembly number, assembly contributions (%) and the  $\beta$  probability (%) for the particular assembly diversion. The boxes in black represent assembly diversion scenarios where the  $\beta$  probability exceeded 15%, indicating a challenge to detect the diversion. While the aim is to keep this number less than 20% for single assembly diversions, characterizing the RMS to obtain low  $\beta$  probabilities is essential. All other assembly colors indicate the neutron emission rate as in Figure 7-1.

### Loading Pattern 1

$D_L$						$D_R$					
$t = 9 \text{ s}$											
		29	30	31	32			29	30	31	32
		2.17	2.32	2.15	1.72			1.65	2.11	2.36	2.24
		2.7	1.4	2.9	12.0			14.4	3.4	1.2	2.0
23	24	25	26	27	28	23	24	25	26	27	28
2.37	3.68	4.02	3.6	2.72	2.5	1.53	2.67	3.57	4.05	3.73	3.88
1.2	0.0	0.0	0.0	0.2	0.8	19.7	0.3	0.0	0.0	0.0	0.0
17	18	19	20	21	22	17	18	19	20	21	22
3.56	4.54	5.01	3.67	2.72	2.12	2.18	3.17	4.35	4.21	3.87	3.44
0.0	0.0	0.0	0.0	0.2	3.4	2.6	0.0	0.0	0.0	0.0	0.0
11	12	13	14	15	16	11	12	13	14	15	16
3.56	3.92	5.17	4.33	2.77	2.21	2.18	2.74	4.48	4.93	3.94	3.57
0.0	0.0	0.0	0.0	0.2	2.4	2.7	0.2	0.0	0.0	0.0	0.0
5	6	7	8	9	10	5	6	7	8	9	10
2.99	3.94	3.49	2.93	2.89	1.94	1.92	2.86	3.09	3.29	3.96	3
0.0	0.0	0.0	0.1	0.1	6.4	6.7	0.1	0.0	0.0	0.0	0.0
	1	2	3	4			1	2	3	4	
	2.76	2.99	2.81	2.28			2.11	2.71	3.08	2.97	
	0.2	0.0	0.1	1.8			3.5	0.2	0.0	0.1	

### Loading Pattern 2

$D_L$						$D_R$					
$t = 11 \text{ s}$											
		29	30	31	32			29	30	31	32
		3.06	3.23	3	2.33			2.31	2.91	3.26	3
		0.1	0.0	0.1	2.1			2.1	0.1	0.0	0.1
23	24	25	26	27	28	23	24	25	26	27	28
2.64	3.39	2.49	2.17	2.49	1.59	1.68	2.44	2.19	2.42	3.38	2.45
0.5	0.0	0.9	3.3	1.0	19.3	15.0	1.1	2.8	1.1	0.0	1.0
17	18	19	20	21	22	17	18	19	20	21	22
3.27	2.77	3.11	2.71	2.03	2.05	1.99	1.92	2.68	3.08	2.86	3.3
0.0	0.2	0.0	0.3	5.6	5.5	6.3	7.3	0.3	0.0	0.1	0.0
11	12	13	14	15	16	11	12	13	14	15	16
3.67	2.78	5.31	6.1	3.07	2.35	2.23	1.92	4.56	6.88	4.33	3.77
0.0	0.2	0.0	0.0	0.1	1.9	2.7	7.2	0.0	0.0	0.0	0.0
5	6	7	8	9	10	5	6	7	8	9	10
3.29	5.11	3.88	3.44	3.72	2.6	2.09	3.67	3.4	3.83	5.05	3.98
0.0	0.0	0.0	0.0	0.0	0.7	4.5	0.0	0.0	0.0	0.0	0.0
	1	2	3	4			1	2	3	4	
	3.23	2.12	4.28	2.53			2.45	1.9	4.65	3.26	
	0.0	4.2	0.0	0.9			1.2	7.9	0.0	0.0	

### Loading Pattern 3

$D_L$						$D_R$					
$t = 10 \text{ s}$											
		29	30	31	32			29	30	31	32
		2.07	2.2	1.98	1.59			1.55	1.97	2.14	2.03
		2.3	1.2	3.3	13.1			13.3	3.0	1.4	2.4
23	24	25	26	27	28	23	24	25	26	27	28
2.3	2.91	4.06	3.61	3.45	2.35	1.46	2.08	3.55	4	4.66	3.6
0.8	0.0	0.0	0.0	0.0	0.7	17.3	1.9	0.0	0.0	0.0	0.0
17	18	19	20	21	22	17	18	19	20	21	22
2.55	4.81	5.07	4.43	3.45	1.62	1.54	3.31	4.34	5.01	4.84	2.59
0.2	0.0	0.0	0.0	0.0	11.8	13.8	0.0	0.0	0.0	0.0	0.1
11	12	13	14	15	16	11	12	13	14	15	16
2.65	4.72	5.34	4.99	2.5	2.53	1.6	3.25	4.56	5.6	3.5	4.04
0.1	0.0	0.0	0.0	0.3	0.3	11.5	0.0	0.0	0.0	0.0	0.0
5	6	7	8	9	10	5	6	7	8	9	10
3.56	4.38	3.18	2.83	3.43	2.35	2.25	3.13	2.77	3.14	4.62	3.58
0.0	0.0	0.0	0.0	0.0	0.8	1.0	0.0	0.0	0.0	0.0	0.0
	1	2	3	4			1	2	3	4	
	1.91	2.08	2.5	2.44			1.44	1.86	2.7	3.12	
	4.3	2.2	0.3	0.5			18.1	4.7	0.1	0.0	

Figure 7-2 Three loading patterns where the top to bottom numbers are the assembly number, assembly contributions (%) to the left and right detectors respectively and the  $\beta$  probability (%) for the particular assembly diversion

Bottom line up front, from all three LPs, the following can be concluded:

- Assembly diversions in the center (DS14, DS14, DS19 and DS20) are always the easiest to detect ( $\beta < 0.5\%$ ) due to proximity to the detectors.
- Assemblies that contribute the least to the to the thermal neutron flux recorded by the detectors are the cool assemblies that are in the periphery of the cask
- Hot assembly diversions are easily detectable by the internal RMS regardless of assembly position
- The internal RMS response is very fast (maximum time required is 11 seconds) to classify if a diversion has occurred. However, this is longer than the 2-second measurement time for homogenous fuel.

From Figure 7-2, for all the LPs, using a 5%  $\alpha$  threshold, it takes 9-11 seconds of measurement time to ensure that all  $\beta$  probabilities for every DS is less than 20% in both detectors. The DSs that are the most challenging to detect shown in red boxes. These DSs are of cool assemblies that are in the periphery of the cask that each contribute less than 1.8% of the total thermal neutron flux observed by the respective detectors. The low contribution can be attributed to the small solid angle shared with the detector due to distance and low neutron emission rate. Diverting assemblies that contribute less, only slightly perturbs the total thermal neutron flux recorded by the detectors. If the perturbation is too small, it may fall within statistical uncertainties and fail to be detected as a diversion. To overcome this, increasing the measurement time to 20 seconds reduces

$\beta$  probabilities for every DS below 5% for all LPs. A longer measurement time reduces statistical uncertainties, hence lowers  $\beta$  probabilities for DSs.

## **7.2. External RMS Results for Various Heterogenous Loading Patterns**

Figure 7-3 shows the percentage contributions of each assembly to the thermal neutron flux recorded external RMS detectors and the corresponding  $\beta$  probabilities for all diversion scenarios. The measurement time is the minimum time needed by both detectors in the internal RMS to achieve  $\beta$  probabilities less than 20%. All scenarios used a 5%  $\alpha$  threshold. In general, the external RMS takes a longer measurement time than the internal RMS (~30 seconds vs ~10 seconds) to provide similar results. The longer measurement time is needed due to the attenuation of neutrons in concrete and stainless-steel lid. The shielding in the lid decreases the thermal neutron flux observed by the external RMS by two orders of magnitude (refer to Tables 5-1 and Table 5-2). Thus, increasing the measurement time allows good counting statistics to be achieved.

From Figure 7-3, similar to the internal RMS, the assembly diversion scenarios that are challenging to detect are the assemblies that are cool and in the periphery of the cask. Diversion scenarios that have  $\beta$  probabilities more than 15% are depicted by the black boxes. In all cases, each of these assemblies contributed less than 2.3% to the detectors in the external RMS. Increasing the measurement time will decrease  $\beta$  probabilities.

**Loading Pattern 1**

**t = 24 s**

	29 2 18.5	30 2.3 9.1	31 2.4 8.3	32 2.1 16.0	
23 2 17.9	24 3.2 0.5	25 3.8 0.0	26 3.9 0.0	27 3.3 0.4	28 3.3 0.5
17 2.9 1.7	18 3.8 0.0	19 4.6 0.0	20 3.9 0.0	21 3.3 0.3	22 2.8 2.3
11 2.9 1.6	12 3.3 0.3	13 4.7 0.0	14 4.5 0.0	15 3.4 0.3	16 3 1.5
5 2.5 5.5	6 3.5 0.2	7 3.3 0.3	8 3.2 0.6	9 3.5 0.1	10 2.6 5.3
	1 2.5 5.7	2 3 1.2	3 3.1 1.0	4 2.8 3.0	

**Loading Pattern 2**

**t = 27 s**

	29 2.74 4.3	30 3.15 1.2	31 3.21 1.0	32 2.73 4.5	
23 2.17 15.2	24 2.91 2.4	25 2.33 10.0	26 2.29 11.1	27 2.95 2.1	28 2.05 19.1
17 2.63 5.4	18 2.3 10.8	19 2.8 2.8	20 2.79 2.8	21 2.39 8.6	22 2.67 4.9
11 2.97 2.1	12 2.31 10.5	13 4.75 0.0	14 6.27 0.0	15 3.64 0.1	16 3.09 1.5
5 2.72 4.4	6 4.4 0.0	7 3.62 0.2	8 3.61 0.2	9 4.46 0.0	10 3.33 0.7
	1 2.89 2.9	2 2.09 17.6	3 4.58 0.0	4 2.99 2.1	

**Loading Pattern 3**

**t = 32 s**

	29 2.07 13.3	30 2.2 3.0	31 1.98 1.4	32 1.59 2.4	
23 2.3 17.3	24 2.91 1.9	25 4.06 0.0	26 3.61 0.0	27 3.45 0.0	28 2.35 0.0
17 2.55 13.8	18 4.81 0.0	19 5.07 0.0	20 4.43 0.0	21 3.45 0.0	22 1.62 0.1
11 2.65 11.5	12 4.72 0.0	13 5.34 0.0	14 4.99 0.0	15 2.5 0.0	16 2.53 0.0
5 3.56 1.0	6 4.38 0.0	7 3.18 0.0	8 2.83 0.0	9 3.43 0.0	10 2.35 0.0
	1 1.91 18.1	2 2.08 4.7	3 2.5 0.1	4 2.44 0.0	

**Figure 7-3 Three loading patterns where the top to bottom numbers are the assembly number, assembly contributions (%) to the detectors in the external RMS and the  $\beta$  probability (%) for the particular assembly diversion**

### 7.3. Conclusions

The following can be concluded regarding both RMS designs:

- Assembly diversions in the center are always the easiest to detect due to proximity to the detectors.
- Increasing the measurement time will decrease  $\beta$  probabilities for DSs.
- Cool assembly that share small solid angle with the detectors are the most challenging to detect when diverted as they contribute the least to the thermal neutron flux recorded.
- The internal RMS is capable of identifying DS in 1/3 of the time taken by the external RMS. But both systems require much less than 5 minutes to determine if a diversion has occurred.

Using these conclusions, the RMS design can be chosen based on the nature of SNF assembly within a dry cask and other limiting factors like measurement time. Both RMSs perform well under the 20%  $\beta$  probability limit for a 5%  $\alpha$  threshold and measurement time under 5 minutes. The study carried out on heterogeneous loading patterns gave insight that which type of loading pattern can support easy safeguards monitoring. How to load the most cooled, medium cooled and hot SNF assemblies is important from the perspective of keeping non-detection probabilities less than 20% which can be used at the time of SNF assembly loading in the dry cask. Also, these studies brought out the advantages and disadvantages of internal and external RMS designs when used in the case of heterogeneous loading patterns.

## 8. CHARACTERIZATION OF RMS FOR MULTIPLE CASK SCENARIO

At present, dry casks are stored in licensed independent spent fuel dry storage installations (ISFSI). Typically, there are two designs: vertical and horizontal storage. For this work, vertical storage is considered. In this chapter, results of MCNP simulations of nine dry casks in a 3 x 3 array were performed to determine the effect of surrounding casks on the performance of the external RMS. The external RMS was specifically chosen for this study as it is subject to the environment it is placed in and the counts recorded by the detectors will vary based on background radiation levels. The internal RMS on the other hand is within the dry cask and is heavily shielded such that the external environment does not significantly affect the signal seen by the detectors within.

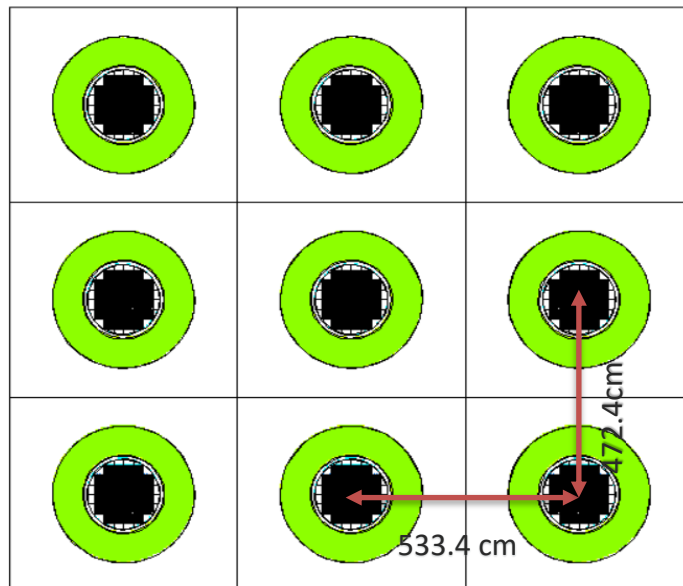


**Figure 8-1** Nine fully loaded dry casks

For all the MCNP simulations performed, the same detailed cask model as before was used but are replicated to form nine casks. Figure 8-1 shows a top view of the nine dry casks that is filled with 32 SNF assemblies per dry cask. In this scenario, all casks contain a homogeneous loading of fuel which has a burnup of 45 GWd/MTU and cooling time of 3 years. Each cask has an external RMS on its lid. The spacing between each cask was obtained from Comanche Peak Nuclear Power Plant [38] that follows regulations to accommodate for radiation dose rates as well as potential for knocking over during seismic events. The distances between casks are shown in Figure 8-1.

To investigate the RMS characteristics, SNF assemblies were diverted from the central cask, one at a time and replaced with a dummy assembly. The corresponding  $\beta$  probabilities were recorded for each DS for  $\alpha$  of 5% and 1%. The results are shown in Table 8-1.

From Table 8-1, it can be noted that for an  $\alpha$  value of 5% the measurement time required to obtain  $\beta$  probabilities less than 20% is about 82 seconds for all DS. However, when a single cask was modelled without accounting for contributions of surrounding casks, the measurement time required to obtain  $\beta$  probabilities less than 20% for all DS was 5 seconds using a 5%  $\alpha$ . This increase in measurement time is observed when an external RMS is surrounded by other casks.

**Table 8-1  $\beta$  probabilities recorded for each DS for  $\alpha$  of 5% (t=82 s) and 1% (t=133s) for the multiple dry casks case with external RMS**

DS	$\beta$ probabilities (%)	
	$\alpha = 5\%$	$\alpha = 1\%$
1	0	0
2	0	0
3	0	0
4	0	0
5	0	0
6	0	0
7	0	0
8	0	0
9	0	0
10	1	0
11	0	0
12	0	0
13	0	0
14	0	0
15	0	0
16	0	0
17	0	0
18	0	0
19	0	0
20	0	0
21	0	0
22	0	0
23	0	0
24	0	0
25	0	0
26	0	0
27	0	0
28	19	19
29	0	0
30	0	0
31	0	0
32	0	0

Looking further into these numbers since there is additional signal in the multiple cask case, the average difference in neutron count rates for RS and all DS for the single cask case was 3.1% while the same in the multi-cask case is 2.6%. The smaller difference in signal between RS and DS causes a larger overlap between their gaussian distributions, thus a larger  $\beta$  probability for each DS. In order to decrease that number, measurement time has to be increased. The counts observed by the external RMS for the single and multi-cask cases are available in Appendix E.

Hence external factors like background radiation and proximity to other radiation sources can increase the measurement times required by the external RMS. However, since the time required is still very short, the external RMS concept is viable for this purpose.

Also, it is seen that decreasing  $\alpha$  from 5% to 1% increases the  $\beta$  probabilities, hence to keep those less than 20%, the measurement time is increased to 133 seconds such that all  $\beta$  probabilities can be less than 20% for each DS.

In an experiment setting, there may be more contributing factors that further increases the measurement time in order for good statistics to be achieved. However, if the measurement time is on the order of minutes, it is still considered reasonable as the authorities can be notified quickly in the event something has been tampered with.

## 9. EXPERIMENTS TO VERIFY INTERNAL RMS CAPABILITIES

The purpose of these experiments is to serve as verification of MCNP simulations of the internal RMS. The RMS is to be placed inside a dry cask filled with SNF. Since SNF or fresh fuel is difficult to attain for the planned experiments, five  $^{252}\text{Cf}$  neutron sources available at Texas A&M University (TAMU) were used to characterize the RMS. However, the goal was to obtain eight strong  $^{252}\text{Cf}$  neutron sources ( $> 0.5\text{mCi}$  each) in order to approximate  $\frac{1}{4}$  of the SNF assemblies in a dry cask. The experiments were to be performed at Oak Ridge National Laboratory and all optimizing simulations were done based on that assumption. Unfortunately, in March of 2020, the COVID-19 pandemic disallowed all TAMU related travel [83]. Hence, obtaining those  $^{252}\text{Cf}$  neutron sources for experiments were no longer feasible.

These proof-of-concept experiments were hence performed using five  $^{252}\text{Cf}$  neutron sources that were available in the Department of Nuclear Engineering at TAMU. The following steps describe the prior experimental planning carried out with eight strong  $^{252}\text{Cf}$  neutron sources. The same assumptions were used for fewer and weaker neutron sources at Texas A&M since the eight-neutron source experiments at ORNL could not be performed.

- 1) MCNP simulations using  $^{252}\text{Cf}$  as a surrogate for SNF.
  - a) Converting isotropic point source to an approximated surface source.
- 2) Downscaling a dry cask by:
  - a) Simulating  $\frac{1}{4}$  of a dry cask due to symmetry.

- b) Approximating concrete body shielding of dry cask.
- c) Approximating lid shielding of dry cask.

### 9.1. MCNP Simulations using $^{252}\text{Cf}$ as a Surrogate for SNF

$^{252}\text{Cf}$ , is a spontaneously fissioning isotope [84]. The dimensions of the available  $^{252}\text{Cf}$  are that of point sources. Further steps have been taken to approximate a point source as a surface source which are described later. Doing so will better mimic the response of detectors to the volumetric nature of SNF assemblies.

First, 32  $^{252}\text{Cf}$  point neutron sources, each with source strength of a SNF assembly is simulated in a similar configuration within the cask. The 8 diversion scenarios (shown in Figure 4-1) were performed for this new configuration. The same methodology described in previous chapters is applied to calculate  $\beta$  probabilities.

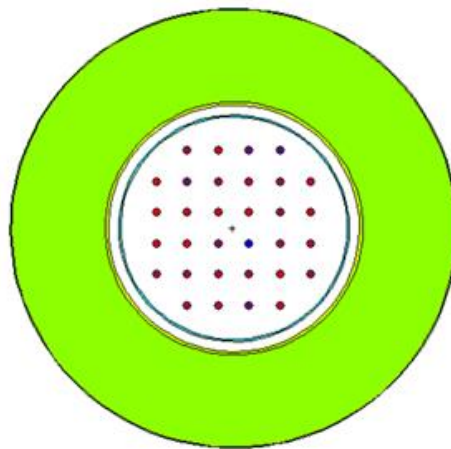


**Figure 9-1 Dots represent 32  $^{252}\text{Cf}$  point neutron sources in a dry cask. Reprinted from 43.**

For this case, every single diversion of point neutron source was 100 % detectable with a 1-second measurement time. This emphasizes that the geometry of SNF is inhibiting such that streaming of neutrons is blocked by surrounding assemblies therefore making it more difficult to detect DSs. Using  $^{252}\text{Cf}$  point sources negates the inherent shadowing and material induced effects of assemblies. Figure 9-1 shows a Visual Editor rendering of the point sources replacing the SNF assemblies within a dry cask, however maintaining the same source strength.

For the proof of concept experiments, eight  $^{252}\text{Cf}$  sources representing 1/4 of a dry cask was planned. Figure 9-2 shows a representation of 32 assemblies in a dry cask. It is then divided into 4 sections by the yellow lines. Each section represents 1/4 of a dry cask with eight assemblies.

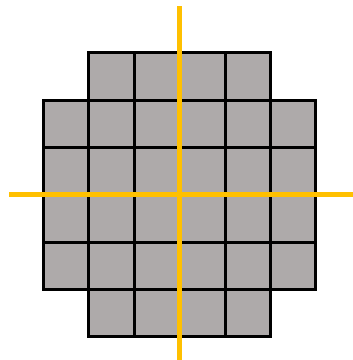


**Figure 9-2 Eight assemblies represent 1/4 of a dry cask**

Therefore, for the proof of concept experiments, eight  $^{252}\text{Cf}$  sources can be used to represent  $\frac{1}{4}$  of a cask.

### 9.1.1. Isotropic Point Source to Surface Source Approximation

An important distinction between SNF assemblies and  $^{252}\text{Cf}$  point neutron sources is the difference in geometry. SNF assemblies are large volumetric sources where streaming of neutrons is blocked by surrounding assemblies thus making it challenging to detect diversions.

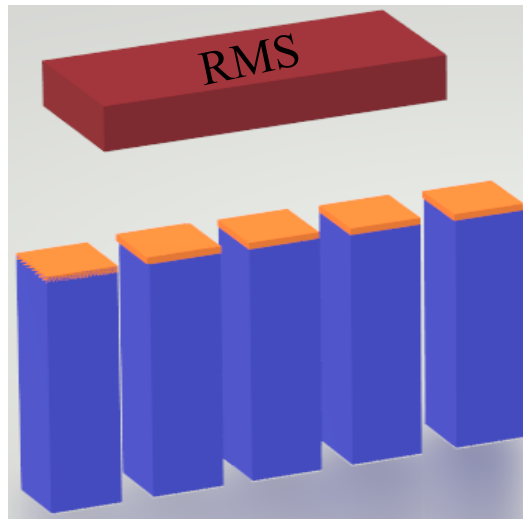


**Figure 9-3 The blue blocks represent SNF assemblies. The RMS (red block) is placed on top of the assemblies which appears as a surface source (yellow squares) to the detectors**

Figure 9-3 shows an illustration of the detectors field of view due to self-shielding of SNF assemblies and detector intrinsic efficiency. Since the RMS is placed

on the top of the MPC lid within the dry cask, the most actively contributing signal to the RMS is from the top portion of the SNF. From the view of the detectors, it is assumed that top surface of the SNF contributes the most. Hence, the RMS views the SNF as a surface source rather than a volumetric source. In Figure 9-3, the red block represents the RMS while the blue blocks represent assemblies. Due to self-attenuation and SNF assemblies shielding each other, the most crucial part of the SNF assemblies that is visible to the detector will be the top portion, highlighted in yellow. Since this is only for illustration purpose, it is not to scale.

Next, in order to compensate for the ‘point-like’ nature of  $^{252}\text{Cf}$  sources versus the volumetric nature of an SNF assembly,  $^{252}\text{Cf}$  sources are surrounded with reflecting material. The desirable characteristics of a reflector is its low thermal neutron absorption cross section and high scattering cross section [85]. For the purpose of these experiments,  $^{252}\text{Cf}$  was to be surrounded by a material that was good at reflecting and moderating to increase the number of thermal neutrons seen by the detectors as well as spread out the source. Employing these characteristics to a point  $^{252}\text{Cf}$  source, a smeared/spread thermal neutron signal depicting a surface source can be obtained. To determine these effects, a single  $^{252}\text{Cf}$  source surrounded by different reflecting material is simulated in MCNP. Mesh tallies providing average cell flux were used to determine the extent of smearing as well as the magnitude of reflection. The  $^{252}\text{Cf}$  source had the same strength as a single SNF assembly which was  $4.74 \text{ E}+08 \text{ ns}^{-1}$ . Geometry for this setup is shown in Figure 9-4.

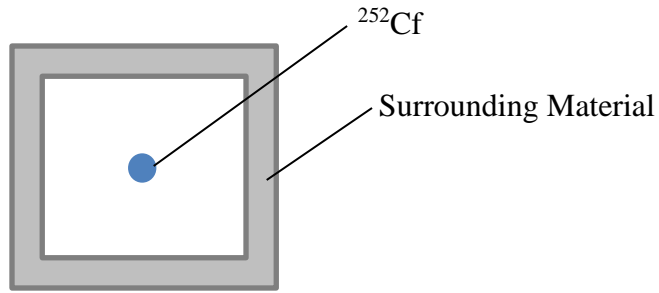


**Figure 9-4 Setup of  $^{252}\text{Cf}$  source and surrounding material for all simulations**

Moderators serve to slow down fission neutrons while reflectors scatter the neutrons back into the system that would have otherwise leaked. The Macroscopic Slowing-down Power (MSDP) is a measure of the ability of a given material to slow down neutrons [86]. However, a material with high MSDP can slow down neutrons with high efficiency, but it can be a poor moderator because of its high probability of absorbing neutrons. Hence the Moderating Ratio (MR) is a better measure of the effectiveness as a moderator because it considers the absorption effects. MSDP and MR are defined in Equation 9-1.

$$\text{MSDP} = \xi \Sigma_S \quad \text{MR} = \xi \frac{\Sigma_S}{\Sigma_A} \quad \text{Eq. 9- 1}$$

$$\xi = 1 + \frac{(A - 1)^2}{2A} \ln\left(\frac{A - 1}{A + 1}\right)$$

where  $\xi$  is the average logarithmic energy loss per collision,  $A$  is the mass number and  $\Sigma_S$  and  $\Sigma_A$  are the macroscopic neutron scattering and neutron absorption cross section.

Some characteristics of these chosen materials are shown in Table 9-1. The cross sections are taken from the JEFF-3.1.1 library using JANIS software [87]. The initial energy of neutrons was assumed to be 2 MeV and slowed down to 0.025 eV.

**Table 9-1 Characteristics of potential moderator/reflector materials**

<b>Parameter</b>	<b>Graphite</b>	<b>Water</b>	<b>Beryllium</b>	<b>Polyethylene</b>
Density (g.cm <sup>-3</sup> )	1.70	1.00	1.85	0.93
$\Sigma_s$ (cm <sup>-1</sup> )	0.427	1.462	0.865	1.798
$\Sigma_A$ (th) (cm <sup>-1</sup> )	2.99E-04	0.022	0.001	0.027
$\xi$	0.158	0.920	0.207	0.906
MSDP	0.067	1.353	0.151	3.230
MR	225.384	61.323	160.387	122.950

Figure 9-5 shows the results of the mesh tallies above the selected materials surrounding a <sup>252</sup>Cf source. The numbers on the x and y axes represent the coordinates. The source was present in the center at -36.35, -15.45 for all simulations. In these simulations, the thickness of the material was kept at 2.54 cm.

For the same thickness, it is seen that polyethylene produces a thermal neutron flux that is approximately 3 times that produced by graphite. From Table 9-1, the

scattering cross section of polyethylene is 4.2 times larger than that of graphite, hence, the higher thermal flux seen is evident of this large scattering cross section difference. Polyethylene also has a higher absorption cross section (88 times more than graphite). However, for the purpose of this work, polyethylene serves as a better reflector and moderator than graphite. From Figure 9-5, there is a relatively even spread of thermal neutrons as opposed to a hot spot in the center for graphite. Graphite is also a good reflector and moderator but does not spread out the thermal flux as well as polyethylene. Notice the hotspot in the center for graphite which is not evident in polyethylene.

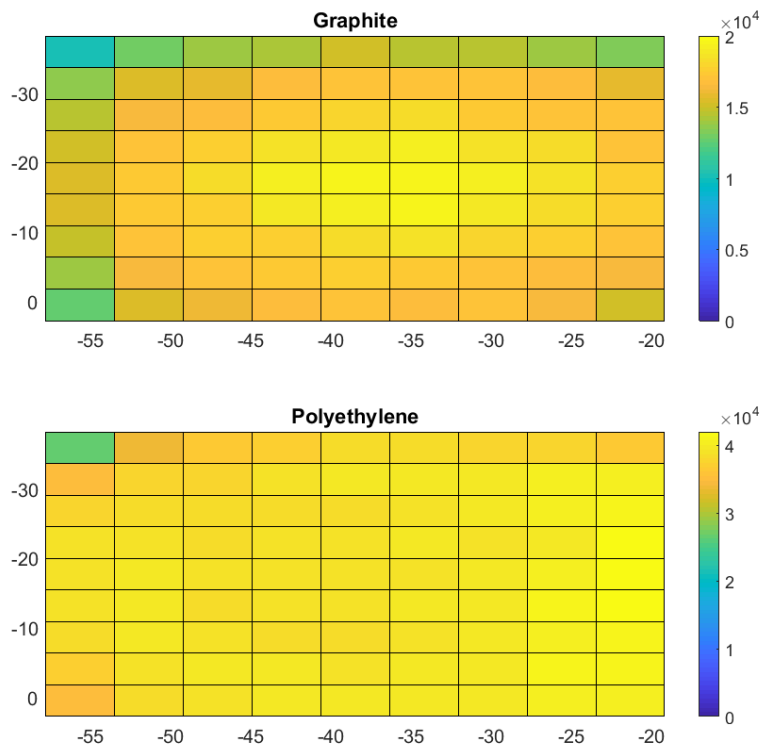


**Figure 9-5 Results of reflector study using a single <sup>252</sup>Cf source surrounded by different reflector materials**

### **9.1.2. Approximating Concrete Body Shielding of Dry Cask**

Concrete plays an important role in shielding neutron radiation within the dry casks. In the MCNP model of the dry cask, 70 cm of concrete is used to shield the SNF within. Also, thick concrete boundaries are used because heat is transferred through ducts, located at the cask wall. For the experiments done at Texas A&M, a boundary of concrete surrounding the  $^{252}\text{Cf}$  was necessary to increase reflection of neutrons back into the system. Heat transfer is not an issue for the scale of experiment that was conducted, hence the thickness of concrete was deemed sufficient for this purpose.

Using materials like solid concrete blocks that can be purchased from local stores, a concrete boundary was created. The thickness of the concrete blocks was 20.32 cm as opposed to the thickness of the concrete canister of the dry cask which was approximately 70 cm. Since only eight  $^{252}\text{Cf}$  sources, with a total neutron emission rate much less than that of the cask (<0.01 % of cask emissions) it was assumed that 20.32 cm thick concrete would suffice.

### **9.1.3. Approximating Lid of Dry Cask**

The concrete lid plays an important role for the detection of diversions using the internal RMS. This is because concrete provides a surface for reflection of neutrons into the RMS. This is represented by the 20 cm of concrete above the internal RMS shown in Figure 9-6. In the absence of a concrete lid, the thermal neutron flux in the RMS drops tremendously as proven in section 6.1.

It is important to notice that there is 24 cm of stainless steel beneath the internal RMS that acts as a primary barrier for radiation emitted by the SNF followed by 20 cm concrete and 2.54 cm stainless steel in the lid. All of this is to ensure that the radiation within the cask is properly shielded and the dose rates surrounding the cask are within acceptable limits. For experimental purposes, the amounts of stainless steel and concrete were reduced.

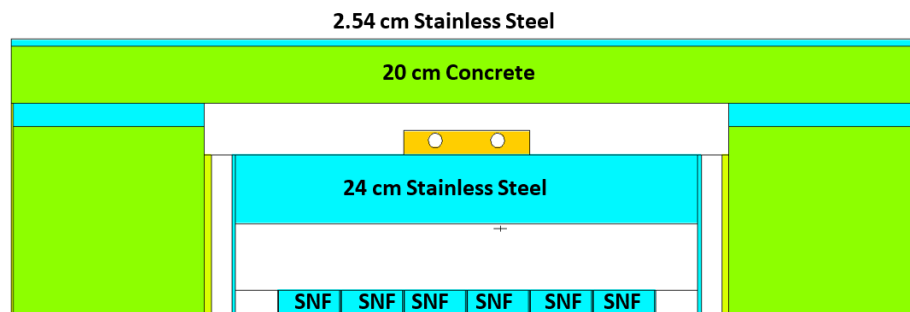


**Figure 9-6 VISED rendering of top part of dry cask containing SNF**

The thickness as well as the width of concrete for experimental purposes needed to be reduced from that of a dry cask. For all simulations, the setup is shown in Figure 9-7 where there were eight  $^{252}\text{Cf}$  sources in a single quadrant representing SNF.

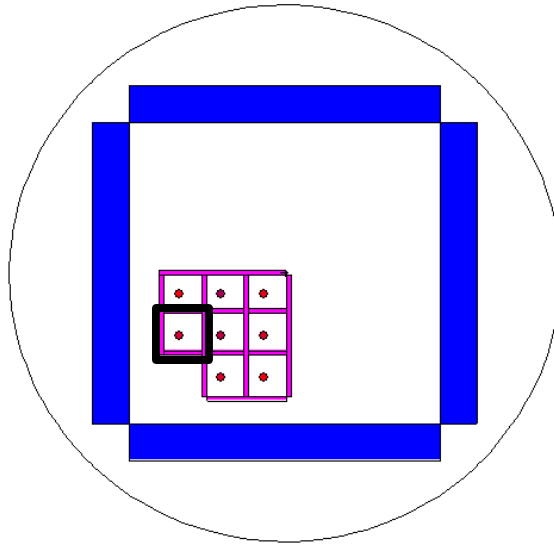


**Figure 9-7 VISED rendering of eight  $^{252}\text{Cf}$  point sources representing  $\frac{1}{4}$  the contents of a dry cask. The pink box surrounding each point source is the reflector material. A single black box in the bottom left corner indicates the position for the mesh tally. Blue boxes are concrete.**

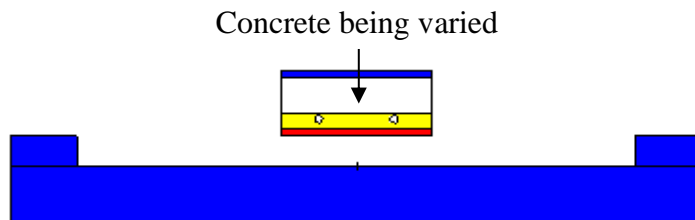


**Figure 9-8 VISED rendering of the thickness of concrete being varied. The blue boxes are concrete.**

Figure 9-8 shows a VISED rendering of the thickness of concrete being varied. The thickness of concrete was varied in 2.54 cm (1 inch) increments and the corresponding neutron flux in detector cell was obtained using average cell flux tallies in MCNP. These were then converted to neutron count rates using detector sensitivities provided in the manufacturer specification sheet. In order to determine the thickness of concrete, the width was first set to match to that of the RMS width which was 23 cm x 23 cm. Figure 9-9 shows the combined thermal neutron counts for a 1-second measurement time as a function of concrete thickness.

It is seen that as the thickness of concrete increases, the counts observed by the detectors also increase. This is expected as concrete has a high hydrogen content and acts as a moderator for neutrons. From Figure 9-9, the point of diminishing returns is 10.16 cm of concrete where the percentage increase in combined counts for every inch of concrete added was ~2% or less. 10.16 cm of concrete would be ideal for this system. However, even 2.54 cm of concrete provides enough reflection to determine the open lid diversion scenario case. Performing diversions of the  $^{252}\text{Cf}$  sources one at a time and calculating the  $\beta$  probabilities of the detector showed that even for the 2.54 cm thickness, the  $\beta$  probabilities for all diversion scenarios are 0 with a 1 s measurement time. Hence, it was decided that for the purpose of these experiments, 2.54 cm thickness of concrete is enough.

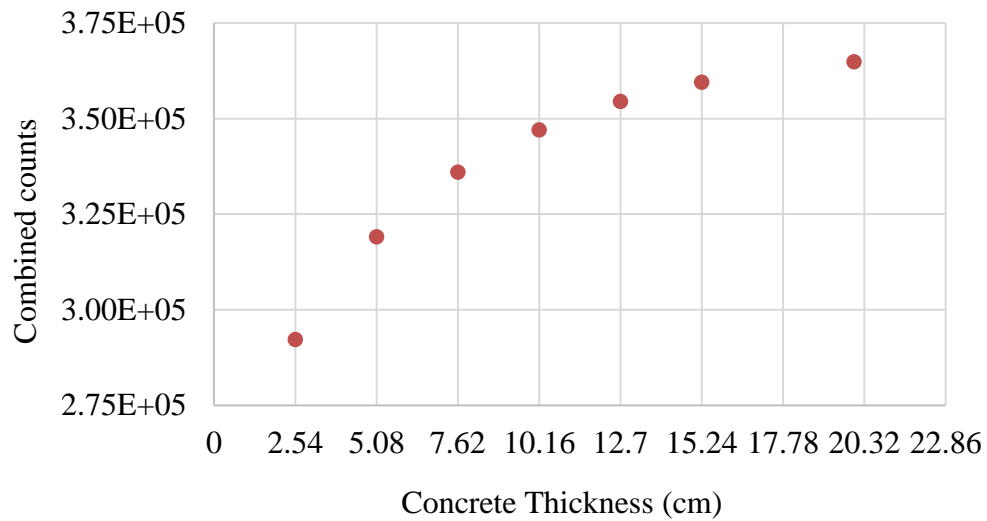


**Figure 9-9 Combined thermal neutron counts for 1-second measurement time as a function of concrete thickness**

The next step was to determine the width of concrete used. Using the same setup as before, the width of concrete was varied in four different steps from 23 cm x 23 cm to 30 cm x 30 cm, 40 cm x 40 cm and finally 50 cm x 50 cm. For this study, the thickness of concrete used was 2.54 cm. For comparison, a width of 10.16 cm was modelled additionally. The results of these cases are shown in Figure 9-10. The widths are labelled as sums such that the 23 cm x 23 cm is 46 cm, 30 cm x 30 cm is 60 cm, 40 cm x 40 cm is 80 cm and 50 cm x 50 cm is 100 cm.

**Table 9-2 Percentage increase in counts as a function of concrete thicknesses and varied widths and corresponding mass of concrete slab**

Width (cm)	2.54 cm		10.16 cm	
	% increase	Mass (kg)	% increase	Mass (kg)
23 x 23	-	3.43	-	13.71
30 x 30	4.21%	5.83	10.24%	23.32
40 x 40	8.19%	10.36	19.95%	41.45
50 x 50	10.97%	16.19	26.88%	64.77

Table 9-2 shows the percentage increase in counts recorded by the detectors combined for 1s measurement time as a function of concrete width for varied thicknesses. It also shows the mass of the concrete slab that needs to be hoisted. The point of diminishing returns is the combination of 10.16 cm thickness of concrete with a width of 40 cm x 40 cm (refer to 80 cm in Fig 9-10). This configuration weighs ~41 kg.

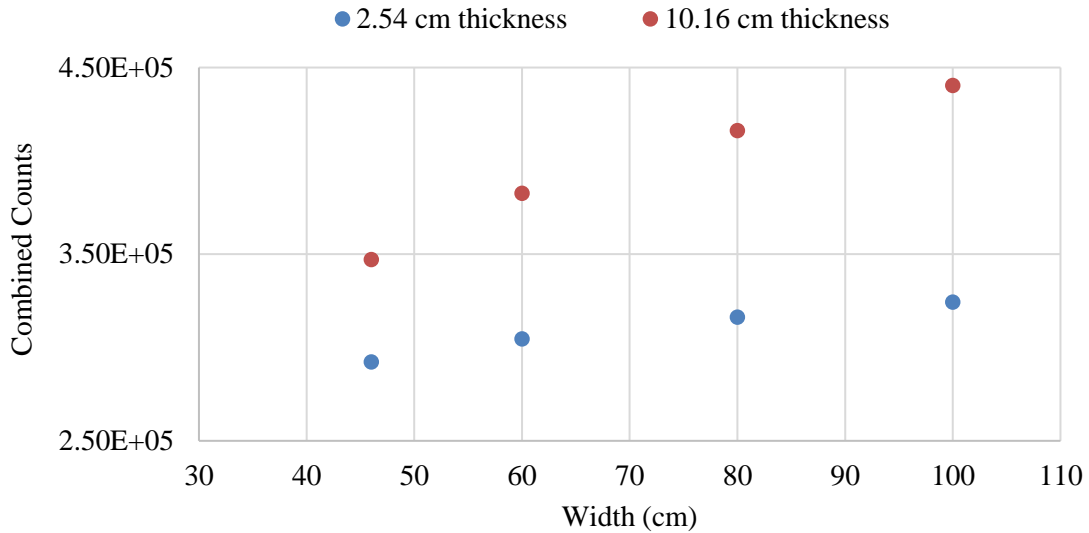


**Figure 9-10 Combined thermal neutron counts for 1-second measurement time as a function of concrete width for varied thicknesses**

Increasing the width further increases the likelihood of reflection, hence will increase the counts in the detectors. However, it increases the mass needed to be hoisted significantly. For the same width, a 2.54 cm thick concrete slab weighs 10.36 kg. MCNP simulations prove that for the 2.54 cm thick and 40 cm x 40 cm width, the  $\beta$  probabilities for all diversion scenarios are 0 with a 1 s measurement time. Thus, this configuration was used in the final setup for experiments.

In the likely event that the source strength and number of sources decrease, the measurement time needs to be increased to obtain statistically good results. A five-minute measurement time was considered good for a real time remote monitoring system.

## 9.2. Experiments at Texas A&M using $^{252}\text{Cf}$ as a Surrogate for SNF

A small-scale experiment was conducted using five  $^{252}\text{Cf}$  neutron sources. These sources were decay corrected to the day the experiments were conducted and the final neutron emission rates are shown in Table 9-3.

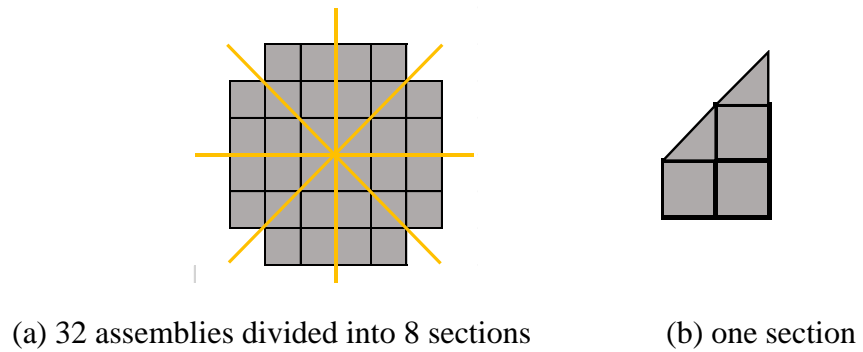
**Table 9-3  $^{252}\text{Cf}$  sources and neutron emission rates**

Source	Neutron emission (n.s <sup>-1</sup> )
1,2,3	5.11E+04
4,5	9.45E+02

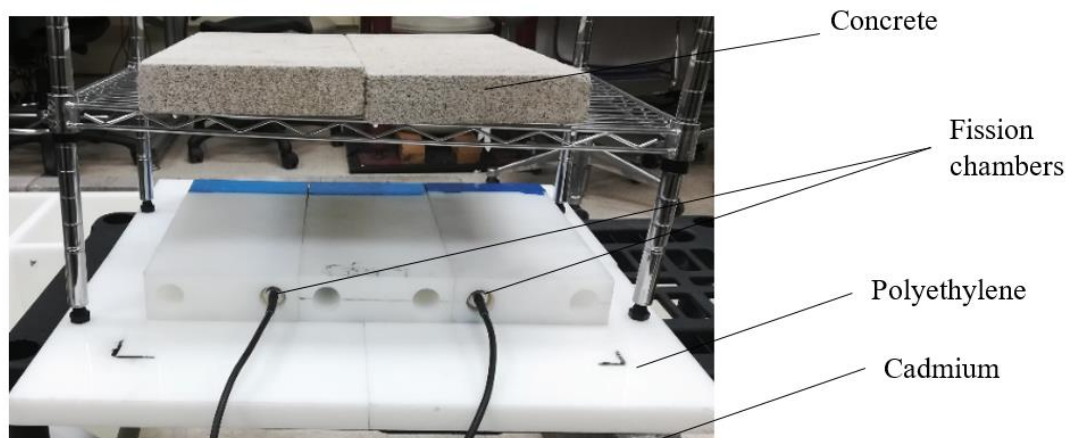
For the proof of concept experiments, five  $^{252}\text{Cf}$  sources representing 1/8 of a dry cask was used.

Figure 9-11 shows a representation of 32 assemblies in a dry cask. It is then divided into 8 sections by the yellow lines. Each section represents 1/8 of a dry cask with full assemblies and 2 half assemblies. Since one section consists 3 full assemblies and two half assemblies, the  $^{252}\text{Cf}$  sources present at Texas A&M were used to mimic this geometry. The  $^{252}\text{Cf}$  sources were surrounded with different reflecting material such that a point source was approximated as a surface source. Arranging those in a configuration to form ‘one section’ allowed for the assumption of symmetry to hold true. Sources 1-3 represent the 3 full assemblies while 4-5 represent the half assemblies. It is noted that

sources 4-5 are closer to  $1/3$  the source strength of sources 1-3. While they should be closer to  $1/2$ , these were the sources that were available to use at Texas A&M.



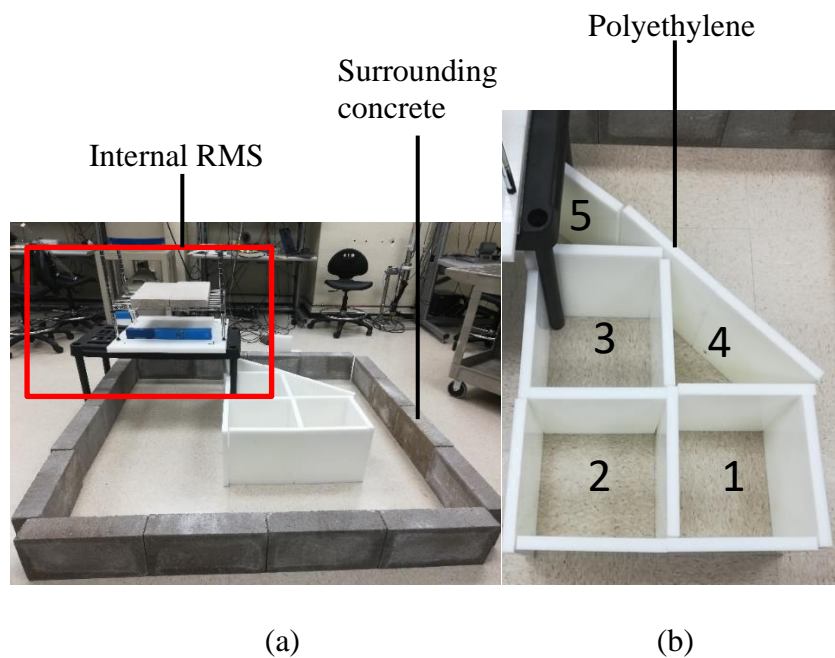
**Figure 9-11 (a) 32 assemblies divided into 8 sections such that each section is made up of (b) 3 full assemblies and 2 half assemblies represent one section which is  $1/8$  of a dry cask**



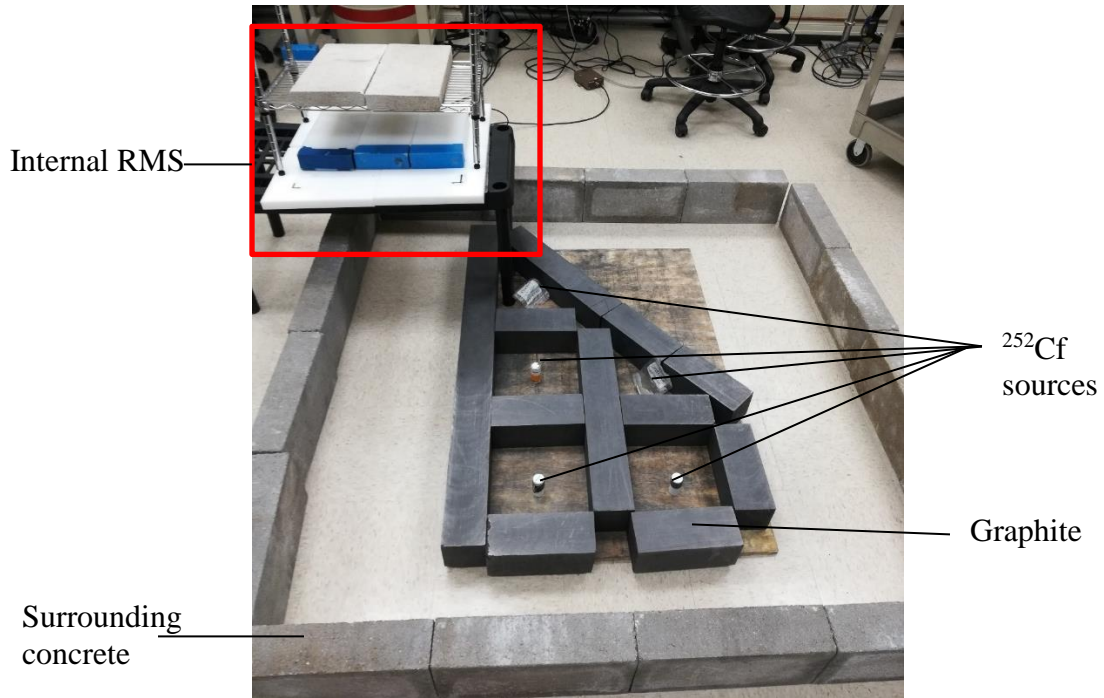
**Figure 9-12 Approximation of internal RMS with two fission chambers enveloped in polyethylene and cadmium with a concrete lid**

Figure 9-12 shows an approximation of the internal RMS while Figure 9-13 and Figure 9-14 show the experimental setup using polyethylene and graphite reflectors respectively as well as the location of the 5  $^{252}\text{Cf}$  sources.

From Figure 9-12, the internal RMS was recreated using fission chamber detectors that were surrounded by polyethylene and has a cadmium layer underneath the polyethylene. The fission chambers used were LND, Inc 30773 fission counters. On top of the RMS, concrete bricks representing the concrete lid of a dry cask were hoisted to incorporate the effect of reflection into the system. This was particularly important for the open lid case, DS0.



**Figure 9-13 Setup of experiments using polyethylene reflectors from the (a) side view and (b) top view where numbers present indicate the position of the  $^{252}\text{Cf}$  source**



**Figure 9-14 Setup of experiments using graphite reflectors**

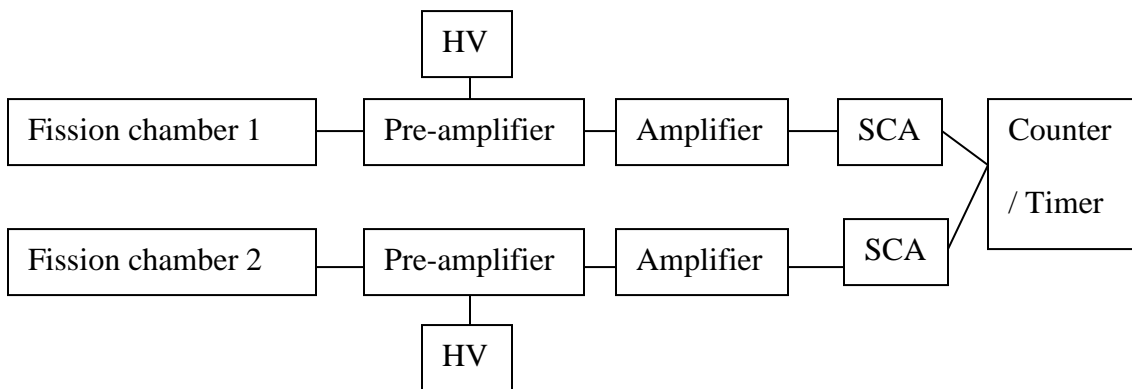
In Figure 9-13, the setup of the internal RMS relative to the position of the  $^{252}\text{Cf}$  sources is shown. Each polyethylene slab is 30.48 cm x 30.48 cm x 2.54 cm in such that when reflected, each box would represent a surface source that is 30.48 cm x 30.48 cm. This is slightly larger than the size of an assembly.

Figure 9-14 shows the same setup using graphite reflectors instead. Here, each piece of graphite has a different length but has a height and width of 4 in x 4 in. When the source is reflected by the surrounding graphite, a 24 cm x 24 cm square is formed to represent the dimensions of an assembly.

The surrounding concrete boundary represents the boundary present in a dry cask which is approximately 70 cm of concrete. In this case, the cinder blocks were 10.16 cm thick and were placed to increase reflections back into the system.

All the approximations made for the experiments that differ from the dimensions of a true dry cask are listed in Table 9-4.

The basic electronic configuration is shown in Figure 9-15 where each fission chamber detector is connected to a preamplifier, followed by an amplifier, to a single channel analyzer and finally to a counter/ timer.



**Figure 9-15 Basic electronic configuration for experiments**

**Table 9-4 Approximations made between experiment performed and MCNP simulations of internal RMS in dry cask storage. \* Length varied based on position**

<b>Parameter</b>	<b>Dry cask</b>	<b>Experiment</b>
<b>Source definition</b>		
Source Type	Spent Fuel	<sup>252</sup> Cf
Number of Sources	32 Assemblies	5 sources
Source Strength (ns <sup>-1</sup> )	1.52E+10	3.45E+05
Source Geometry	Volumetric	Point (surface when reflected)
<b>Fission chamber detector dimensions</b>		
Number of Detectors	2	2
Length (cm)	23	12.7
Radius (cm)	2.54	1.27
<b>Shielding for detector units</b>		
Polyethylene	46 x 46 x 8.35	(45.72 x 30.48 x 5.04) + (60.96 x 60.96 x 2.54)
Cadmium	46 x 46 x 0.05	46 x 46 x 0.05
<b>Dry cask environment</b>		
Lid concrete thickness (cm)	20	4.1275
Surrounding Concrete thickness (cm)	70	10.16
Stainless Steel thickness (cm)	24	0.16
Source to Stainless Steel distance (cm)	23	15.24
<b>Reflector dimensions</b>		
Graphite	N/A	4" x 4" x Length*
Polyethylene	N/A	1" x 12" x Length*

### 9.3. Results of Experiments

Using the experimental setup as shown in Figures 9-12, 9-13 and 9-14, the neutron counts recorded by each fission chamber detector was obtained for five minute counting time for the reference case (RS) with all neutron sources present, 5 diversion scenarios (DS1 through DS5 where each source was diverted one at a time) and the open lid case (DS0) where all sources are present but the concrete lid is open. A 15-minute background reading was also obtained, and the appropriate background neutron counts were subtracted for each experiment. Once the neutron count rates for each scenario were obtained, the minimum measurement time was determined by finding the least time required to get all  $\beta$  probabilities to less than 20%. The right detector,  $D_R$  is closer to the sources while the left detector,  $D_L$  is further away. Table 9-5 and Table 9-6 shows counts recorded by  $D_R$  and  $D_L$  and corresponding  $\beta$  probabilities,  $\beta_R$  and  $\beta_L$  using polyethylene reflected sources and graphite reflected sources for measurement times of 90 seconds and 220 seconds respectively.

For both reflector materials, all  $\beta$  probabilities for the various DS are below 20%. Increasing the measurement time will further drop the  $\beta$  probabilities.  $D_R$  is closer to the sources and always receives higher counts than  $D_L$ .

From Table 9-5, the trends between both detectors are the same where DS1, DS4 and DS0 are more challenging to detect than DS2 and DS3. Similar trends are seen using graphite reflectors in Table 9-6 where DS1 and DS4 are more challenging to detect than DS2 and DS3. However, DS0 is easily detectable than in the polyethylene case.

**Table 9-5 Neutron counts recorded by D<sub>1</sub> and D<sub>2</sub> for 90 seconds measurement time and corresponding  $\beta$  probabilities  $\beta_R$  and  $\beta_L$  using polyethylene reflected sources**

Diversion scenario	Counts		$\beta_R$ (%)	Counts		$\beta_L$ (%)
	D <sub>R</sub>	$\sigma_R$		D <sub>L</sub>	$\sigma_L$	
RS	119.7	10.9	-	110.4	10.5	-
DS1	89.4	9.5	9.7	78.6	8.9	5.1
DS2	67.2	8.2	0	45.9	6.8	0
DS3	66.3	8.1	0	53.1	7.3	0
DS4	92.4	9.6	16.7	84.6	9.2	17.7
DS5	93.0	9.6	18.0	77.7	8.8	4.0
DS0	93.3	9.7	19.2	84.6	9.2	17.7

Focusing on DS1 in both reflector material cases and using the positions of the sources from Figure 9-13 (b), DS1 is the source that is furthest away and shares a small solid angle with the detectors. In this case, D<sub>R</sub> sees a larger drop on counts than D<sub>L</sub> which makes it easier to distinguish whether a diversion has taken place or not. D<sub>L</sub> shares a larger solid angle with the source in position 1 and hence it is more sensitive to the change.

**Table 9-6 Neutron counts recorded by  $D_R$  and  $D_L$  for 220 seconds measurement time and corresponding  $\beta$  probabilities  $\beta_R$  and  $\beta_L$  using graphite reflected sources**

Diversio n scenario	Counts		$\beta_R$ (%)	Counts		$\beta_L$ (%)
	$D_R$	$\sigma_R$		$D_L$	$\sigma_L$	
RS	367	19.2	-	351	18.7	-
DS1	308	17.5	5.6	278	16.7	0.5
DS2	297	17.2	1.2	205	14.3	0.0
DS3	197	14.0	0.0	139	11.8	0.0
DS4	304	17.4	3.5	302	17.4	14.0
DS5	260	16.1	0.0	276	16.6	0.4
DS0	321	17.9	19.5	305	17.5	19.2

DS2 and DS3 are very easily detectable by both detectors and for both cases as the sources are closer to the detectors and resemble the sources that will be in the center of the cask, hence low  $\beta$  probabilities are expected.

DS4 and DS5 are the ‘half sources’ however in reality, their source strength is closer to 1/3 that of sources 1,2 and 3. In this case, DS5 is always easier to detect than DS4 as it is much closer to the detectors. DS4 is about equally as difficult to detect in both detectors regardless of reflector material as it is a weak source that shares a small solid angle with the detectors.

Finally, DS0 is the case where the concrete lid is open. In the dry cask simulations, the open concrete lid caused a large drop in flux (~ one order of magnitude)

seen by the detectors as there is no longer a medium to reflect and thermalize neutrons. In both reflector cases, a drop in counts is recorded for DS0 in the experiments, however, it is not the largest drop in counts as expected. Using polyethylene reflectors (Table 9-5) for both detectors, DS0 is a challenging case to detect. This may be because for the experiments, the 'lid' used only covered the width of the detectors encased in polyethylene as opposed to a large surface area present like that of a dry cask. Also, in the case of a dry cask, the largest fraction of neutrons that made it through the stainless steel MPC lid was in the fast energy range, >100 keV. These neutrons thermalized in the lid and are detected in the RMS. However, in this experiment, the neutrons are thermalized by the surrounding polyethylene before making it to the detectors. This is followed by further thermalization in the polyethylene surrounding the detectors which is thicker in the experiments than simulations due to availability. Hence, not as many neutrons reach the detectors and fewer than that are thermalized in the lid. This effect is less pronounced in the case with graphite reflectors. Since graphite thermalizes fast neutrons less than polyethylene, more fast neutrons reach the detectors and are reflected back into the system with the concrete lid present. Hence when the concrete lid is removed, a large drop in flux is noticed for the case with graphite reflectors than with polyethylene reflectors. Further, this is evident in lower  $\beta$  probabilities for DS0 in graphite versus polyethylene.

In general, it takes the graphite reflector case a measurement time of 220 seconds to reach the same  $\beta$  probabilities as the polyethylene case which took a measurement time of 90 seconds. Both materials work well for this experiment to smear the neutron

flux of a  $^{252}\text{Cf}$  source such that it looks like a surface source, however, as predicted, polyethylene serves as a better moderator than graphite.

These small-scale experiments prove that every single diversion is detectable with  $\beta$  probabilities less than 20% using a 5%  $\alpha$  for measurement times under four minutes. Hence, the internal RMS concept is a viable option for dry cask storages. Larger scale experiments using stronger and more sources would allow for better characterization of the system.

#### **9.4. MCNP Simulations of Final Experimental Setup**

MCNP simulations were performed using the same geometry of the experiments as shown in Figure 9-16. The results of the counts obtained in the detectors were retrieved using cell average flux tallies (F4) multiplied by source strength and detector sensitivities. The counts recorded by the detectors for the polyethylene and graphite reflected sources as well as the simulated counts are shown in Figures 9-17 and 9-18. The same with the associated  $\beta$  probabilities for simulations and experiments are shown in Tables 9-7 and 9-8. The counts recorded by the each fission chamber detector for the full case (RS) with all sources present, five diversion scenarios, DS1 through DS5 where each source was diverted one at a time (no replacement was made when a diversion occurred) and the open lid case, DS0 where all sources are present but the concrete lid is open are shown for the MCNP simulations. The minimum measurement time was determined by finding the least time required to get all  $\beta$  probabilities less than 20% for

$\alpha$  of 5%. The right detector,  $D_R$  is closer to the sources while the left detector,  $D_L$  is further away.

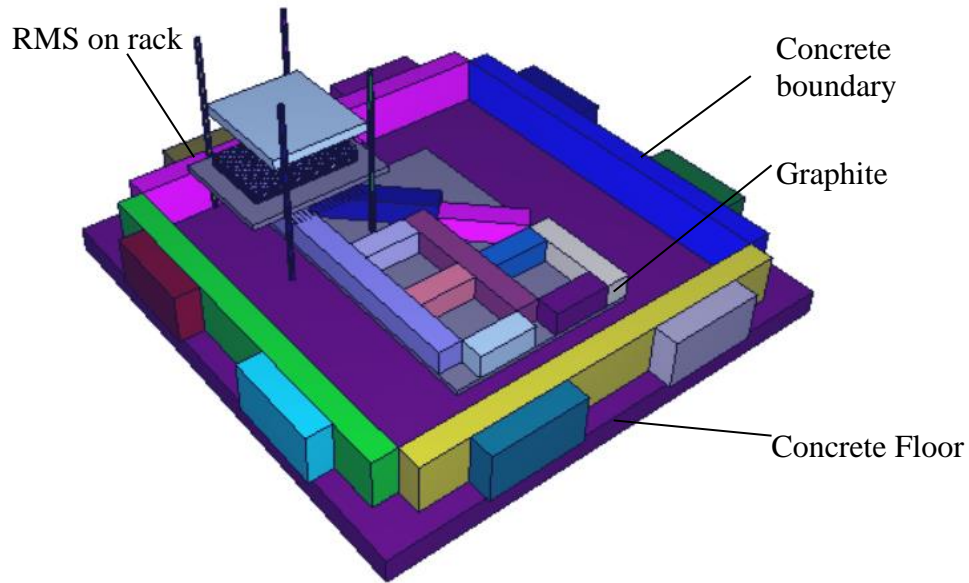


**Figure 9-16 VISED 3D rendering of experimental setup for the graphite reflected system**

From Figures 9-17 and 9-18, it is consistent across all DS and reflector materials that the measured counts through experiments are always higher than the simulated counts, but both follow the same trends. However, for most cases, the measured and simulated counts are within  $2\sigma$  uncertainty of each other, indicating that they can be considered statistically similar. In both reflector cases, the counts recorded by the right detector is higher than the left as it is closer to the sources and shares a larger solid angle with them which increases the probability of interactions with the detectors, hence higher counts. Additionally, the right detector measurement and simulations are all

within  $2\sigma$  uncertainty of each other with the exception of RS, DS0 and DS3 for both reflector materials. These three cases are the most significant when it comes to increase or decrease in counts. For instance, RS is the full case with maximum counts recorded while DS0 and DS3 are cases where the largest drop in counts happen for no source diversion (DS0) and source diversion (DS1).

Sources of error between measurement and simulations include presence of other radiation in the lab space that contribute to experimental counts but are absent in simulations, presence of more reflective surfaces in measurements versus simulations due to limited geometry of model (simulations only model pertinent parts of the experiment including the floor but does not include other features of the room like walls, furniture, etc.) that contribute to scatter and reflection of neutrons back into the system and human error associated with the experiment like placement of source within each square may vary between simulations. Additionally, the detectors modelled in MCNP only account for the declared active areas and conversion from thermal neutron flux to counts is done based on manufacturer provided sensitivities. While this is an acceptable procedure, all the neutrons interacting within the detectors are not necessarily below 0.025 eV. Rather, if a neutron between 0.026 eV - 0.5 eV interact within the detector, the sensitivity of interactions may be less than declared maximum sensitivity but still allows for counts to be registered. Hence, for these MCNP simulations the neutrons below 0.5 eV are considered thermal and included in the total counts detected.

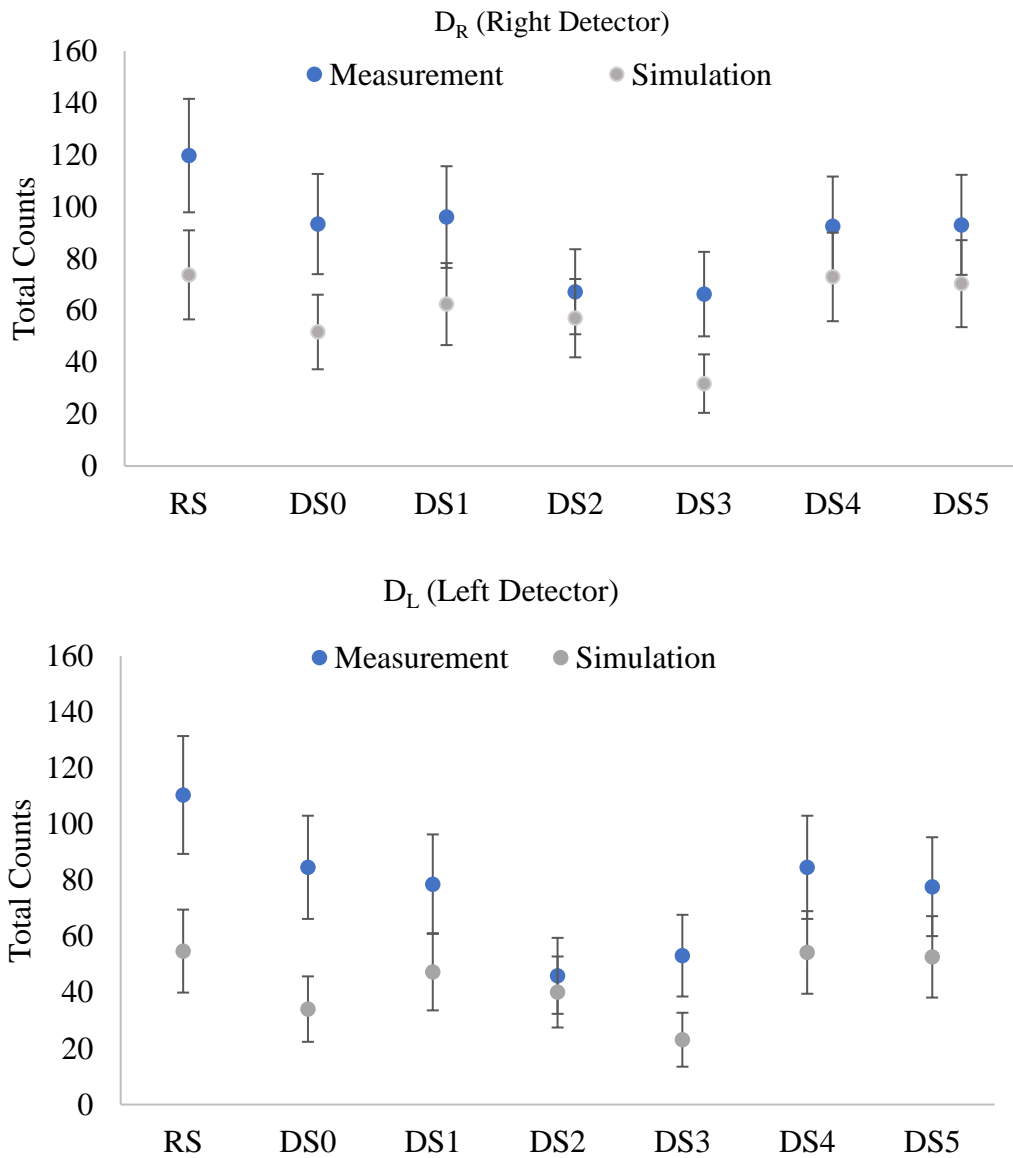


**Figure 9-17 Neutron counts with  $2\sigma$  uncertainties obtained in the left and right detectors using polyethylene reflectors for a measurement time of 90 seconds**

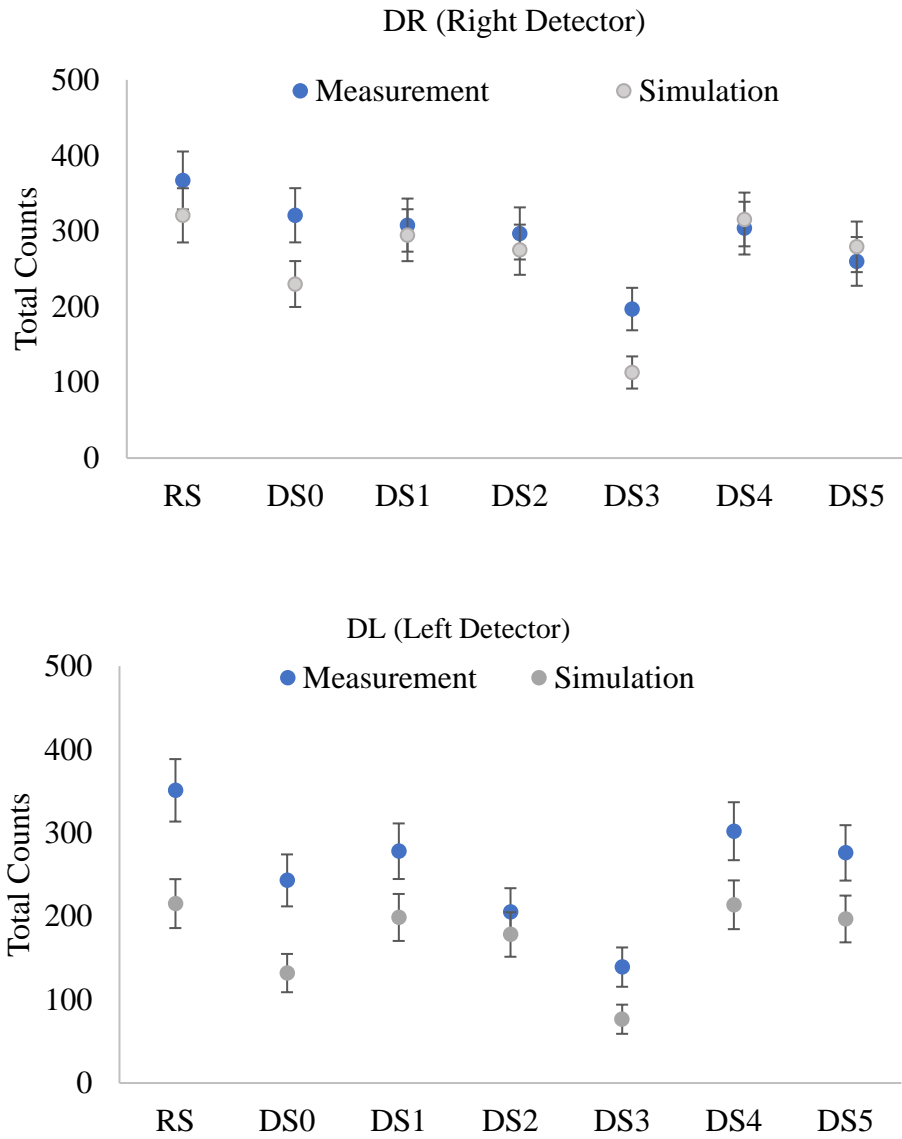


**Figure 9-18 Neutron counts with  $2\sigma$  uncertainties obtained in the left and right detectors using graphite reflectors for a measurement time of 220 seconds**

Focusing on the polyethylene reflected measurements in Table 9-7, the  $\beta$  probabilities calculated using the detected counts in MCNP simulations is higher than that obtained in the experiments. As mentioned previously, there are a number of reasons why the simulated and measured values are not more closely aligned, however, since  $\beta$  probabilities depend a lot on overlap between two gaussians, the mean and standard deviation of the counts obtained is crucial. Since the counts detected in simulations for the specified measured time is always lower than the measurement, the associated mean counts detected is also lower and when diversions occur, the drop in counts is less in simulation than measurements. Smaller differences between diversion scenarios account for larger overlap in the gaussian distributions and hence a larger  $\beta$  probability. From the simulations performed, in order to obtain  $\beta$  probabilities less than 20% for all DS (except DS4 and DS5), the proposed measurement time is ~ 9 minutes in the left detector and ~5 minutes in the right detector. DS4 and DS5 were the most challenging to detect and was considered unable to detect due to long measurement times (> 2 hours). However, when the experiment was performed, the count rates detected were higher than expected and proved that a 90 second measurement time was sufficient to obtain similar  $\beta$  probabilities and DS4 was detectable. This difference may be due to reflection and scatter of neutrons back into the system that is highly probable to the large concrete boundary, walls and lots of workstations present in the lab. Additionally, the fission chambers used may be more sensitive than declared which cause more counts to be detected.

**Table 9-7  $\beta$  probabilities (%) in the left and right detectors, comparing measurement neutron counts to MCNP simulation counts. These show values for the polyethylene reflected sources using a measurement time of 90 s and 5%  $\alpha$**

	<b>D<sub>R</sub></b>						<b>D<sub>L</sub></b>					
	<b>Measurement</b>	<b><math>\sigma</math></b>	<b><math>\beta</math></b>	<b>MCNP</b>	<b><math>\sigma</math></b>	<b><math>\beta</math></b>	<b>Measurement</b>	<b><math>\sigma</math></b>	<b><math>\beta</math></b>	<b>MCNP</b>	<b><math>\sigma</math></b>	<b><math>\beta</math></b>
RS	119.7	10.9	-	73.7	7.9	-	110.4	10.5	-	54.7	6.6	-
DS0	93.3	9.7	19.2	51.7	6.7	24.7	84.6	9.2	17.7	34.0	5.1	7.2
DS1	89.4	9.5	9.7	62.4	7.6	84.1	78.6	8.9	5.1	47.3	6.3	75.7
DS2	67.2	8.2	0.0	57.0	7.3	68.9	45.9	6.8	0.0	40.1	5.9	35.2
DS3	66.3	8.1	0.0	31.8	4.7	0	53.1	7.3	0.0	23.1	3.9	0.0
DS4	92.4	9.6	16.7	72.9	7.8	93.4	84.6	9.2	17.7	54.2	6.5	94.4
DS5	93.0	9.6	18.0	70.3	7.4	75.5	77.7	8.8	4.0	52.7	6.3	91.8

**Table 9-8  $\beta$  probabilities (%) in the left and right detectors, comparing measurement neutron counts to MCNP simulation counts. These show values for the graphite reflected sources using a measurement time of 220 s and 5%  $\alpha$**

	<b>D<sub>R</sub></b>						<b>D<sub>L</sub></b>					
	<b>Measurement</b>	<b><math>\sigma</math></b>	<b><math>\beta</math></b>	<b>MCNP</b>	<b><math>\sigma</math></b>	<b><math>\beta</math></b>	<b>Measurement</b>	<b><math>\sigma</math></b>	<b><math>\beta</math></b>	<b>MCNP</b>	<b><math>\sigma</math></b>	<b><math>\beta</math></b>
RS	367.4	19.2	-	320.9	17.9	-	351.3	18.7	-	215.2	14.7	-
DS0	320.5	17.9	19.5	230.1	15.2	0.0	305.1	17.5	19.2	131.8	11.5	0.0
DS1	308.0	17.5	5.6	294.7	17.2	57.4	277.6	16.7	0.5	198.6	14.1	70.3
DS2	297.0	17.2	1.2	275.5	16.6	16.8	205.3	14.3	0.0	178.1	13.3	16.6
DS3	196.5	14.0	0.0	113.1	10.6	0.0	139.3	11.8	0.0	76.5	8.7	0.0
DS4	304.3	17.4	3.5	315.5	17.8	91.2	301.7	17.4	14.0	213.8	14.6	94.0
DS5	260.3	16.1	0.0	279.3	16.7	23.4	275.7	16.6	0.4	196.7	14.0	65.8

In the graphite reflected case in Table 9-8, the same arguments can be used, however, the simulations indicated that a measurement time of ~1.5 hours for the right detector and ~2.5 hours for the left detector were needed to obtain all  $\beta$  probabilities less than 20%. DS4 was also considered not detectable due to the long measurement time required (>35 hours). In the experiment, all the  $\beta$  probabilities were less than 20% for a measurement time of 220 seconds. While the total counts detected in simulations and measurements are similar, the  $\beta$  probabilities are very different, thus leading to longer predicted measurement times.

The difference in simulations and experiments for a complete dry cask will be much less because of the following reasons:

1. The counting statistics obtained from a full dry cask will be much better (higher counts) due to higher neutron emissions. This will allow for better agreement of simulations and experiments. This is evident in the small-scale experiment performed, where the right detector count rates are higher than the left due to proximity to the sources, but that allowed for a better match of counts between the measurement and simulations.
2. In a complete dry cask system, the internal RMS is encased within the dry cask and there is lower probability of leakage and no scatter/reflection from the surrounding outside the dry cask that will contribute to the detectors as noticed in the small-scale experiments. The low efficiency design of the experiments due to limited resources allows for many external factors to contribute to the counts of the

detectors which are not captured in simulations, however, this is not the case with the dry cask system. The entirety of it is explicitly modelled and accounted for. Therefore, while the simulations called for longer measurement times to achieve similar  $\beta$  probabilities to the measurements, the total time required for an RMS to tell if the contents have been tampered with is still within acceptable limits. Hence, this proof-of-concept experiment verifies that the internal RMS is a good candidate to ensure CoK once a dry cask has been sealed.

## 10. EXTERNAL RMS MATERIAL STUDY

For the purpose of this dissertation, modelling of MSNDs was not done, instead void cells with realistic dimensions of the active area were used to represent the detectors in the external RMS model. All the results obtained for the external RMS up to this point employ realistic dimensions of the detector's active volume but are void of material. Each detector is fabricated as 0.05 cm thick with an active area of dimensions 2 cm x 2 cm [77] hence the model had the same dimensions.

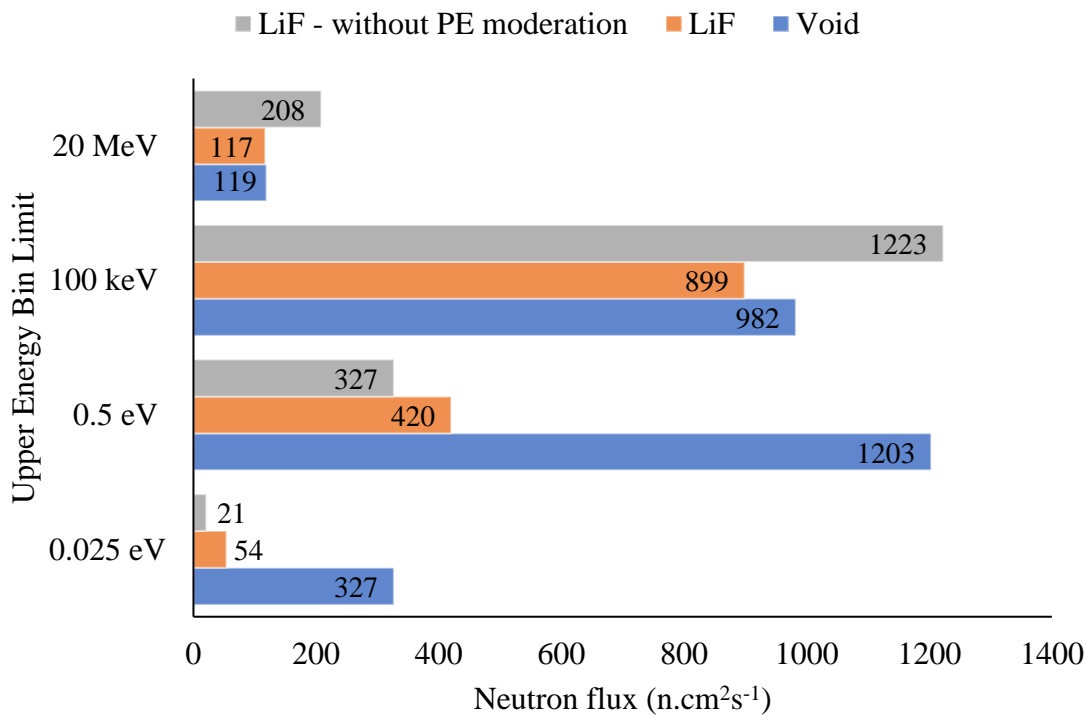
To better understand radiation interaction within the actual detector material, a second case is considered. In this case, the void detector volume was replaced with  ${}^6\text{LiF}$  with a density of  $0.892 \text{ g. cm}^{-3}$  to represent the material used in MSNDs. This density was reflective of the packing fraction of LiF within the detectors [80]. However, the trenches, microcavities, silicon packing and support structure were not modelled. The difference in neutron fluxes obtained between the first case (with void detector cells) and the second case (with  ${}^6\text{LiF}$  detector cells) will provide insight to the self-attenuating properties of the detector and RMS capabilities for detection of DSs.

Figure 10-1 shows the energy discriminated neutron flux ( $\text{n.cm}^{-2}\text{s}^{-1}$ ) observed by the external RMS for detector cells made of void and  ${}^6\text{LiF}$  in the cases mentioned above.

The neutron flux in the thermal bin ( $<0.025 \text{ eV}$ ) is attenuated by 84% due to the presence of LiF. The thickness of the LiF in the detector is 0.5 mm which represents approximately 3 mean free paths of thermal neutrons (MSND thicknesses were

optimized to ensure maximum energy deposition within the detectors by the manufacturers).

However, when using LiF, the thermal bin only contributes 4% to the total neutron flux while the 100 keV (intermediate energy) bin contributed 60%. Hence, adding more polyethylene moderation may thermalize these neutrons to the energy range of interest and increase the thermal neutron flux recorded by the detectors.



**Figure 10-1 Neutron flux observed by external cask detector for void and LiF detector materials**

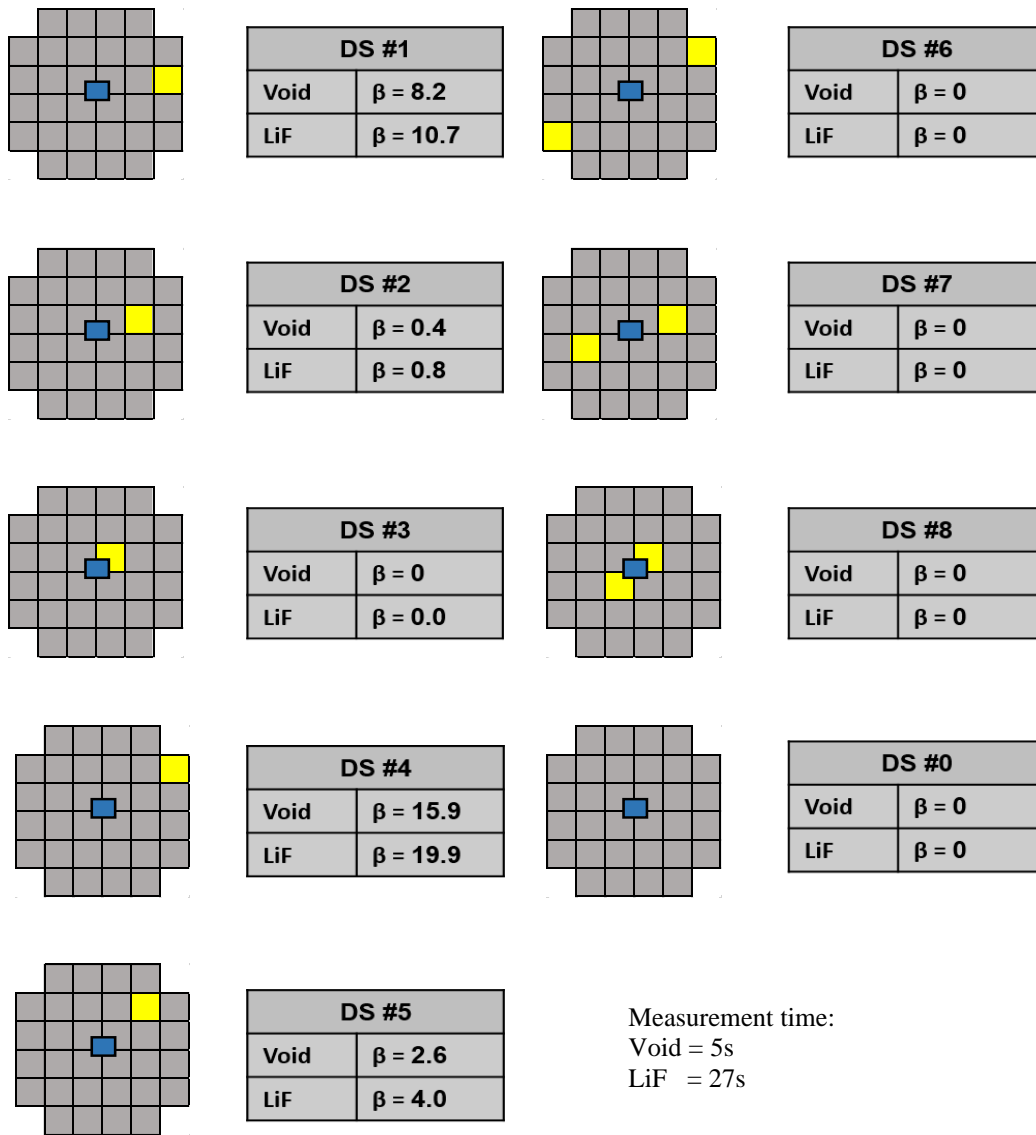
### 10.1. Effect of LiF Material in the External RMS for Homogenous Assemblies

Figure 10-2 show the  $\beta$  probabilities (%) of the 8 diversion scenarios and open lid scenario (DS0) using LiF and void as materials in the detector array of the external RMS. The blue box in the center represents the position of the external RMS detector. The yellow square designates position of diverted SNF assemblies that have been replaced with a dummy assembly and  $\alpha$  is the false alarm probability (%).  $\beta$  probabilities for all diversion scenarios are calculated for 5%  $\alpha$  thresholds. The measurement time is determined by finding the time that corresponds to the first instance that all the  $\beta$  probabilities for all SNF assembly diversion scenarios is less than 20%.

When using LiF as the detector material, the external RMS takes 27 seconds to ensure all  $\beta$  probabilities for all DS are under 20%. This is well under the initial criteria of having the measurement time under 5 minutes. The two challenging DSs are DS1 and DS4 which are the peripheral assembly diversions that contribute less to the detector. The rest of the single assembly diversions achieve  $\beta$  probabilities less than 20% within 15 seconds of measurement time. As the SNF assembly diversions happen closer to the center of the cask, where the detectors are positioned, the  $\beta$  probability decreases significantly as it becomes easier to detect the diversion (and substitution) of the assemblies. Two assembly diversions (DS 6 through DS 8) and the open lid scenario (DS0) provide large drops in thermal neutron flux and hence they are detectable with  $\beta$  probabilities less than 20% within 6 seconds.

As a comparison, when the detector was void of material, the measurement time for all DS to achieve  $\beta$  probabilities less than 20% was 5 seconds. However, in this case

with LiF, a longer measurement time is needed to ensure the detector records sufficient counts for good counting statistics due to the attenuation of neutrons within the LiF material which decreases the thermal neutron flux observed by the external RMS.



**Figure 10-2  $\beta$  probabilities (%) for the external RMS using LiF and void detector materials**

## 10.2. Effect of LiF Material in External RMS on Heterogenous Loading Patterns

Figure 10-3 shows the percentage contributions of each assembly to the thermal neutron flux recorded by the external RMS detectors and the corresponding  $\beta$  probabilities for all diversion scenarios. The measurement time is the minimum time needed by both detectors in the internal RMS to achieve  $\beta$  probabilities less than 20%. All scenarios used a 5%  $\alpha$  threshold. In general, the external RMS takes a longer measurement time with LiF compared to void (~130 -190 seconds vs. ~10 seconds) to provide similar results. The longer measurement time is needed to achieve good counting statistics due to the reduction in thermal neutron flux record in the detectors. This is because of the attenuation of neutrons within the detector material and the need to re-optimize the polyethylene moderation surrounding it. However, even without re-optimization of polyethylene, the external RMS is able to verify all DSs within ~3 minutes which meets the measurement time criteria of being under 5 minutes.

From Figure 10-3, the assembly diversion scenarios that are challenging to detect are the assemblies that are cool and in the periphery of the cask. Diversion scenarios that have  $\beta$  probabilities more than 15% are depicted by the black boxes. In all cases, each of these assemblies contributed less than 2.3% to the detectors in the external RMS. The central assembly diversions are easily detectable ( $\beta$  probability <10%) within 45 seconds of measurement time.

**Loading Pattern 1**

**t = 139 s**

	29	30	31	32	
	2	2.3	2.4	2.1	
	19.9	9.9	9.2	17.0	
23	24	25	26	27	28
2	3.2	3.8	3.9	3.3	3.3
19.1	0.7	0.0	0.0	0.5	0.8
17	18	19	20	21	22
2.9	3.8	4.6	3.9	3.3	2.8
2.1	0.0	0.0	0.0	0.5	2.8
11	12	13	14	15	16
2.9	3.3	4.7	4.5	3.4	3
2.1	0.4	0.0	0.0	0.4	2.0
5	6	7	8	9	10
2.5	3.5	3.3	3.2	3.5	2.6
6.2	0.3	0.4	0.8	0.2	6.4
	1	2	3	4	
	2.5	3	3.1	2.8	
	6.5	1.8	1.2	3.8	

**Loading Pattern 2**

**t = 165 s**

	29	30	31	32	
	2.74	3.15	3.21	2.73	
	4.4	1.2	1.0	4.4	
23	24	25	26	27	28
2.17	2.91	2.33	2.29	2.95	2.05
15.1	2.5	10.2	11.5	2.2	19.9
17	18	19	20	21	22
2.63	2.3	2.8	2.79	2.39	2.67
5.5	11.0	2.9	3.0	8.9	4.9
11	12	13	14	15	16
2.97	2.31	4.75	6.27	3.64	3.09
2.3	11.0	0.0	0.0	0.2	1.7
5	6	7	8	9	10
2.72	4.4	3.62	3.61	4.46	3.33
4.4	0.0	0.2	0.2	0.0	0.8
	1	2	3	4	
	2.89	2.09	4.58	2.99	
	2.9	18.7	0.0	2.3	

**Loading Pattern 3**

**t = 191 s**

	29	30	31	32	
	2.07	2.2	1.98	1.59	
	14.7	6.5	7.1	14.4	
23	24	25	26	27	28
2.3	2.91	4.06	3.61	3.45	2.35
13.1	2.1	0.0	0.0	0.0	0.4
17	18	19	20	21	22
2.55	4.81	5.07	4.43	3.45	1.62
8.9	0.0	0.0	0.0	0.0	7.4
11	12	13	14	15	16
2.65	4.72	5.34	4.99	2.5	2.53
7.1	0.0	0.0	0.0	0.2	0.1
5	6	7	8	9	10
3.56	4.38	3.18	2.83	3.43	2.35
0.4	0.0	0.2	0.2	0.0	0.4
	1	2	3	4	
	1.91	2.08	2.5	2.44	
	19.9	9.5	1.1	0.6	

**Figure 10-3 Three loading patterns where the top to bottom numbers are the assembly number, assembly contributions (%) to the detectors in the external RMS and the  $\beta$  probability (%) for the particular assembly diversion.**

In conclusion, the presence of LiF attenuates the thermal neutron flux recorded within the detectors in the external RMS by 82%. This causes the measurement time needed to achieve good counting statistics to ensure  $\beta$  probabilities  $<20\%$  to be  $\sim 3$  minutes (vs. 30 seconds for void case). This measurement time is within the initially set criteria of being under 5 minutes and proves that the external RMS concept is viable.

Future work for this portion includes detailed modelling of the trench design within MSND and the silicon material surrounding them. Also, the density of LiF is dependent on its packing factor, hence, a wider literature review and array of simulations should be performed to see how various densities of materials affect the signal recorded by the external RMS.

## 11. CONCLUSIONS

Current practices in nuclear safeguards for maintaining continuity of knowledge (CoK) of spent nuclear fuel (SNF) assemblies stored in dry casks are inadequate. Hence, in the event of a loss of CoK, the required reverification of SNF assemblies in dry casks will be cumbersome, expensive and time consuming. The main objective of the dissertation study was to find a better solution to this problem of maintaining CoK of SNF stored in dry casks and to timely detect the diversion of a single SNF assembly from the dry cask.

The study included the design of two types of remote monitoring systems (RMS) which detect neutron signal from SNF. The first RMS design (internal to the cask) utilized fission chamber neutron detectors while the second design (external to the cask) utilized micro-structured semi-conductor neutron detectors (MSND). The detectors in both designs were surrounded by neutron moderating materials in specific configurations that optimized counting efficiencies for each RMS. The RMS design development involved elaborate simulation studies using a Monte Carlo radiation transport code (MCNP), proof-of-concept neutron measurement experiments for the internal RMS and analyses. Separate studies were conducted for each RMS design integrated with the dry cask simulation model.

The study concluded that both internal and external RMS designs are suitable for maintaining CoK and able to timely detect diversion of a single SNF assembly. For the SNF assembly/assemblies diversion scenarios analyzed, the false alarm probability was

set at 5% of the reference scenario (no diversions) and the corresponding non-detection probabilities,  $\beta$  calculated were found to be less than 20% that meets the criteria set by the International Atomic Energy Agency. The cost of the internal RMS and external RMS is estimated at \$14,000 and \$5,000 respectively. The details of the cost of each RMS is provided in Appendix F.

Additionally, the simulations performed using both RMS designs with heterogenous loading patterns provided insight to arrangements of SNF based on neutron emission rates that aid with monitoring from a safeguards perspective. This is essential to ensure  $\beta$  probabilities are kept less than 20% for any assembly diversions.

In conclusion, the proposed RMS designs are compact and cost effective as well as integrable with existing dry cask designs. The choice of detectors and shielding material ensure robustness of the system and simple operation procedure due to easy analysis using gross neutron counts. All the simulations and experiments performed further support RMS capabilities to fulfill IAEA requirements. As a vital portion of information driven safeguards and safeguards by design, the concepts of RMSs should be integrated into future dry cask designs. This integration can ensure the continuous verification of SNF assemblies in dry cask storages and support facility safeguards.

### **11.1. Future work**

The internal RMS design validation experiments should be conducted with strong  $^{252}\text{Cf}$  sources. A robust prototype of the internal RMS design should be manufactured for further field testing.

The external RMS on the other hand was a conceptual development, hence making detailed models of the trench design within MSNDs and the silicon material surrounding them is the next step. Also, the density of LiF used in MSNDs is dependent on its packing factor, hence, a wider literature review and array of simulations should be performed to see how various densities of materials affect the signal recorded by the external RMS.

In addition, procuring MSNDs and testing them with neutron sources will further validate its use in nuclear safeguards application to detect SNF assembly diversion. Finally, the number of detectors proposed for this work was the minimum required to low  $\beta$  probabilities in the various diversion scenarios. If more detectors could be used, other arrangements that particularly focus on placing the detectors on the periphery of the cask lid, in addition to the center should be tested. This is because, the most challenging assembly diversions to detect are those of cool assemblies in the periphery of the cask. Hence, strategically placing an optimized number of detectors to detect peripheral assembly diversions will be a fruitful exercise

Further work includes developing the electronics needed to sustain the power and remote transmission of data from both RMS designs.

Finally, further MCNP simulations with different cask designs and other SNF assemblies from boiling water reactors (BWR), Canada deuterium uranium (CANDU), fast breeder reactor (FBR), molten salt reactor (MSR) and more can be simulated and tested for usefulness in the future. This study considered only dry casks stored with pressurized water reactor (PWR) SNF assemblies.

## REFEFENCES

- [1] POWER, Dry Cask Storage Booming for Spent Nuclear Fuel, POWER Magazine. (2015). <https://www.powermag.com/dry-cask-storage-booming-for-spent-nuclear-fuel/> (accessed May 9, 2020).
- [2] Shippingport NuclearPower Station, (n.d.). /About-ASME/Engineering-History/Landmarks/47-Shippingport-Nuclear-Power-Station (accessed February 15, 2020).
- [3] J.D. Werner, U.S. Spent Nuclear Fuel Storage, (n.d.) 57.
- [4] NRC: Spent Fuel Storage in Pools and Dry Casks - Key Points and Questions & Answers, (n.d.). <https://www.nrc.gov/waste/spent-fuel-storage/faqs.html> (accessed February 15, 2020).
- [5] NRC: Dry Cask Storage, (n.d.). <https://www.nrc.gov/waste/spent-fuel-storage/dry-cask-storage.html> (accessed February 15, 2020).
- [6] A. Fattah, N. Khlebnikov, International safeguards aspects of spent-fuel disposal in permanent geological repositories, IAEA BULLETIN. (n.d.) 5.
- [7] Enhancing and Optimizing Safeguards Implementation by Remote, Studylib.Net. (n.d.). <https://studylib.net/doc/18753427/enhancing-and-optimizing-safeguards-implementation-by-remote> (accessed February 15, 2020).
- [8] I. Harkness, T. Zhu, Y. Liang, E. Rauch, A. Enqvist, K.A. Jordan, Development of Neutron Energy Spectral Signatures for Passive Monitoring of Spent Nuclear Fuels in Dry Cask Storage, EPJ Web Conf. 170 (2018) 07004. <https://doi.org/10.1051/epjconf/201817007004>.
- [9] NRC: Pressurized Water Reactors, (n.d.). <https://www.nrc.gov/reactors/pwrs.html> (accessed February 15, 2020).
- [10] J.J. Duderstadt, L.J. Hamilton, Nuclear Reactor Analysis, Wiley, 1976. <https://books.google.com/books?id=R057QgAACAAJ>.
- [11] Nuclear Fuel Cycle Overview - World Nuclear Association, (n.d.). <https://www.world-nuclear.org/information-library/nuclear-fuel-cycle/introduction/nuclear-fuel-cycle-overview.aspx> (accessed February 15, 2020).

- [12] U.S.G.A. Office, Disposal of High-Level Nuclear Waste, (n.d.). <http://www.gao.gov/disposal-high-level-nuclear-waste> (accessed February 15, 2020).
- [13] L.N. Larson, Nuclear Waste Storage Sites in the United States, (n.d.) 2.
- [14] Reprocessing plants, world-wide, ENS. (n.d.). <https://www.euronuclear.org/glossary/reprocessing-plants-world-wide/> (accessed February 15, 2020).
- [15] The use of scientific and technical results from underground research laboratory investigations for the geological disposal of radioactive waste, (n.d.). [https://www-pub.iaea.org/MTCD/publications/PDF/te\\_1243\\_prn.pdf](https://www-pub.iaea.org/MTCD/publications/PDF/te_1243_prn.pdf) (accessed February 15, 2020).
- [16] Nuclear Reactors | Nuclear Power Plant | Nuclear Reactor Technology - World Nuclear Association, (n.d.). <https://www.world-nuclear.org/information-library/nuclear-fuel-cycle/nuclear-power-reactors/nuclear-power-reactors.aspx> (accessed February 15, 2020).
- [17] J.R. Phillips, Irradiated Fuel Measurements, (n.d.) 34.
- [18] INFCIRC/153(Corrected) - The Structure and Content of Agreements Between the Agency and States Required in Connection with the Treaty on the Non-Proliferation of Nuclear Weapons, (n.d.) 34.
- [19] Safeguards in practice, (2016). <https://www.iaea.org/topics/safeguards-in-practice> (accessed February 15, 2020).
- [20] [iaea\\_safeguards\\_glossary.pdf](https://www.iaea.org/sites/default/files/iaea_safeguards_glossary.pdf), (n.d.). [https://www.iaea.org/sites/default/files/iaea\\_safeguards\\_glossary.pdf](https://www.iaea.org/sites/default/files/iaea_safeguards_glossary.pdf) (accessed February 15, 2020).
- [21] The Present Status of IAEA Safeguards on Nuclear Fuel Cycle Facilities, (n.d.). [https://www.iaea.org/sites/default/files/publications/magazines/bulletin/bull22-3/223\\_403400240.pdf](https://www.iaea.org/sites/default/files/publications/magazines/bulletin/bull22-3/223_403400240.pdf) (accessed February 15, 2020).
- [22] K. Ziock, P. Vanier, L. Forman, G. Caffrey, J. Wharton, A. Lebrun, The Feasibility of Cask “Fingerprinting” as a Spent-Fuel, Dry-Storage Cask Safeguards Technique, (2020). <https://doi.org/10.2172/881660>.
- [23] C.J. Wharton, E.H. Seabury, A.J. Caffrey, P.L. Winston, Summary Report: INL CDCIS Cask Scanner Testing at Doel, Belgium, (n.d.) 26.

- [24] M. Österlund, J. Blomgren, J. Donnard, A. Flodin, J. Gustafsson, M. Hayashi, P. Mermod, L. Nilsson, S. Pomp, L. Wallin, A. Öhrn, A. Prokofiev, TOMOGRAPHY OF CANISTERS FOR SPENT NUCLEAR FUEL, (2006).
- [25] G. Jonkmans, V. Anghel, C. Jewett, M. Thompson, Nuclear Waste Imaging and Spent Fuel Verification by Muon Tomography, *Annals of Nuclear Energy*. 53 (2012). <https://doi.org/10.1016/j.anucene.2012.09.011>.
- [26] F. Ambrosino, L. Bonechi, L. Cimmino, R. D'Alessandro, D.G. Ireland, R. Kaiser, D.F. Mahon, N. Mori, P. Noli, G. Saracino, C. Shearer, L. Viliiani, G. Yang, Assessing the feasibility of interrogating nuclear waste storage silos using cosmic-ray muons, *J. Inst.* 10 (2015) T06005–T06005. <https://doi.org/10.1088/1748-0221/10/06/T06005>.
- [27] A. Clarkson, D.J. Hamilton, M. Hoek, D.G. Ireland, J.R. Johnstone, R. Kaiser, T. Keri, S. Lumsden, D.F. Mahon, B. McKinnon, M. Murray, S. Nutbeam-Tuffs, C. Shearer, C. Staines, G. Yang, C. Zimmerman, The design and performance of a scintillating-fibre tracker for the cosmic-ray muon tomography of legacy nuclear waste containers, *Nuclear Instruments and Methods in Physics Research Section A: Accelerators, Spectrometers, Detectors and Associated Equipment*. 745 (2014) 138–149. <https://doi.org/10.1016/j.nima.2014.01.062>.
- [28] S. Chatzidakis, P. Forsberg, B. Sims, L. Tsoukalas, Monte Carlo Simulations of Cosmic Ray Muons for Dry Cask Monitoring, in: 2015.
- [29] J.M. Durham, E. Guardincerri, C.L. Morris, D. Poulson, J.D. Bacon, D. Chichester, J. Fabritius, S. Fellows, K. Plaud, D. Morley, P. Winston, Cosmic Ray Muon Imaging of Spent Nuclear Fuel in Dry Storage Casks, (n.d.) 14.
- [30] D. Poulson, J.M. Durham, E. Guardincerri, C.L. Morris, J.D. Bacon, K. Plaud-Ramos, D. Morley, A.A. Hecht, Cosmic ray muon computed tomography of spent nuclear fuel in dry storage casks, *Nuclear Instruments and Methods in Physics Research Section A: Accelerators, Spectrometers, Detectors and Associated Equipment*. 842 (2017) 48–53. <https://doi.org/10.1016/j.nima.2016.10.040>.
- [31] A. Rimpler, Bonner sphere neutron spectrometry at spent fuel casks, *Nuclear Instruments and Methods in Physics Research Section A: Accelerators, Spectrometers, Detectors and Associated Equipment*. 476 (2002) 468–473. [https://doi.org/10.1016/S0168-9002\(01\)01492-9](https://doi.org/10.1016/S0168-9002(01)01492-9).
- [32] P.A. Santi, M.C. Browne, C.R. Freeman, R.F. Parker, R.B. Williams, Initial measurements of BN-350 spent fuel in dry storage casks using the dual slab verification detonator, Los Alamos National Lab. (LANL), Los Alamos, NM (United States), 2010. <https://www.osti.gov/biblio/1017486-initial-measurements->

- bn-spent-fuel-dry-storage-casks-using-dual-slab-verification-detonator (accessed February 16, 2020).
- [33] I. Harkness, SAFEGUARDS APPROACHES FOR SPENT NUCLEAR FUEL IN DRY CASK STORAGE, (2018).
- [34] C.J. Werner, MCNP Users Manual - Code Version 6.2, (2017). [https://laws.lanl.gov/vhosts/mcnp.lanl.gov/pdf\\_files/la-ur-17-29981.pdf](https://laws.lanl.gov/vhosts/mcnp.lanl.gov/pdf_files/la-ur-17-29981.pdf) (accessed February 23, 2020).
- [35] R.D. Mosteller, VALIDATION SUITES FOR mcnp<sup>tm</sup>, (n.d.) 10.
- [36] Holtec International, Holtec International Final Safety Analysis Report for the HI-STORM 100 Cask System, (n.d.). <https://www.nrc.gov/docs/ML1613/ML16138A100.pdf> (accessed February 16, 2020).
- [37] R. Kelly, P. Tsvetkov, S. Chirayath, J. Poston, E. Kitcher, Uncertainty Quantification of Concrete Utilized in Dry Cask Storage, Nuclear Technology. 190 (2015) 72–87. <https://doi.org/10.13182/NT13-155>.
- [38] R. Kelly, Uncertainty Quantification of Concrete Utilized in Dry Cask Storage, Texas A&M University, 2013.
- [39] W. Marshall, J. Wagner, Impact of Fuel Failure on Criticality Safety of Used Nuclear Fuel, (2012).
- [40] R.P. Kelly, Uncertainty Quantification of Concrete Utilized in Dry Cask Storage, Thesis, 2013. <https://oaktrust.library.tamu.edu/handle/1969.1/158896> (accessed February 19, 2020).
- [41] Oak Ridge National Laboratory, Isotope Generation and Depletion Code Matrix Exponential Method., (n.d.).
- [42] Khudoleeva-Thesis-2013.pdf, (n.d.). <https://oaktrust.library.tamu.edu/bitstream/handle/1969.1/158895/KHUDOLEEVA-THESIS-2013.pdf?sequence=1> (accessed January 31, 2020).
- [43] A. Sagadevan, S. Chirayath, Information driven safeguards approach for remote monitoring system of dry cask storage, Nuclear Instruments and Methods in Physics Research Section A: Accelerators, Spectrometers, Detectors and Associated Equipment. 954 (2020) 161737. <https://doi.org/10.1016/j.nima.2018.12.052>.

- [44] D.G. Cacuci, Handbook of Nuclear Engineering: Vol. 1: Nuclear Engineering Fundamentals; Vol. 2: Reactor Design; Vol. 3: Reactor Analysis; Vol. 4: Reactors of Generations III and IV; Vol. 5: Fuel Cycles, Decommissioning, Waste Disposal and Safeguards, Springer Science & Business Media, 2010.
- [45] A. Lafleur, Development of Self-Interrogation Neutron Resonance Densitometry (SINRD) to Measure the Fissile Content in Nuclear Fuel, Thesis, 2011. <https://oaktrust.library.tamu.edu/handle/1969.1/ETD-TAMU-2011-08-9685> (accessed March 23, 2020).
- [46] J. Fan, Force collision and next event estimation of pulse height tallies, *Sci China Ser E.* 46 (2003) 271. <https://doi.org/10.1360/03ye9029>.
- [47] X-5 Monte Carlo Team, MCNP — A General Monte Carlo N-Particle Transport Code, Version 5 Volume I: Overview and Theory, (n.d.). [https://mcnp.lanl.gov/pdf\\_files/la-ur-03-1987.pdf](https://mcnp.lanl.gov/pdf_files/la-ur-03-1987.pdf) (accessed March 23, 2020).
- [48] Excel NORMINV Function, (n.d.). <https://www.excelfunctions.net/excel-norminv-function.html> (accessed February 5, 2020).
- [49] NORMDIST function, (n.d.). <https://support.office.com/en-us/article/normdist-function-126db625-c53e-4591-9a22-c9ff422d6d58> (accessed February 5, 2020).
- [50] W.H. Geist, IAEA Sampling Plan, 2017. <https://doi.org/10.2172/1392849>.
- [51] NRC: Glossary -- Neutron flux, (n.d.). <https://www.nrc.gov/reading-rm/basic-ref/glossary/neutron-flux.html> (accessed February 29, 2020).
- [52] A. Khudoleeva, Conceptual Development of Remote Monitoring System for PWR Spent Fuel Dry Cask Storage through Neutron and Gamma Transport Simulations, Texas AM University, 2013.
- [53] A.P. Khudoleeva, S.S. Chirayath, W.S. Charlton, CONCEPTUAL Development Of A Remote Monitoring System For Safeguarding Of Dry Cask Storage Facilities, (n.d.) 10.
- [54] C. Greulich, C. Hughes, Y. Gao, A. Enqvist, J. Baciak, High energy neutron transmission analysis of dry cask storage, *Nuclear Instruments and Methods in Physics Research Section A: Accelerators, Spectrometers, Detectors and Associated Equipment.* 874 (2017) 5–11. <https://doi.org/10.1016/j.nima.2017.08.014>.
- [55] J.-H. Ko, J.-H. Park, I.-S. Jung, G.-U. Lee, C.-Y. Baeg, T.-M. Kim, Shielding Analysis Of Dual Purpose Casks For Spent Nuclear Fuel Under Normal Storage

Conditions, *Nuclear Engineering and Technology*. 46 (2014) 547–556.  
<https://doi.org/10.5516/NET.08.2013.039>.

- [56] Dry Cask Storage FAQ.pdf, (n.d.).  
<http://www.safesecurevital.com/pdf/Dry%20Cask%20Storage%20FAQ.pdf>  
(accessed February 23, 2020).
- [57] NRC: Spent Fuel Storage Licensing, (n.d.). <https://www.nrc.gov/waste/spent-fuel-storage/licensing.html> (accessed February 23, 2020).
- [58] E.B. Rauch, Signatures of Extended Storage of Used Nuclear Fuel Comprehensive Final Report, 2016. <https://doi.org/10.2172/1327981>.
- [59] Fission Chamber - Wide Range Detectors, Nuclear Power. (n.d.).  
<https://www.nuclear-power.net/nuclear-power-plant/nuclear-reactor/nuclear-instrumentation/excore-nuclear-instrumentation/fission-chamber-wide-range-detectors/> (accessed February 29, 2020).
- [60] A.M. Lafleur, W.S. Charlton, H.O. Menlove, M.T. Swinhoe, A.R. Lebrun, Development of Self-Interrogation Neutron Resonance Densitometry to Improve Detection of Possible Diversions for PWR Spent Fuel Assemblies, *Nuclear Technology*. 181 (2013) 354–370. <https://doi.org/10.13182/NT13-A15790>.
- [61] A.C. Trahan, Utilization of the Differential Die-Away Self-Interrogation Technique for Characterization and Verification of Spent Nuclear Fuel, 2016.  
<https://doi.org/10.2172/1237214>.
- [62] G.F. Knoll, Radiation Detection and Measurement, 4th Edition | Wiley, Wiley.Com. (n.d.). <https://www.wiley.com/en-us/Radiation+Detection+and+Measurement%2C+4th+Edition-p-9780470131480> (accessed February 29, 2020).
- [63] reuter\_stokes\_fission\_counter.pdf, (n.d.).  
[https://www.bakerhughesds.com/sites/g/files/cozyhq596/files/2018-07/reuter\\_stokes\\_fission\\_counter.pdf](https://www.bakerhughesds.com/sites/g/files/cozyhq596/files/2018-07/reuter_stokes_fission_counter.pdf) (accessed February 29, 2020).
- [64] J. Coburn, S.M. Luker, E.J. Parma, K.R. DePriest, Modeling, Calibration, and Verification of a Fission Chamber for ACRR Experimenters, EPJ Web of Conferences. 106 (2016) 05001. <https://doi.org/10.1051/epjconf/201610605001>.
- [65] S. Joo, J. Lee, S. Seo, Calibration of Digital Wide Range Neutron Power Measurement Channel for Open-Pool Type Research Reactor, *Nuclear Engineering and Technology*. 50 (2017). <https://doi.org/10.1016/j.net.2017.10.011>.

- [66] Z. Lyric, A review on the modeling of fission chambers, Kansas State University, 2017. <https://core.ac.uk/download/pdf/84312744.pdf> (accessed March 1, 2020).
- [67] B. Geslot, T. Unruh, P. Filliatre, C. Jammes, J. Di Salvo, S. Breaud, J.-F. Villard, Method to Calibrate Fission Chambers in Campbell Mode, *IEEE Transactions on Nuclear Science*. 59 (2011). <https://doi.org/10.1109/ANIMMA.2011.6172904>.
- [68] Triga Reactor Mainsystems, (n.d.). [https://ansn.iaea.org/Common/documents/Training/TRIGA%20Reactors%20\(Safety%20and%20Technology\)/chapter3/mainsystem54.htm](https://ansn.iaea.org/Common/documents/Training/TRIGA%20Reactors%20(Safety%20and%20Technology)/chapter3/mainsystem54.htm) (accessed March 1, 2020).
- [69] M.A. Reichenberger, P.B. Ugorowski, J.A. Roberts, D.S. McGregor, First-order numerical optimization of fission-chamber coatings using natural uranium and thorium, in: 2014 IEEE Nuclear Science Symposium and Medical Imaging Conference (NSS/MIC), 2014: pp. 1–4. <https://doi.org/10.1109/NSSMIC.2014.7431171>.
- [70] H. Böck, E. Balcar, Long-time behaviour of regenerating in-core neutron detectors with  $^{238}\text{U}$ – $^{239}\text{Pu}$  electrodes during power cycling, *Nuclear Instruments and Methods*. 124 (1975) 563–571. [https://doi.org/10.1016/0029-554X\(75\)90611-4](https://doi.org/10.1016/0029-554X(75)90611-4).
- [71] Z. W. Bell, M. J. Harrison, D. E. Holcomb, NEET-2.5 Material Selection for a High-Temperature Fission Chamber (ORNL-LTR-2012-331).pdf, n.d. [https://neup.inl.gov/SiteAssets/FY2014%20Documents/NEET-2.5%20Material%20Selection%20for%20a%20High-Temperature%20Fission%20Chamber%20\(ORNL-LTR-2012-331\).pdf](https://neup.inl.gov/SiteAssets/FY2014%20Documents/NEET-2.5%20Material%20Selection%20for%20a%20High-Temperature%20Fission%20Chamber%20(ORNL-LTR-2012-331).pdf) (accessed March 9, 2020).
- [72] Photonis, Neutron detector Product specification CFUC06, (n.d.).
- [73] Neutron moderator - Energy Education, (n.d.). [https://energyeducation.ca/encyclopedia/Neutron\\_moderator](https://energyeducation.ca/encyclopedia/Neutron_moderator) (accessed March 29, 2020).
- [74] G. Leinweber, D.P. Barry, R.C. Block, J.A. Burke, M.J. Rapp, K.E. Remley, Y. Danon, Neutron Capture And Total Cross Section Measurements Of Cadmium At The Rpi Linac, (2017) 9.
- [75] Cadmium 113 edge - cross-section, Nuclear Power. (n.d.). <https://www.nuclear-power.net/glossary/cadmium/cadmium-113-edge/> (accessed March 9, 2020).
- [76] A. Khudoleeva, S. Chirayath, W.S. Charlton, Conceptual Development of the Remote Monitoring System for Safeguarding of the Dry Cask Storage Facilities, in: Palm Desert, California, USA., 2013.

- [77] R.G. Fronk, S.L. Bellinger, L.C. Henson, D.E. Huddleston, T.R. Ochs, M.A. Reichenberger, C.J. Rietchek, C.T. Smith, T.J. Sobering, J.K. Shultis, D.S. McGregor, Advancements in microstructured semiconductor neutron detector (MSND)-based instruments, in: 2015 IEEE Nuclear Science Symposium and Medical Imaging Conference (NSS/MIC), 2015: pp. 1–5. <https://doi.org/10.1109/NSSMIC.2015.7581971>.
- [78] Doug Reilly, Norbert Ensslh Hastings smith Jr. Sarah Kreiner, Passive Nondestructive Assay of Nuclear Materials, n.d. <https://fas.org/sgp/othergov/doe/lanl/lib-www/la-pubs/00326408.pdf> (accessed March 9, 2020).
- [79] D.S. McGregor, W.J. McNeil, S.L. Bellinger, T.C. Unruh, J.K. Shultis, Microstructured semiconductor neutron detectors, Nuclear Instruments and Methods in Physics Research Section A: Accelerators, Spectrometers, Detectors and Associated Equipment. 608 (2009) 125–131. <https://doi.org/10.1016/j.nima.2009.06.031>.
- [80] A. Soto, R.G. Fronk, K. Neal, B. Ehresmann, S.L. Bellinger, M. Shoffner, D.S. McGregor, A semiconductor-based neutron detection system for planetary exploration, (n.d.) 28.
- [81] Neutron Scattering Lengths and cross sections, (n.d.). <https://www.ncnr.nist.gov/resources/n-lengths/elements/li.html> (accessed March 10, 2020).
- [82] Domino\_V5.40\_general\_spec\_sheet\_30percent.pdf, (n.d.). [http://radectech.com/content/Domino\\_V5.40\\_general\\_spec\\_sheet\\_30percent.pdf](http://radectech.com/content/Domino_V5.40_general_spec_sheet_30percent.pdf) (accessed March 10, 2020).
- [83] Coronavirus, (n.d.). <https://www.who.int/emergencies/diseases/novel-coronavirus-2019> (accessed March 30, 2020).
- [84] F.H. Froehner, Watt spectrum fit to  $^{252}\text{Cf}$  prompt fission neutron data, (1988). [http://inis.iaea.org/Search/search.aspx?orig\\_q=RN:20025173](http://inis.iaea.org/Search/search.aspx?orig_q=RN:20025173) (accessed March 30, 2020).
- [85] D.E. Baker, Graphite as a neutron moderator and reflector material, Nuclear Engineering and Design. 14 (1971) 413–444. [https://doi.org/10.1016/0029-5493\(70\)90160-3](https://doi.org/10.1016/0029-5493(70)90160-3).
- [86] Macroscopic Slowing Down Power - MSDP, Nuclear Power. (n.d.). <https://www.nuclear-power.net/glossary/macroscopic-slowing-down-power-msdp/> (accessed April 5, 2020).

- [87] Neutron cross section, Wikipedia. (2020).  
[https://en.wikipedia.org/w/index.php?title=Neutron\\_cross\\_section&oldid=945857745](https://en.wikipedia.org/w/index.php?title=Neutron_cross_section&oldid=945857745) (accessed April 5, 2020).
- [88] Dry Cask Storage, (n.d.). <http://large.stanford.edu/courses/2014/ph241/ng2/>  
(accessed May 24, 2020).
- [89] E. Stewart, Principles of Total Neutron Counting, (n.d.) 28.

APPENDIX A

SAMPLE MCNP INPUT

A sample MCNP Input Deck

```

C   Westinghouse Fuel Assembly
C   ----- Cell cards -----
C   ----- Fuel Cell -----
C
101 1 -10.46 -101 +115 -116          u=1 imp:n=1    $Fuel Rod
102 0   +101 -102 +117 -118          u=1 imp:n=1    $Diametral gap
103 2 -6.55  +102 -103              u=1 imp:n=1    $Zircaloy 4 Cladding
104 0   +103                          u=1 imp:n=1    $void between fuel cells
C   ----- plenum cell -----
C
108 0   -101 +117 -115              u=1 imp:n=1    $lower plenum void
109 0   -101 +116 -118              u=1 imp:n=1    $upper plenum void
110 2 -6.55 -102 -117              u=1 imp:n=1    $lower plenum clad
111 2 -6.55 -102 +118              u=1 imp:n=1    $upper plenum clad
C   ----- Guide Tube -----
C
105 0   -102                          u=2 imp:n=1    $Void inside clad
106 2 -6.55  +102 -103              u=2 imp:n=1    $Zircaloy 4 Cladding
107 0   +103                          u=2 imp:n=1    $space between fuel cells
C
C
c 112 0  121 -122 123 -124 117 -118 fill=3    u=33    imp:n=1
c   ----- Fuel Rod ASSEMBLY -----
c
201 0 111 -112 113 -114    u=3 lat=1 fill= -16:0 -16:0 0:0
  1 1 1 1 1 1 1 1 1 1 1 1 1 1 1 1 1 1
  1 1 1 1 1 1 1 1 1 1 1 1 1 1 1 1 1 1
  1 1 1 1 1 2 1 1 2 1 1 2 1 1 1 1 1 1
  1 1 1 2 1 1 1 1 1 1 1 1 1 2 1 1 1 1
  1 1 1 1 1 1 1 1 1 1 1 1 1 1 1 1 1 1
  1 1 2 1 1 2 1 1 2 1 1 2 1 1 2 1 1 1
  1 1 1 1 1 1 1 1 1 1 1 1 1 1 1 1 1 1
  1 1 1 1 1 1 1 1 1 1 1 1 1 1 1 1 1 1
  1 1 2 1 1 2 1 1 2 1 1 2 1 1 2 1 1 1
  1 1 1 1 1 1 1 1 1 1 1 1 1 1 1 1 1 1
  1 1 1 1 1 1 1 1 1 1 1 1 1 1 1 1 1 1

```

```

1 1 2 1 1 2 1 1 2 1 1 2 1 1 2 1 1
1 1 1 1 1 1 1 1 1 1 1 1 1 1 1 1 1
1 1 1 2 1 1 1 1 1 1 1 1 1 2 1 1 1
1 1 1 1 1 2 1 1 2 1 1 2 1 1 1 1 1
1 1 1 1 1 1 1 1 1 1 1 1 1 1 1 1 1
1 1 1 1 1 1 1 1 1 1 1 1 1 1 1 1 1   imp:n=1 $ ----- Surface cards -----
c 202  0  -121:122:-123:124:-117:118   imp:n=0 $kill zone
C  ----- Assembly sized void -----
C
301  0   +129 -130 +131 -132 #302 #303 #304 #305   u=20 imp:n=1 $
302  3 -7.92 +129 -133 +131 -132   u=20 imp:n=1 $stainless steel
panel left
303  3 -7.92 +133 -142 +131 -143   u=20 imp:n=1 $stainless steel
panel bottom
304  3 -7.92 +142 -130 +131 -132   u=20 imp:n=1 $stainless steel
panel right
305  3 -7.92 +133 -142 +152 -132   u=20 imp:n=1 $stainless steel
panel top
C
C  ----- Assembly (no boral) -----
C
306  0   +121 -122 +123 -124   fill=3 u=10 imp:n=1 $Assembly
307  3 -7.92 +129 -133 +131 -132   u=10 imp:n=1 $stainless steel
panel left
308  3 -7.92 +133 -142 +131 -143   u=10 imp:n=1 $stainless steel
panel bottom
309  3 -7.92 +142 -130 +131 -132   u=10 imp:n=1 $stainless steel
panel right
310  3 -7.92 +133 -142 +152 -132   u=10 imp:n=1 $stainless steel
panel top
311  0   +129 -130 +131 -132 #306 #307 #308 #309 #310   u=10 imp:n=1 $
C  ----- Assembly (top boral) -----
C
312  0   +121 -122 +123 -124   fill=3 u=11 imp:n=1 $Assembly
313  3 -7.92 +129 -133 +131 -132   u=11 imp:n=1 $stainless steel
panel left
314  3 -7.92 +133 -142 +131 -143   u=11 imp:n=1 $stainless steel
panel bottom
315  3 -7.92 +142 -130 +131 -132   u=11 imp:n=1 $stainless steel
panel right
316  3 -7.92 +133 -142 +152 -132   u=11 imp:n=1 $stainless steel
panel top
317  4 -1.70 +137 -138 +151 -152   u=11 imp:n=1 $boral Top

```

318 3 -7.92 +137 -138 +150 -151 u=11 imp:n=1 \$stainless steel  
sheath top  
319 3 -7.92 +138 -139 +150 -152 u=11 imp:n=1 \$stainless steel  
sheath top  
320 3 -7.92 +136 -137 +150 -152 u=11 imp:n=1 \$stainless steel  
sheath top  
321 0 +129 -130 +131 -132 #312 #313 #314 #315 #316 #317 &  
#318 #319 #320 u=11 imp:n=1 \$  
C ----- Assembly (top & left Boral) -----  
C  
322 0 +121 -122 +123 -124 fill=3 u=12 imp:n=1 \$Assembly  
323 3 -7.92 +129 -133 +131 -132 u=12 imp:n=1 \$stainless steel  
panel left  
324 3 -7.92 +133 -142 +131 -143 u=12 imp:n=1 \$stainless steel  
panel bottom  
325 3 -7.92 +142 -130 +131 -132 u=12 imp:n=1 \$stainless steel  
panel right  
326 3 -7.92 +133 -142 +152 -132 u=12 imp:n=1 \$stainless steel  
panel top  
327 4 -1.70 +137 -138 +151 -152 u=12 imp:n=1 \$boral Top  
328 4 -1.70 +133 -134 +147 -148 u=12 imp:n=1 \$boral left  
329 3 -7.92 +134 -135 +147 -148 u=12 imp:n=1 \$stainless steel  
sheath left  
330 3 -7.92 +137 -138 +150 -151 u=12 imp:n=1 \$stainless steel  
sheath top  
331 3 -7.92 +133 -135 +146 -147 u=12 imp:n=1 \$stainless steel  
sheath 1  
332 3 -7.92 +138 -139 +150 -152 u=12 imp:n=1 \$stainless steel  
sheath 6  
333 3 -7.92 +136 -137 +150 -152 u=12 imp:n=1 \$stainless steel  
sheath 7  
334 3 -7.92 +133 -135 +148 -149 u=12 imp:n=1 \$stainless steel  
sheath 8  
335 0 +129 -130 +131 -132 #322 #323 #324 #325 #326 #327 &  
#328 #329 #330 #331 #332 #333 #334 u=12 imp:n=1 \$  
c  
C ----- Assembly (top & left Boral) -----  
C  
1322 0 +121 -122 +123 -124 u=15 imp:n=1 \$Assembly  
1323 3 -7.92 +129 -133 +131 -132 u=15 imp:n=1 \$stainless steel panel  
left  
1324 3 -7.92 +133 -142 +131 -143 u=15 imp:n=1 \$stainless steel panel  
bottom

1325	3 -7.92 +142 -130 +131 -132	u=15 imp:n=1 \$stainless steel panel
right		
1326	3 -7.92 +133 -142 +152 -132	u=15 imp:n=1 \$stainless steel panel
top		
1327	4 -1.70 +137 -138 +151 -152	u=15 imp:n=1 \$boral Top
1328	4 -1.70 +133 -134 +147 -148	u=15 imp:n=1 \$boral left
1329	3 -7.92 +134 -135 +147 -148	u=15 imp:n=1 \$stainless steel sheath
left		
1330	3 -7.92 +137 -138 +150 -151	u=15 imp:n=1 \$stainless steel sheath
top		
1331	3 -7.92 +133 -135 +146 -147	u=15 imp:n=1 \$stainless steel sheath
1		
1332	3 -7.92 +138 -139 +150 -152	u=15 imp:n=1 \$stainless steel sheath
6		
1333	3 -7.92 +136 -137 +150 -152	u=15 imp:n=1 \$stainless steel sheath
7		
1334	3 -7.92 +133 -135 +148 -149	u=15 imp:n=1 \$stainless steel sheath
8		
1335	0 +129 -130 +131 -132 #1322 #1323 #1324 #1325 #1326 #1327 & #1328 #1329 #1330 #1331 #1332 #1333 #1334 u=15 imp:n=1 \$	
c	----- Assembly (left Boral) -----	
C		
336	0 +121 -122 +123 -124	fill=3 u=13 imp:n=1 \$Assembly
337	3 -7.92 +129 -133 +131 -132	u=13 imp:n=1 \$stainless steel
panel left		
338	3 -7.92 +133 -142 +131 -143	u=13 imp:n=1 \$stainless steel
panel bottom		
339	3 -7.92 +142 -130 +131 -132	u=13 imp:n=1 \$stainless steel
panel right		
340	3 -7.92 +133 -142 +152 -132	u=13 imp:n=1 \$stainless steel
panel top		
341	4 -1.70 +133 -134 +147 -148	u=13 imp:n=1 \$boral left
342	3 -7.92 +134 -135 +147 -148	u=13 imp:n=1 \$stainless steel
sheath left		
343	3 -7.92 +133 -135 +146 -147	u=13 imp:n=1 \$stainless steel
sheath left		
344	3 -7.92 +133 -135 +148 -149	u=13 imp:n=1 \$stainless steel
sheath left		
345	0 +129 -130 +131 -132 #336 #337 #338 #339 #340 #341 & #342 #343 #344 u=13 imp:n=1 \$	
c	----- Assembly (left Boral) DUMMY -----	
C		
1336	0 +121 -122 +123 -124	u=14 imp:n=1 \$Assembly

1337	3 -7.92 +129 -133 +131 -132	u=14 imp:n=1 \$stainless steel panel
left		
1338	3 -7.92 +133 -142 +131 -143	u=14 imp:n=1 \$stainless steel panel
bottom		
1339	3 -7.92 +142 -130 +131 -132	u=14 imp:n=1 \$stainless steel panel
right		
1340	3 -7.92 +133 -142 +152 -132	u=14 imp:n=1 \$stainless steel panel
top		
1341	4 -1.70 +133 -134 +147 -148	u=14 imp:n=1 \$boral left
1342	3 -7.92 +134 -135 +147 -148	u=14 imp:n=1 \$stainless steel
sheath left		
1343	3 -7.92 +133 -135 +146 -147	u=14 imp:n=1 \$stainless steel
sheath left		
1344	3 -7.92 +133 -135 +148 -149	u=14 imp:n=1 \$stainless steel
sheath left		
1345	0 +129 -130 +131 -132 #1336 #1337 #1338 #1339 #1340 #1341 & #1342 #1343 #1344	u=14 imp:n=1 \$
C		
C	----- Assembly sized void (left panel) -----	
C		
346	0 +129 -130 +131 -132 #347	u=21 imp:n=1 \$
347	3 -7.92 +129 -133 +131 +142 -132	u=21 imp:n=1 \$stainless steel
panel left		
C		
C	----- Assembly sized void (bottom panel) -----	
C		
348	0 +129 -130 +131 -132 #349	u=22 imp:n=1 \$
349	3 -7.92 +127 -126 +131 -143	u=22 imp:n=1 \$stainless steel
panel bottom		
C		
C	----- Assembly sized void (right panel) -----	
C		
350	0 +129 -130 +131 -132 #351	u=23 imp:n=1 \$
351	3 -7.92 +142 -130 +131 -133 +142 -132	u=23 imp:n=1 \$stainless
steel panel right		
C		
C	----- Assembly sized void (top panel) -----	
C		
352	0 +129 -130 +131 -132 #353	u=24 imp:n=1 \$
353	3 -7.92 +127 -128 +152 -132	u=24 imp:n=1 \$stainless steel
panel top		
C		
C	----- Assembly sized void (left & bottom panel) -----	
C		

```

354 0 +129 -130 +131 -132 #355 #356 u=25 imp:n=1 $
355 3 -7.92 +129 -133 +131 -132 u=25 imp:n=1 $stainless steel
panel left
356 3 -7.92 +133 -126 +131 -143 u=25 imp:n=1 $stainless steel
panel bottom
C
C ----- Assembly sized void (right & bottom panel) -----
C
357 0 +129 -130 +131 -132 #358 #359 u=26 imp:n=1 $
358 3 -7.92 +142 -130 +131 -132 u=26 imp:n=1 $stainless steel
panel right
359 3 -7.92 +127 -142 +131 -143 u=26 imp:n=1 $stainless steel
panel bottom
C
C ----- Assembly sized void (left & top panel) -----
C
360 0 +129 -130 +131 -132 #361 #362 u=27 imp:n=1 $
361 3 -7.92 +129 -133 +131 -132 u=27 imp:n=1 $stainless steel
panel left
362 3 -7.92 +133 -128 +152 -132 u=27 imp:n=1 $stainless steel
panel top
C
C ----- Assembly sized void (right & top panel) -----
C
363 0 +129 -130 +131 -132 #364 #365 u=28 imp:n=1 $
364 3 -7.92 +142 -130 +131 -132 u=28 imp:n=1 $stainless steel
panel right
365 3 -7.92 +127 -142 +152 -132 u=28 imp:n=1 $stainless steel
panel top
C
400 0 -161 117 -118 fill =6 imp:n=1 $ containment
401 0 +125 -126 +127 -128 u=6 lat=1 fill=-3:5 -3:5 0:0
21 20 22 22 22 22 20 23 20
21 25 13 13 13 10 26 23 20 $ row 1
21 13 12 12 12 12 10 23 20 $ row 2
21 12 12 12 12 12 11 23 20 $ row 3
21 12 12 12 12 12 11 23 20 $ row 4
21 12 12 12 12 12 11 23 20 $ row 5
21 27 12 12 12 11 28 23 20 $ row 6
21 20 24 24 24 24 20 23 20
21 20 20 20 20 20 20 23 20 imp:n=1
402 3 -7.92 161 -162 117 -196 imp:n=1 $ Stainless Steel
403 0 162 -163 117 -196 imp:n=1 $air
404 6 -7.82 163 -164 117 -196 imp:n=1 $carbon steel

```

405 5 -2.55 164 -165 117 -200 imp:n=1 \$concrete  
 407 6 -7.82 165 -166 117 -197 imp:n=1 \$carbon steel  
 408 3 -7.92 164 -165 200 -197 imp:n=1 \$side ss  
 406 0 166:-194:1999 imp:n=0  
 C ----- MPC Lid and Base -----  
 C  
 417 3 -7.92 -117 194 -166 imp:n=1 \$ steel containment base  
 418 0 -161 118 -195 imp:n=1 \$air on top  
 419 3 -7.92 -161 195 -196 imp:n=1 \$\$SS on top  
 420 0 -164 196 -197 imp:n=1 \$air on top  
 c ----- Start imp biasing in concrete 20cm -----  
 1971 5 -2.55 -166 197 -1971 imp:n=2 \$ 2 cm concrete  
 1972 5 -2.55 -166 1971 -1972 imp:n=4 \$ 2 cm concrete  
 1973 5 -2.55 -166 1972 -1973 imp:n=8 \$ 2 cm concrete  
 1974 5 -2.55 -166 1973 -1974 imp:n=16 \$ 2 cm concrete  
 1975 5 -2.55 -166 1974 -1975 imp:n=32 \$ 2 cm concrete  
 1976 5 -2.55 -166 1975 -1976 imp:n=64 \$ 2 cm concrete  
 1977 5 -2.55 -166 1976 -1977 imp:n=128 \$ 2 cm concrete  
 1978 5 -2.55 -166 1977 -1978 imp:n=256 \$ 2 cm concrete  
 1979 5 -2.55 -166 1978 -1979 imp:n=512 \$ 2 cm concrete  
 421 5 -2.55 -166 1979 -198 imp:n=1024 \$ 2 cm concrete  
 c ----- Start imp biasing in SS 2.54 cm -----  
 1981 3 -7.92 -166 198 -1981 imp:n=2048 \$1 cm SS  
 1982 3 -7.92 -166 1981 -1982 imp:n=4096 \$1 cm SS  
 422 3 -7.92 -166 1982 -199 imp:n=8192 \$0.54 cm SS  
 1999 0 -166 199 1991 991 981 -1999 imp:n=16384 \$ quantifier box  
 991 7 -0.93 -991 imp:n=16384  
 981 7 -0.93 -981 imp:n=16384  
 1991 0 -1991 imp:n=16384  
 c ----- Detectors -----  
 c 500 7 -0.93 -500 501 502 503 701 imp:n=1 \$ 46x46x7.08 box  
 c 701 7 -0.93 -701 imp:n=1 \$ Top quantifier box  
 c 501 8 -2.7 -501 imp:n=1 \$ Cd  
 c 502 0 -512 imp:n=1 \$ left detector  
 c 503 0 -513 imp:n=1 \$ right detector  
 c 504 9 -19.1 512 -502 imp:n=1 \$ left detector uranium lining  
 c 505 9 -19.1 513 -503 imp:n=1 \$right detector uranium lining  
 C -----  
 C ----- Fuel Pin Surfaces -----  
 C -----  
 101 c/z 1.4417675 1.6322675 0.392176  
 102 c/z 1.4417675 1.6322675 0.40005  
 103 c/z 1.4417675 1.6322675 0.4572

104 pz -203.16825  
 105 pz +203.16825  
 106 pz -226.456875  
 107 pz +226.456875  
 108 pz -232.806875  
 109 pz +249.634375  
 110 pz +250.586875  
 C ----- plenum -----  
 C  
 115 pz -190.5  
 116 pz +190.5  
 117 pz -201.16825  
 118 pz +201.16825  
 C ----- Basic Lattice Cell -----  
 C  
 111 px +0.8118475  
 112 px +2.0716875  
 113 py +1.0023475  
 114 py +2.2621875  
 C ----- Basic assembly cell -----  
 C C  
 121 px +0.8118475  
 122 px +22.2291275  
 123 py +1.0023475  
 124 py +22.4196275  
 C ----- Assembly pitch -----  
 C  
 125 px 0  
 126 px +23.046975  
 127 py 0  
 128 py +23.421975  
 C  
 C ----- Assembly universe -----  
 C  
 129 px -1  
 130 px +24  
 131 py -1  
 132 py +24  
 C  
 C -----  
 C  
 133 px 0.3571875  
 134 px 0.6137275  
 135 px 0.7026275

136 px 1.9065875  
 137 px 1.9954875  
 138 px 21.0454875  
 139 px 21.1343875  
 140 px 22.3384875  
 141 px 22.4273875  
 142 px 22.6837875

C

C -----

C

143 py 0.3571875  
 144 py 0.6137275  
 145 py 0.7036275  
 146 py 2.0970875  
 147 py 2.1859875  
 148 py 21.2359875  
 149 py 21.3248875  
 150 py 22.7193475  
 151 py 22.8082475  
 152 py 23.0647875

C

C ----- Containment -----

C

161 cz 84.455      \$Inner radius of cask boundary  
 162 cz 85.855      \$1.4 cm SS  
 163 cz 93.405      \$7.55 cm air  
 164 cz 95.945      \$2.54 cm of Carbon steel  
 165 cz 165.745      \$69.8 cm of concrete  
 166 cz 166.52      \$0.764cm of carbon steel

c 160 cz 67.31

c -----Cask Lid and Base -----

194 pz -227.66825      \$26.5cm of SS from plenum bottom  
 195 pz 224.45825      \$23.29cm air  
 196 pz 248.45825      \$24 cm SS  
 200 pz 258.45825      \$side ss cutoff  
 197 pz 266.45825      \$18cm air

c ----- Start imp biasing in concrete 20cm -----

1971 pz 268.45825      \$ 2 cm concrete  
 1972 pz 270.45825      \$ 2 cm concrete  
 1973 pz 272.45825      \$ 2 cm concrete  
 1974 pz 274.45825      \$ 2 cm concrete  
 1975 pz 276.45825      \$ 2 cm concrete  
 1976 pz 278.45825      \$ 2 cm concrete  
 1977 pz 280.45825      \$ 2 cm concrete

```

1978 pz 282.45825      $ 2 cm concrete
1979 pz 284.45825      $ 2 cm concrete
198  pz 286.45825      $20cm concrete
c ----- Start imp biasing in SS 2.54 cm -----
1981 pz 287.45825      $ 1 cm SS
1982 pz 288.45825      $ 1 cm SS
199  pz 288.99825      $ 0.54cm SS
1999 pz 293.99825      $ quantifier box 5cm tall
991  RPP -4 4 -2 2 289 290.5  $ poly under
981  RPP -4 4 -2 2 290.55 293.05 $ poly above
1991 RPP -4 4 -2 2 290.5 290.55 $ Quantifier
c 700 RPP -23 23 -23 23 246.45 248.45 $ bottom quantifier box
c 195 px +69.1402
c 196 py -70.623
c 197 py +70.623
c 264 cz 90
      $ right detector Uranium lining
c -----Detectors-----
500 RPP -23 23 -23 23 248.55 257.13 $ 8.58 cm of Poly block
701 RPP -23 23 -23 23 248.55 250.55 $ Stop quantifier box
501 RPP -23 23 -23 23 248.5 248.55 $ 0.05cm of Cd., x and y width of 34.8cm
502 RCC -11.4 -11.5 253.59 0 23 0 2.54 $ left detector
512 RCC -11.4 -11.5 253.59 0 23 0 2.5399926702 $ left detector Uranium lining
503 RCC 11.4 -11.5 253.59 0 23 0 2.54 $ right detector
513 RCC 11.4 -11.5 253.59 0 23 0 2.5399926702 $ right detector Uranium lining

c ---DATA CARDS
mode n
sdef pos=d1 x=fpos D2 y=fpos D9 z=D16 erg=D17
si1 1 000000000000000000000000000000
      000000000000000000000000000000
      000000000000000000000000000000
      000000000000000000000000000000
spl d 1 1 1 1 1 1 1 1
      1 1 1 1 1 1 1 1
      1 1 1 1 1 1 1 1
      1 1 1 1 1 1 1 1
DS2 s 3 3 3 3 4 4 4 4 4 4 5 5 5 5 5 5 6 6 6 6 6 6
      7 7 7 7 7 7 8 8 8 8
Si3 -68.3290775 -46.9117975
Sp3 0 1
Si4 -45.2821025 -23.8648225
Sp4 0 1
Si5 -22.2351275 -0.8178475

```

```

Sp5  0 1
Si6  0.8118475 22.2291275
Sp6  0 1
Si7  23.8588225 45.2761025
Sp7  0 1
Si8  46.9057975 68.3230775
Sp8  0 1
ds9  s  11 12 13 14 10 11 12 13 14 15 10 11 12 13 14 15
      10 11 12 13 14 15 10 11 12 13 14 15 11 12 13 14
Si10 -69.2635775 -47.8462975
Sp10 0 1
Si11 -45.8416025 -24.4243225
Sp11 0 1
Si12 -22.4196275 -1.0023475
Sp12 0 1
Si13  1.0023475 22.4196275
Sp13 0 1
Si14  24.4243225 45.8416025
Sp14 0 1
Si15  47.8462975 69.2635775
Sp15 0 1
SI16 -190.5 190.5      $ fuel height
SP16 0 1
SI17 H 0.1  0.4  0.9  1.4  1.85
      3.0  6.43  20
SP17 D 0      1.80E+07 9.21E+07 8.43E+07 6.21E+07
      1.09E+08 9.96E+07 8.84E+06
c -----Tallies and Detectors -----
c FMESH24:n GEOM=XYZ ORIGIN=-170 -170 289
c   IMESH= 170 IINTS= 16
c   JMESH= 170 JINTS= 16
c   KMESH= 289.5 KINTS= 1
c   EMESH= 0.5E-06 0.1 20
F4:N 1991
e0  0.25E-07
    0.5E-06
    0.1
    2E+01
c -----MATERIAL CARDS
C  ----- MPC Material cards -----
C
C  ----- UO2 -----
m1  92235  -0.035258615      $UO2 fuel 4% enriched density 10.46g/cc
    92238  -0.845966244

```

92234 -0.000240509  
 08016 -0.118534632  
 C ----- Zircaloy-4 -----  
 C  
 m2 40000 -98.23 \$Zircaloy-4  
 50000 -1.45  
 26000 -0.21  
 24000 -0.1  
 72000 -0.01  
 C  
 C ----- SS304 -----  
 C  
 m3 24000 2.09848e-1  
 26056 6.80967e-1 \$SS304  
 28000 8.8815e-2  
 25055 2.03702e-2  
 C  
 C ----- Boral -----  
 C  
 m4 13027 -0.6861 \$Boral  
 06000 -0.0682  
 05010 -0.044226  
 05011 -0.201474  
 C  
 C ----- Concrete -----  
 C  
 m5 14000 -0.315 \$Concrete  
 13027 -0.048  
 8016 -0.5  
 1001 -0.006  
 11023 -0.017  
 20000 -0.083  
 26000 -0.012  
 19000 -0.019  
 C  
 C ----- Carbon Steel -----  
 C  
 m6 6012 0.022831 \$Carbon steel  
 26000 0.977170  
 C ----- Polyethylene -----  
 m7 1001 -0.143716 \$Polyethylene  
 6012 -0.856284  
 C ----- Cadmium -----  
 m8 48000 1 \$Cadmium

C ----- Uranium-235 -----  
m9 92235 1 \$Uranium  
CUT:n 2j 0 0 \$ turns on analog capture  
NPS 1e8  
PRDMP -1440 -1440  
c VOID 500 701 501 502 503 504 505

## APPENDIX B

### MCNP VARIANCE REDUCTION TECHNIQUES

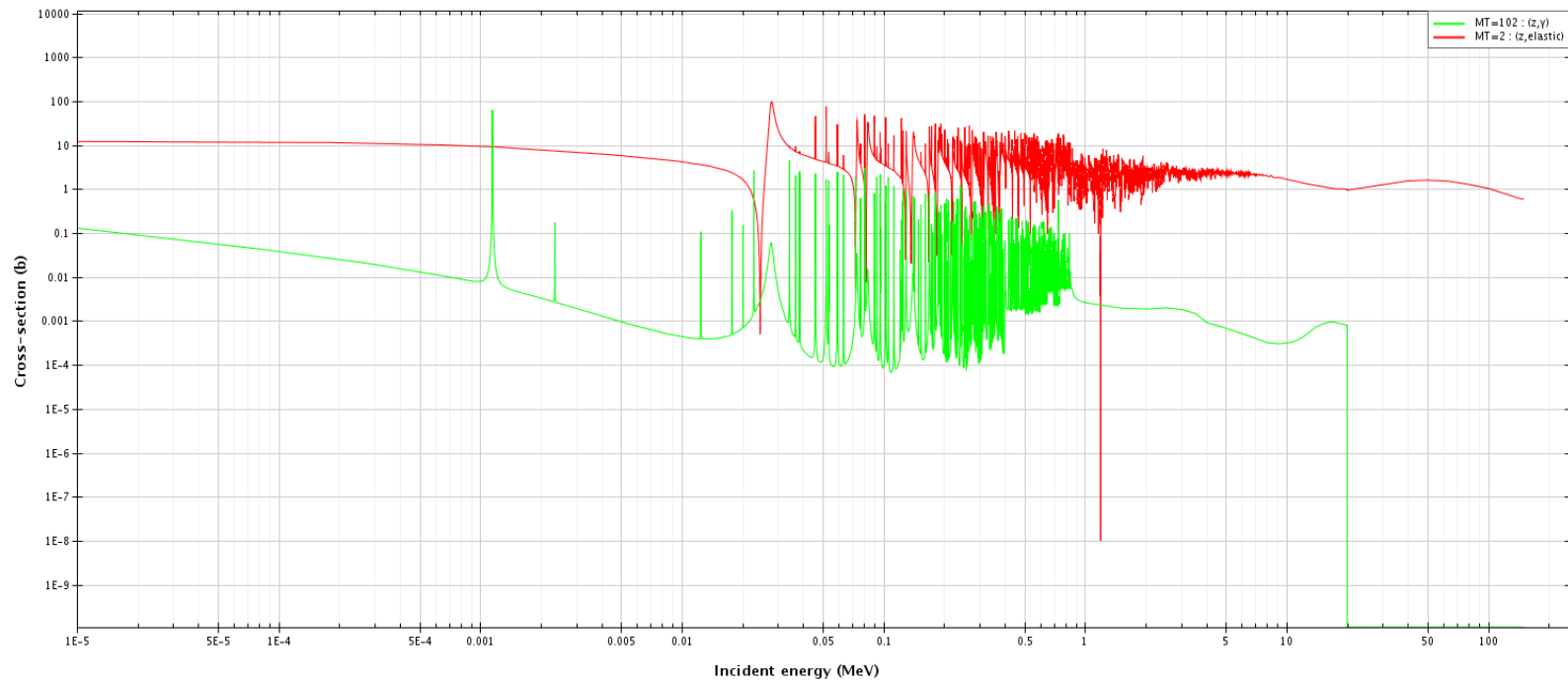
Effect of variance reduction techniques on tally mean, relative error, variance of variance, figure of merit, slope and computer time from MCNP simulations of external RMS configurations( No VR= No variance reduction techniques, GS= Geometry splitting, GS+AC= Geometry Splitting and Analog Capture)

	Mean			Relative Error			Variance of Variance			Figure of Merit			Slope			Computer Time (minutes)		
	No VR	GS	GS+AC	No VR	GS	GS+AC	No VR	GS	GS+AC	No VR	GS	GS+AC	No VR	GS	GS+AC	No VR	GS	GS+AC
Full 2x2	1.87E-07	1.59E-07	1.58E-07	0.122	0.004	0.003	0.0505	0.0002	0.0002	7.80E-03	10	7.5	0	3.8	4	8961.4	7774.3	13028
Ext 1_DS_0	1.22E-06	2.31E-07	2.31E-07	0.041	0.003	0.003	0.011	0.0004	0.0001	6.80E-02	13	10	10	3.5	3.6	8934.3	7148.6	11722.7
DS 1	1.91E-07	1.59E-07	1.59E-07	0.142	0.004	0.003	0.0801	0.0001	0.0012	5.70E-03	10	7.4	0	4.3	3.7	9047.2	7777.1	12974.5
DS 2	2.00E-07	1.57E-07	1.57E-07	0.138	0.004	0.003	0.0762	0.0001	0.0012	6.10E-03	10	7.3	0	3.6	3.6	9036	7793.1	12891.18
DS 3	1.88E-07	1.56E-07	1.56E-07	0.134	0.004	0.003	0.0649	0.0002	0.0002	6.50E-03	10	7.5	0	3.1	4.6	9041.2	7814.7	12794.52
DS 4	1.89E-07	1.59E-07	1.60E-07	0.144	0.004	0.003	0.0806	0.0001	0.0011	5.60E-03	10	7.3	0	4.2	3.6	9172.2	7780.8	13140.87
DS 5	1.98E-07	1.58E-07	1.58E-07	0.140	0.004	0.003	0.0756	0.0001	0.0012	6.00E-03	10	7.3	0	4.3	3.7	8927	7714	13024.71
DS 6	1.51E-07	1.62E-07	1.60E-07	0.137	0.004	0.003	0.1305	0.0002	0.0012	6.10E-03	10	7.3	0	4	3.5	9255.9	7868.4	13156.97
DS 7	1.57E-07	1.54E-07	1.54E-07	0.128	0.004	0.003	0.0589	0.002	0.0002	7.30E-03	9.8	7.5	0	3.1	3.6	8759	7646.3	12698.44
DS_8	1.95E-07	1.57E-07	1.56E-07	0.129	0.004	0.003	0.0772	0.002	0.0012	6.90E-03	9.7	7.3	0	3	3.5	9141.2	7703.3	12916.05
Full 3x3	2.10E-07	1.81E-07	1.80E-07	0.091	0.004	0.003	0.0582	0.0001	0.0001	1.40E-02	11	8.2	0	3.8	3.7	8920.8	7872.7	12953.42
DS_0	1.45E-06	2.61E-07	2.61E-07	0.031	0.003	0.003	0.0132	0.0001	0.0001	1.20E-01	15	11	6.7	3.1	3.8	8963.3	7220.3	11788.52
DS 1	1.86E-07	1.82E-07	1.82E-07	0.091	0.004	0.003	0.0777	0.0001	0.0002	1.40E-02	11	8.1	0	4.6	3.9	9020.1	7815.7	13004.52
DS 2	2.01E-07	1.80E-07	1.79E-07	0.089	0.004	0.003	0.0654	0.0001	0.0002	1.50E-02	11	8.1	0	4.8	3.5	8876.1	7704.9	13022.34
DS 3	1.95E-07	1.78E-07	1.78E-07	0.094	0.004	0.003	0.0646	0.0001	0.0001	1.30E-02	11	8.1	0	4	4.1	8832.5	7653.2	13110.05
DS 4	1.86E-07	1.82E-07	1.82E-07	0.092	0.004	0.003	0.0758	0.0001	0.0002	1.40E-02	11	8	0	4.3	3.6	9025	8132.1	13445.19
DS 5	1.95E-07	1.81E-07	1.81E-07	0.090	0.004	0.003	0.0706	0.0001	0.0002	1.40E-02	11	8.1	0	4.3	3.5	9019.1	7731.6	12971.37
DS 6	1.99E-07	1.85E-07	1.84E-07	0.091	0.003	0.003	0.0558	0.0001	0.0002	1.40E-02	11	8.1	0	3.3	3.1	9201.2	7913.1	13149.45
DS 7	2.03E-07	1.75E-07	1.75E-07	0.094	0.004	0.003	0.0593	0.0005	0.0001	1.30E-02	11	8.1	0	3.6	4.1	8794.2	7613.3	12816.56
DS 8	2.02E-07	1.79E-07	1.78E-07	0.084	0.004	0.003	0.0297	0.0005	0.0001	1.70E-02	11	8.2	0	3.1	3.3	8903.5	7693.3	12892.86
Full 4x2	1.76E-07	1.74E-07	1.73E-07	0.093	0.003	0.003	0.0488	0.0001	0.0002	1.30E-02	11	8.1	0	5	4.2	9103.1	8020.5	13063.54
Ext 4_2_DS_0	1.32E-06	2.50E-07	2.50E-07	0.030	0.003	0.003	0.0071	0.0001	0.0001	1.30E-01	15	11	7.6	3.4	3.9	9107.3	7155.8	11806.56
DS 1	1.65E-07	1.74E-07	1.74E-07	0.092	0.003	0.003	0.0397	0.0001	0.0003	1.30E-02	11	8.1	0	4.7	3.3	9230	7778.6	13098.53
DS 2	1.75E-07	1.72E-07	1.72E-07	0.091	0.003	0.003	0.036	0.0001	0.0003	1.40E-02	11	8	0	4.8	3.3	8917.4	7728	13031.97
DS 3	1.69E-07	1.71E-07	1.71E-07	0.093	0.003	0.003	0.0413	0.0001	0.0002	1.30E-02	11	8.1	0	4.9	3.6	8900.2	7687.9	12929.29
DS 4	1.64E-07	1.74E-07	1.74E-07	0.094	0.003	0.003	0.0392	0.0001	0.0003	1.30E-02	11	8.1	0	4.2	3.3	8967.6	7812.5	13271.73
DS 5	1.68E-07	1.73E-07	1.73E-07	0.091	0.003	0.003	0.039	0.0001	0.0003	1.40E-02	11	8.1	0	4.6	3.3	8988	7741.7	13083.05
DS 6	1.45E-07	1.76E-07	1.76E-07	0.089	0.003	0.003	0.0563	0.0001	0.0003	1.40E-02	11	8.1	0	3.6	3.6	9130.1	7890	13212.64
DS 7	1.71E-07	1.68E-07	1.69E-07	0.093	0.004	0.003	0.0409	0.0002	0.0001	1.40E-02	11	8.2	0	4	5.5	8781.7	7596.1	12837.57
DS 8	1.68E-07	1.71E-07	1.70E-07	0.091	0.004	0.003	0.0402	0.0003	0.0002	1.40E-02	11	8.2	0	3.1	4.4	8802	7754.2	13007.55
Full 4x4	2.13E-07	1.97E-07	1.97E-07	0.062	0.003	0.003	0.0175	0.0001	0.0001	3.00E-02	12	8.5	10	4	5.6	8934.2	7821.7	12940.15
Ext 4_4_DS_0	1.50E-06	2.85E-07	2.84E-07	0.024	0.003	0.003	0.0118	0.0001	0.0001	2.00E-01	15	11	6.2	3.8	4.1	8943.5	7160	11856.69
DS 1	1.92E-07	1.98E-07	1.98E-07	0.065	0.003	0.003	0.0264	0.0001	0.0001	2.70E-02	12	8.4	7.1	10	4.9	9149.8	7821.1	13210.03
DS 2	2.00E-07	1.95E-07	1.96E-07	0.064	0.003	0.003	0.0245	0.0001	0.0001	2.80E-02	12	8.4	10	8.4	5.4	8979.7	7700	13035.85
DS 3	2.01E-07	1.94E-07	1.94E-07	0.063	0.003	0.003	0.0146	0.0001	0.0001	3.00E-02	12	8.4	10	4.5	10	9144.1	7711.3	12924.44
DS 4	1.91E-07	1.99E-07	1.99E-07	0.066	0.003	0.003	0.0262	0.0001	0.0001	2.70E-02	12	8.4	5.6	9.3	5.3	9025.2	7859.3	13382.41
DS 5	1.95E-07	1.97E-07	1.98E-07	0.064	0.003	0.003	0.0261	0.0001	0.0001	2.80E-02	12	8.4	6.2	10	5.6	8944.2	7803.6	13021.73
DS 6	2.06E-07	2.01E-07	2.01E-07	0.066	0.003	0.003	0.0289	0.0001	0.0001	2.60E-02	12	8.6	2.7	4.6	3.9	9125.1	7851.4	13117.64
DS 7	2.24E-07	1.91E-07	1.92E-07	0.065	0.003	0.003	0.0187	0.0001	0.0001	2.80E-02	11	8.4	10	4.3	6.1	8785.1	7658.1	12814.13
DS 8	2.14E-07	1.95E-07	1.95E-07	0.065	0.003	0.003	0.0268	0.0001	0.0001	2.80E-02	11	8.5	6	3.7	3.8	8806.7	8005	12870.7

# APPENDIX C

## CROSS SECTIONS

Neutron elastic scattering and radiative capture cross sections for  $^{56}\text{Fe}$  obtained from ENDF/B-VI.8 libraries through JANIS OECD



## APPENDIX D

### OPTIMIZATION OF EXTERNAL RMS

Energy discriminated neutron flux for various polyethylene configurations to determine the detectors needed for the external RMS.

Polyethylene thickness (cm)		Neutron flux ( n.cm <sup>-2</sup> .s <sup>-1</sup> )				
Front	Back	Thermal	Cd	Intermediate	Fast	Total
0	0	1.71E+01	1.66E+02	3.69E+02	6.71E+01	6.19E+02
0	0.5	5.44E+01	3.21E+02	5.53E+02	7.46E+01	1.00E+03
0	1	8.10E+01	4.32E+02	6.20E+02	7.73E+01	1.21E+03
0	1.5	1.03E+02	5.21E+02	6.51E+02	7.86E+01	1.35E+03
0	2	1.22E+02	5.90E+02	6.65E+02	7.94E+01	1.46E+03
0	2.5	1.36E+02	6.42E+02	6.73E+02	7.98E+01	1.53E+03
0	3	1.46E+02	6.81E+02	6.76E+02	7.98E+01	1.58E+03
0	4	1.60E+02	7.32E+02	6.79E+02	8.01E+01	1.65E+03
0.5	0	2.78E+01	1.69E+02	2.90E+02	4.73E+01	5.33E+02
0.5	0.5	8.80E+01	3.65E+02	4.09E+02	5.23E+01	9.14E+02
0.5	1	1.31E+02	4.98E+02	4.48E+02	5.38E+01	1.13E+03
0.5	1.5	1.64E+02	6.02E+02	4.65E+02	5.45E+01	1.29E+03
0.5	2	1.91E+02	6.84E+02	4.73E+02	5.50E+01	1.40E+03
0.5	2.5	2.10E+02	7.44E+02	4.77E+02	5.52E+01	1.49E+03
0.5	3	2.25E+02	7.89E+02	4.79E+02	5.54E+01	1.55E+03
0.5	4	2.45E+02	8.49E+02	4.81E+02	5.56E+01	1.63E+03
1	0	3.30E+01	1.71E+02	2.19E+02	3.61E+01	4.59E+02
1	0.5	1.00E+02	3.74E+02	3.02E+02	3.99E+01	8.17E+02
1	1	1.45E+02	5.08E+02	3.28E+02	4.10E+01	1.02E+03
1	1.5	1.81E+02	6.14E+02	3.39E+02	4.16E+01	1.18E+03
1	2	2.08E+02	6.96E+02	3.44E+02	4.19E+01	1.29E+03
1	2.5	2.28E+02	7.56E+02	3.47E+02	4.21E+01	1.37E+03
1	3	2.44E+02	8.02E+02	3.49E+02	4.22E+01	1.44E+03
1	4	2.64E+02	8.63E+02	3.49E+02	4.22E+01	1.52E+03
1.5	0	3.57E+01	1.70E+02	1.63E+02	2.82E+01	3.96E+02
1.5	0.5	1.05E+02	3.70E+02	2.24E+02	3.09E+01	7.29E+02
1.5	1	1.50E+02	5.04E+02	2.41E+02	3.16E+01	9.26E+02
1.5	1.5	1.85E+02	6.07E+02	2.48E+02	3.21E+01	1.07E+03
1.5	2	2.11E+02	6.84E+02	2.52E+02	3.24E+01	1.18E+03
1.5	2.5	2.31E+02	7.42E+02	2.54E+02	3.25E+01	1.26E+03
1.5	3	2.46E+02	7.87E+02	2.55E+02	3.26E+01	1.32E+03
1.5	4	2.65E+02	8.44E+02	2.56E+02	3.27E+01	1.40E+03
2	0	3.65E+01	1.64E+02	1.18E+02	2.19E+01	3.40E+02
2	0.5	1.05E+02	3.57E+02	1.62E+02	2.40E+01	6.48E+02
2	1	1.50E+02	4.85E+02	1.75E+02	2.45E+01	8.35E+02
2	1.5	1.83E+02	5.82E+02	1.81E+02	2.50E+01	9.71E+02
2	2	2.07E+02	6.55E+02	1.84E+02	2.52E+01	1.07E+03
2	2.5	2.25E+02	7.09E+02	1.85E+02	2.52E+01	1.14E+03
2	3	2.39E+02	7.49E+02	1.86E+02	2.53E+01	1.20E+03
2	4	2.57E+02	8.03E+02	1.87E+02	2.54E+01	1.27E+03

APPENDIX E

THERMAL NEUTRON FLUX FOR MULTICASK SCENARIO

**Table E-1 External RMS results for Single Cask**

DS	Flux ( n/cm2s)	CPS	Counts	$\beta$ (%)
RS	3.27E+02	3.14E+03	1.57E+04	N/A
1	3.19E+02	3.07E+03	1.53E+04	17
2	3.18E+02	3.05E+03	1.53E+04	8
3	3.18E+02	3.06E+03	1.53E+04	9
4	3.19E+02	3.07E+03	1.53E+04	16
5	3.19E+02	3.06E+03	1.53E+04	16
6	3.17E+02	3.04E+03	1.52E+04	3
7	3.15E+02	3.02E+03	1.51E+04	0
8	3.15E+02	3.02E+03	1.51E+04	0
9	3.17E+02	3.04E+03	1.52E+04	2
10	3.19E+02	3.07E+03	1.53E+04	16
11	3.18E+02	3.05E+03	1.53E+04	8
12	3.15E+02	3.02E+03	1.51E+04	0
13	3.13E+02	3.00E+03	1.50E+04	0
14	3.13E+02	3.00E+03	1.50E+04	0
15	3.15E+02	3.02E+03	1.51E+04	0
16	3.18E+02	3.05E+03	1.53E+04	8
17	3.18E+02	3.05E+03	1.53E+04	8
18	3.15E+02	3.02E+03	1.51E+04	0
19	3.13E+02	3.00E+03	1.50E+04	0
20	3.13E+02	3.00E+03	1.50E+04	0
21	3.15E+02	3.02E+03	1.51E+04	0
22	3.18E+02	3.05E+03	1.53E+04	8
23	3.19E+02	3.07E+03	1.53E+04	16
24	3.17E+02	3.04E+03	1.52E+04	3
25	3.15E+02	3.02E+03	1.51E+04	0
26	3.15E+02	3.02E+03	1.51E+04	0
27	3.17E+02	3.04E+03	1.52E+04	3
28	3.19E+02	3.07E+03	1.53E+04	16
29	3.19E+02	3.07E+03	1.53E+04	17
30	3.18E+02	3.06E+03	1.53E+04	9
31	3.18E+02	3.06E+03	1.53E+04	9
32	3.19E+02	3.07E+03	1.53E+04	17

Single Cask  
 CPS/ nv= 9.6  
 Measurement time =5-s  
 $\alpha = 5\%$  and corresponding  
 threshold = 1.55E+04

**Table E-2 External RMS results for Multiple Cask**

DS	Flux (n.cm <sup>-2</sup> s <sup>-1</sup> )	CPS	Counts	β (%)
Full	1.37E+02	1.32E+03	1.75E+05	N/A
1	1.32E+02	1.27E+03	1.69E+05	0
2	1.31E+02	1.26E+03	1.68E+05	0
3	1.32E+02	1.27E+03	1.68E+05	0
4	1.33E+02	1.28E+03	1.70E+05	0
5	1.34E+02	1.29E+03	1.71E+05	0
6	1.32E+02	1.27E+03	1.69E+05	0
7	1.32E+02	1.27E+03	1.69E+05	0
8	1.32E+02	1.27E+03	1.69E+05	0
9	1.34E+02	1.28E+03	1.71E+05	0
10	1.35E+02	1.30E+03	1.73E+05	1
11	1.34E+02	1.29E+03	1.71E+05	0
12	1.33E+02	1.28E+03	1.70E+05	0
13	1.31E+02	1.26E+03	1.68E+05	0
14	1.32E+02	1.27E+03	1.69E+05	0
15	1.33E+02	1.28E+03	1.70E+05	0
16	1.32E+02	1.26E+03	1.68E+05	0
17	1.31E+02	1.26E+03	1.68E+05	0
18	1.32E+02	1.26E+03	1.68E+05	0
19	1.33E+02	1.28E+03	1.70E+05	0
20	1.35E+02	1.30E+03	1.72E+05	0
21	1.34E+02	1.29E+03	1.71E+05	0
22	1.34E+02	1.29E+03	1.71E+05	0
23	1.34E+02	1.29E+03	1.71E+05	0
24	1.35E+02	1.29E+03	1.72E+05	0
25	1.35E+02	1.29E+03	1.72E+05	0
26	1.35E+02	1.29E+03	1.72E+05	0
27	1.35E+02	1.30E+03	1.72E+05	0
28	1.36E+02	1.31E+03	1.74E+05	19
29	1.35E+02	1.30E+03	1.73E+05	0
30	1.35E+02	1.30E+03	1.72E+05	0
31	1.34E+02	1.29E+03	1.71E+05	0
32	1.34E+02	1.29E+03	1.71E+05	0

Multiple casks  
CPS/ nv= 9.6  
Measurement time =82s  
α = 5% and  
corresponding threshold  
= 1.07E+05

## APPENDIX F

### INTERNAL AND EXTERNAL RMS COST

The usage of RMS allows for more efficient inspection regimes by authorities like the IAEA. This is because the number of inspections to a facility can be decreased due to 24/7 surveillance using the RMS. Hence, the proposed cost of the RMS is an important factor to consider. As a rule, the cost of the systems should not exceed 1-2% the cost of a dry cask. Since the cost of a dry cask is approximately \$1,000,000 [88], the total cost of the systems should not be more than \$20,000.

Since there are two RMSs proposed, the cost of both systems is provided in Table F-1 and Table F-2. For each dry cask, the choice of using one or both systems are up to the facility operator.

**Table F-1 Cost of internal RMS excluding electronics like amplifiers, preamplifiers, cables, etc.**

<b>RMS component for one unit (per one dry cask)</b>	<b>Cost (\$)</b>
*Cadmium plate, (46×46×0.05) cm	1,135
*Polyethylene box, (46×46×7.08) cm	300
**Fission chamber (2 pieces)	12,000
Total cost per one RMS unit	13,435

*\*The prices for cadmium and polyethylene were obtained from Goodfellowusa.com*

*\*\* The price for fission chamber was obtained from the manufacturer*

In the cost estimate for the internal RMS, the cost for electronics like cables, preamplifier and amplifier are not included. This will further increase the cost depending on the electronics purchased. However, the base cost of a single RMS costs \$13,435.

**Table F-2 Cost of external RMS**

<b>RMS component for one unit (per one dry cask)</b>	<b>Cost (\$)</b>
MSND detectors and driver	1,135
Polyethylene box, (8 x 4 x 4) cm	300
Total cost per one RMS unit	4,696

The external RMS costs \$4,696 including all the electronics. Hence for a single dry cask, if the operator decides to use both systems, the total cost is under \$20,000 which is within the initial plan of being 1-2% the cost of a dry cask. This price is great for a highly reliable robust system that allows for 24/7 monitoring.

APPENDIX G  
ADDITIONAL SIMULATIONS FOR INTERNAL RMS USING NATURAL  
URANIUM RODS

These simulations are performed for the internal RMS using natural uranium rods inserted in water instead of SNF in a dry cask. This was initially done as a test to see if a small-scale experiment was plausible using the natural uranium rods available at Texas A&M University. The setup was already made using natural uranium rods within a drum. That drum was placed inside another drum where the gap between both drums was filled with water. This setup was for a different experiment; however, I was permitted to use the rods in this configuration for my own experiment. Figure G-1 shows the setup where the rods are in the center and the green region represents the water between both drums. For the purpose of this work, the goal was to place the internal RMS over the rods and divert some rods to characterize the response of the internal RMS.

From the preliminary MCNP simulations of the experimental setup, it turned out that more natural uranium rods were necessary for the execution of the experiment than what was available. This was because it was challenging to detect a signal from the existing rods in a timely manner. Hence, these MCNP simulations (rather than the experiments) serve as a proof-of-concept to determine if the internal RMS could detect diversions of natural uranium rods in a timely manner.

In these simulations, each natural uranium rod was 23 cm long and had a diameter of 4 cm. The rods were annular with an air hole of diameter 1.4 cm. Four rods stacked on top of each other created a 92 cm long rod. A total of 436 small rods were used to represent assemblies where each assembly was a bundle of four 92 cm rods (16 small rods). These assemblies were placed in a drum filled with water. The drum had a diameter of 50.8 cm hence, there was 12.7 cm thick water between the assemblies and the inner surface of the drum.

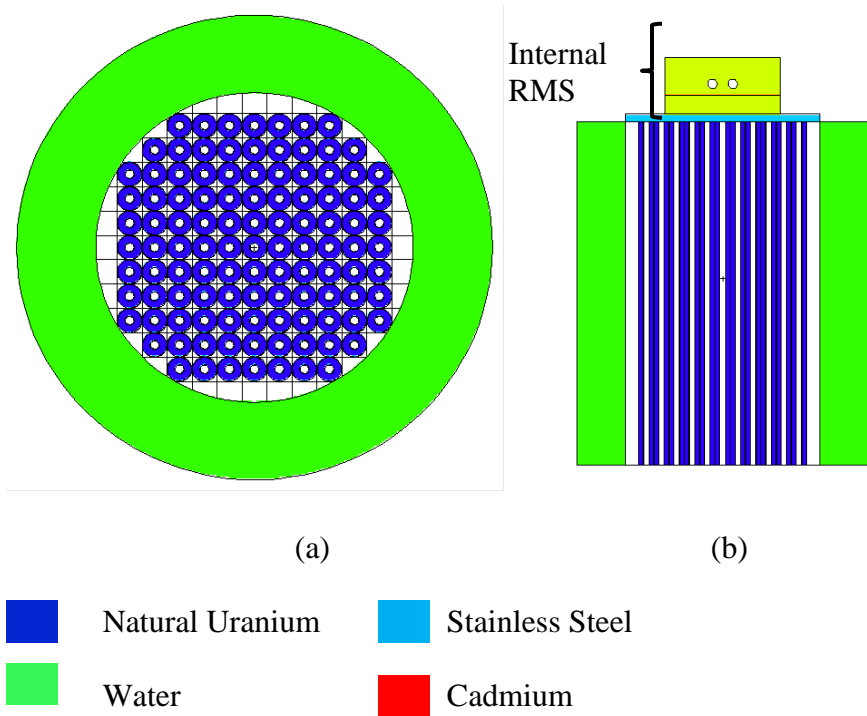


**Figure G-1 Natural Uranium rods surrounded by water drum in the (a) radial view and (b) axial view**

A full case containing all 436 rods that served as the reference case (RS) was simulated in MCNP, followed by eight different diversion scenarios (DS) as shown in Figure G-2 where DS 1 through DS5 are single assembly diversions with 432 rods present and DS 6 through DS8 are two assembly diversions with 428 rods present. As before, the average thermal neutron fluxes were obtained from energy binned F4 cell flux average tallies in MCNP and the corresponding  $\beta$  probabilities are calculated using a 5%  $\alpha$ .

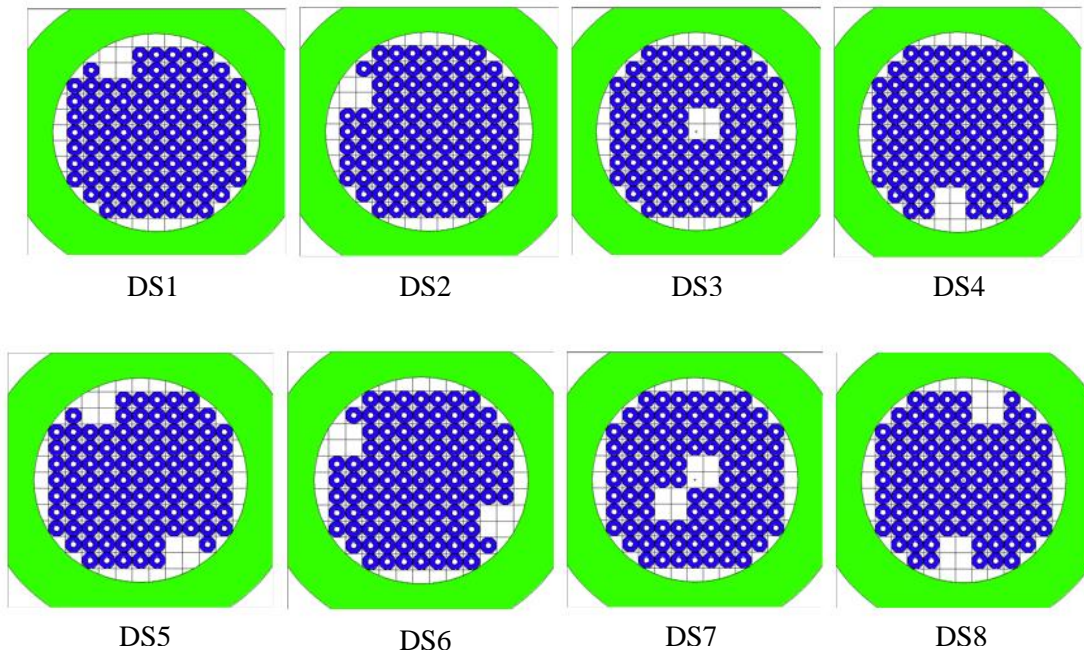


**Figure G-2 Diversion scenarios using natural uranium rods**

The neutron production in  $^{238}\text{U}$  was obtained to be  $13.6 \text{ n}\cdot\text{s}^{-1}\cdot\text{kg}^{-1}$  [89]. Each rodlet weighed 1.81 kg. Hence, for the reference simulation with 436 uranium rods, total source strength emitted was  $10.7 \text{ E}+03 \text{ n}\cdot\text{s}^{-1}$ . In comparison, a single SNF assembly had

a neutron source strength of  $4.74 \text{ E}+08 \text{ ns}^{-1}$  and a single  $^{252}\text{Cf}$  sources used in the small-scale experiment performed at TAMU had a strength of  $5.11\text{E}+04 \text{ ns}^{-1}$ . These 436-natural uranium rodlets combined produced a much smaller neutron source than the previous sources that were investigated.

From the diversion scenarios, it was shown that a measurement time of 114 hours (~5 days) would be required to tell is an ‘assembly’ containing 16 natural uranium rods were diverted. The counts recorded by the left and right detectors inside the internal RMS is shown in Table G-1 along with the corresponding  $\beta$  probabilities for each DS. Here, a measurement time of  $4.32\text{E}+05$  seconds or 5 days was used with a false alarm probability,  $\alpha$  of 5%.

From Table G-1, it is seen that the trends remained the same for the internal RMS - when diversions take place closer to the center of the setup where the detectors were present, it was easier to detect. The  $\beta$  probabilities decreased from DS1 to DS2 to DS3 as the diversions approached the center. Also, two assembly diversions (DS 6 through DS8) were easier to detect than the single assembly diversions. In order to obtain all  $\beta$  probabilities less than 20%, a measurement time of ~12 days would be required.

If there were ~1200 rods instead of 436, the measurement time would decrease to ~3 days to obtain  $\beta$  probabilities less than 20%. Hence, it was proved that this experiment would not be feasible.

**Table G-1  $\beta$  probabilities of the left and right detector within the internal RMS for 5%  $\alpha$  and measurement time of 5 days ( $4.32E+05$  s)**

	Left Detector			Right detector		
	Counts	$\sigma$	$\beta$ (%)	Counts	$\sigma$	$\beta$ (%)
Full	148923	386	-	149562	387	-
DS1	150049	387	10	150180	388	52
DS2	150308	388	3	150691	388	10
DS3	140995	375	0	140741	375	0
DS4	148229	385	44	148667	386	25
DS5	151944	390	0	152527	391	0
DS6	150822	388	0	151507	389	0
DS7	137004	370	0	137091	370	0
DS8	148138	385	35	148656	386	24